Optical, Electronic, and Dynamical Phenomena in the Shock Compression of Condensed Matter

by

Evan J. Reed

B.S., California Institute of Technology (1998)

Submitted to the Department of Physics
in partial fulfillment of the requirements for the degree of

Doctor of Philosophy

at the

MASSACHUSETTS INSTITUTE OF TECHNOLOGY

May 2003

Author . . . .
Department of Physics
May 2, 2003

Certified by . . . .
John D. Joannopoulos
Francis Wright Davis Professor of Physics
Thesis Supervisor

Accepted by . . . .
Thomas J. Greytak
Chairman, Department Committee on Graduate Students

Optical, Electronic, and Dynamical Phenomena in the Shock Compression of Condensed Matter

by

Evan J. Reed

Submitted to the Department of Physics
on May 2, 2003, in partial fulfillment of the
requirements for the degree of
Doctor of Philosophy

Abstract

Despite the study of shock wave compression of condensed matter for over 100 years, scant progress has been made in understanding the microscopic details. This thesis explores microscopic phenomena in shock compression of condensed matter including electronic excitations at the shock front, a new dynamical formulation of shock waves that links the microscopic scale to the macroscopic scale, and basic questions regarding the role of crystallinity in the propagation of electromagnetic radiation in a shocked material.

In Chapter 2, the nature of electronic excitations in crystalline solid nitromethane are examined under conditions of shock compression. Density functional theory calculations are used to determine the crystal bandgap under hydrostatic stress, uniaxial strain, and shear strain for pure and defective materials. In all cases, the bandgap is not lowered enough to produce a significant population of excited states.

In Chapter 3, a new multi-scale simulation method is formulated for the study of shocked materials. The method allows the molecular dynamics simulation of the system under dynamical shock conditions for orders of magnitude longer time periods than is possible using the popular non-equilibrium molecular dynamics (NEMD) approach. An example calculation is given for a model potential for silicon in which a computational speedup of 10^5 is demonstrated. Results of these simulations are consistent with some recent experimental observations.

Chapters 4 and 5 present unexpected new physical phenomena that result when light interacts with a shock wave propagating through a photonic crystal. These new phenomena include the capture of light at the shock wave front and re-emission at a tunable pulse rate and carrier frequency across the bandgap, and bandwidth narrowing of an arbitrary signal as opposed to the ubiquitous bandwidth broadening. Reversed and anomalous Doppler shifts are also predicted in light reflected from the shock front.

Thesis Supervisor: John D. Joannopoulos
Title: Francis Wright Davis Professor of Physics

Acknowledgments

First, I must acknowledge my thesis advisor, John Joannopoulos. My graduate experience would not have been the same without John's constant reassurance that I will graduate in only 8 or 9 more years. Perhaps most importantly, I have learned from John the value of enthusiasm for research and the importance of conveying this in presentations and writing. I have also learned people management skills which may be useful if I ever get a real job someday. All the research topics in this thesis are a result of the fact John has allowed me tremendous freedom in research direction and has placed an emphasis on creative and interdisciplinary science.

I also owe considerable gratitude to Larry Fried at LLNL for playing a major role in my graduate studies. Larry has provided significant direction and encouragement, which was particularly important in the early stages. In addition to his personal attention, Larry has provided computer resources and financial support in the form of an LLNL MRI/EMC graduate fellowship. Much of what I know about shock waves, electronic structure, and molecular dynamics was picked up during sunny summers spent at LLNL. Those summers have also given me the confidence to secretly infiltrate the chemistry community without being suspected of being a physicist.

Marin Soljacic has also played a major role in the course of my research. The work on shock waves in photonic crystals would not likely have been pursued without Marin's enthusiasm and support in the very early stages. In the beginning, Marin was the only person who did not think shooting a photonic crystal with a gun was mere senseless destruction, and he continues to play an important role in spinoffs of this work.

At MIT, I would like to thank all members of the JJ group that I've overlapped with: Dan Abrams, Peter Bermel, Peter Bienstman, David Chan, Matt Evans, Shanhui Fan, Casey Huang, Steven Johnson, Mihai Ibanescu, Lefteris Lidorikis, Chiyan Luo, Atilla Mekis, Niko Moll, Ickjin Park, Michelle Povinelli, David Roundy, Maksim Skorobogatiy, Marin Soljacic, Pierre Villeneuve, Tairan Wang, and Josh Weitz. I also thank Sidney Yip and members of his research group for exposing me to the key is-

sues in computational materials science. Niko taught me most of what I know about density functional theory and provided important encouragement while I was getting started. He also taught me that the 4.5 years of German I took in high school were completely wasted. Thanks to Steven for making me not feel bad about showing up so late every day. Thanks to Michelle for voicing some outrage over the mice in the corridor. Thanks to Lefteris for providing great elevator music while I wait for things at the printer. I enjoyed the scheming for global domination with Tairan. Thanks to Casey for enhancing my quality of life with the addition of the 12-111 refrigerator.

I would like to thank the LLNL folks I have interacted with: Ing Chiu, Jerry Forbes, Rick Gee, Kurt Glaesemann, Dave Hare, Neil Holmes, Riad Manaa, Carl Melius, Craig Tarver, and Dan Yu. Thanks to Rick for getting me hooked on spicy food, Kurt for regular reminders that I am not a chemist, and Riad and Dan for being good sports during particularly steep lazy 8's.

Thanks to Angela Damery for taking me just about everywhere I've been in Boston. Thanks to Nick Choly and Tom Dmukauskis for listening to all my whining about graduate school and reminding me of the days of yore when the burning and destruction of large objects constituted a good time for all. Thanks to Ian Zacharia for sharing his laundry-related conspiracy theories.

Finally, thanks to my family for quelling their horror at my meager graduate student existence for the past few years: Mom, Dad, Sally, Dan, Ryan, and Reed. And Beau.

This thesis was paid for by the National Defense Science Education Graduate Fellowship (NDSEG) for the first three years, and the Lawrence Livermore National Laboratory Materials Research Institute Energetic Materials Center fellowship for the last two years. Some of the research in this thesis was performed under the auspices of the U.S. Department of Energy by the University of California Lawrence Livermore National Laboratory under contract No. W-7405-Eng-48.

Contents

List of Figures

List of Tables

Chapter 1

Introduction

Study of the propagation of shock waves in condensed matter has led to new discoveries ranging from new metastable states of carbon[74] to the metallic conductivity of hydrogen in Jupiter[48, 71] to the possibility of delivery of life to planets via meteorite impact.[18] Shock waves are currently the only practical way to simultaneously probe the high temperature and high pressure behavior of matter and the short timescale dynamical response of materials to extreme conditions.

Shock waves are similar to sound waves, but have amplitudes sufficiently large that a nonlinear material response results in the formation of a sharp discontinuity between the pre and post-shock material thermodynamic quantities like density and stress. Shock waves propagate faster than the material sound speed. Shock compression is inherently irreversible, and differs from adiabatic compression by the addition of extra heat to the post-shock material. The response of a material to a shock wave may be very different than under static high pressure conditions like those found in a diamond anvil cell. The strain behind a shock wave is usually of a uniaxial nature on short timescales. Furthermore, the material behind a shock front may contain highly non-equilibrium regions in which interesting and poorly understood physics occurs. Such non-equilibrium regions have been shown to give rise to the formation of metastable states of matter,[74] and are central to understanding the initiation and detonation process of high explosives.[65, 54]

As an experimental tool, shock waves are currently the only way to simultaneously study the high temperature and high pressure equation of state of materials. Shock waves can be generated in a controlled laboratory setting in several different ways. First, large guns that shoot projectiles are routinely fired at targets to launch shock waves in these targets. Recently, high intensity lasers have been successfully used to generate shock waves. These shocks are shorter lived than shocks produced in gun experiments. The detonation of high explosives can also be used to generate shock waves.

Despite the study of shock wave compression of condensed matter for over 100 years, progress in understanding the microscopic details has been extremely difficult. Phenomena like phase transitions and plastic deformation that occur on the atomic scale can manifest themselves in the behavior of the shock on the macroscopic scale.[34, 40, 65, 54] Therefore, an understanding of the atomic scale phenomena is essential to understanding the behavior of the shock wave. Experimental study of the microscopic effects of these shock waves on materials is made difficult by the *simultaneously* short time (as short as 10 femtoseconds) and length scales (as short as Ångstroms) involved with the various shock processes like the shock front thickness and shock compression timescale. Theoretical approaches are therefore of significant value. [26, 20, 35, 54]

The study of shock waves is usually broken into two categories: shocks in energetic materials and shocks in non-energetic materials. Energetic materials release energy when shocked and can form detonation shock waves. Detonation is a special form of combustion where most of the energy transfer between the reacted and unreacted parts of the system occurs through mass flow in the form of compressive shock waves. During detonation, the chemical reaction front propagates 10^3 to 10^8 times faster than in a flame, where heat conduction is the primary mechanism of energy transfer. [17] Detonation occurs when rapid chemical reactions result in an increase in volume. This volume increase can result in part from large molecules breaking up into many smaller molecules or from thermal expansion resulting from an increase in temperature due to exothermic reactions. The volume increase drives the detonation wave.

The modern theoretical understanding of detonation waves on the macroscopic scale began in the 1940s with work by von Neumann and others. However, despite substantial progress in characterization of the phenomenological properties of known energetic materials, little progress has been made in understanding the microscopic details of detonation waves. Microscopic theories of detonation are currently an active area of research.[64] Questions as basic as the effect of the shock front on energetic materials have yet to be definitively answered.

Computational power and simulation methodology has reached the point today where microscopic scale phenomena can be elucidated to a meaningful degree of accuracy. A wide variety of methods exist for calculating the total energy of a given spatial configuration of atoms. These methods range considerably in their complexity and computational requirements, and this thesis makes use of a number of these methods. On the more expensive side are density functional theory based approaches to calculation of the self-consistent electronic density and total energy. [25, 50] These approaches are often similar to the Hartree approximation, but give reasonably quantitative results for many systems and scenarios of interest through the inclusion of exchange and correlation effects as a functional of the local total electron density. Less accurate and less computationally expensive are tight-binding approaches, which are usually non self-consistent and often parameterized with a large amount of empirical data. The least accurate and least computationally expensive approaches to the calculation of total energies utilize empirically derived classical interatomic potentials.

In addition to information about the total energy and electronic structure, these computational schemes can provide interatomic forces for use in "molecular dynamics" simulations where the atomic nuclei obey classical equations of motion. [1] Molecular dynamics simulations can now be used to study of shock waves on the atomistic scale. For the first time, it is now becoming possible to understand the microscopic details of shock waves. [26, 20, 35] Chapters 2 and 3 present applications of atomistic modeling to shock waves in condensed matter.

1.1 Electronic phenomena in shocked molecular solids

Energetic materials come in a wide variety of forms ranging from liquids to gasses to solids to aerogels and have practical uses ranging from mining to automobile airbags to weapons. Most energetic materials of practical interest are molecular crystals of organic molecules.

It is very challenging to perform any but the simplest experiments on energetic materials. In addition to the extremely short time and length scales involved with the detonation and initiation process, there are practical considerations that are of utmost importance. Energetic materials are generally very dangerous to handle and work with and the experiment can destroy the surrounding experimental apparatus.

Most of the theoretical understanding of energetic systems to date has been obtained at the level of continuum material descriptions. Most of the atomistic modeling has been focused on properties of individual molecules (i.e. gas phase) rather than properties of the molecules in condensed phases in which they are actually used as explosives. Furthermore, the complexity and size of most energetic molecular solids have been prohibitively large for detailed quantum mechanical studies until now.

It has been postulated that bandgap closure occurs at the shock fronts in energetic materials leading to very fast dissociative chemistry which drives the detonation shock wave.[72, 36, 21] Chapter 2 explores effects of a shock wave on the electronic structure on crystalline nitromethane. Nitromethane (CH_3NO_2) can be made to detonate in the laboratory and has a chemical composition similar to other commonly used energetic materials. Nitromethane is electronically insulating under atmospheric conditions, but may become metallic under shock compression. The electronic structure of the system is studied under shock conditions within the context of density functional theory. The possibility of metallization at the shock front and other phenomena that could lead to fast chemistry are explored.

Chapter 2 attempts to consider the effects of a shock wave on a small piece of the crystalline nitromethane material without simulating the entire shock wave structure. Reduction of a macroscopic shock wave to a small representative material element enables the use of computationally expensive and accurate methods like density functional theory to simulate the effects of a shock wave. Chapter 3 extends this idea and puts it on a formal basis. Chapter 3 presents a new way of thinking about shock waves from the point of view of an element of the material being shocked.

1.2 A new molecular dynamics simulation methodology

Shock waves in condensed phase materials are inherently multi-scale entities. The propagation of the shock in a medium can be described to some extent by continuum theory, but the equation of state of the material arises from the atomistic scale. Therefore, a good theoretical understanding of shock waves requires an understanding of the physics at the atomic length and timescales. Molecular dynamics computer simulations of shock waves can be performed using model interactions between each atom. In principle, this approach captures the important physics on the atomistic length and time scales. However, computationally expensive techniques for molecular dynamics simulation like density functional theory or tight-binding are almost always required for an accurate treatment of extreme phenomena like the extreme deformations and bond breaking that can occur in a shock wave. It is only possible to perform molecular dynamics simulations with a few hundred atoms at this level of accuracy. Therefore, making contact between experimental observations of macroscopic behavior and molecular dynamics simulations has been extremely difficult because of the tremendous computational requirement.

The fact that macroscopic material behavior requires an understanding of the atomic scale behavior is a fundamental problem in the computational simulation of materials. Considerable effort has been put into the formulation of multi-scale computational methodologies that combine aspects of both the atomistic and macroscopic length and time scales. In Chapter 3, a new computational simulation methodology is formulated that combines atomistic simulation methodologies with the Euler equations for compressible flow of a continuum fluid. This new hybrid methodology enables the simulation of an entire shock wave by performing molecular dynamics only on a small material element of the system. Stress boundary conditions on that material element come from continuum theory. This new multiscale approach opens up the door to the study of shock waves using accurate material descriptions, like density functional theory, and therefore making contact with experiments.

Chapter 3 describes the new simulation method and presents an application of the method to silicon. Agreement is found between the simulations and some recent experimental observations of shocked silicon.

Along with other microscopic details of shocked condensed matter, the role of a crystal lattice is only beginning to be elucidated through molecular dynamics simulations. The more general question of what happens when a shock wave propagates through a periodic medium is completely unanswered. Chapters 4 and 5 shift gears away from the atomistic scale to a continuum picture of shock waves where this fundamental question of periodicity is addressed in the context of optical phenomena.

1.3 Optical phenomena in shocked photonic crystals

Chapters 4 and 5 focus on optical phenomena in shocked condensed matter. Some diagnostics used in shock wave experiments involve measurement of light reflected from the shock front. Chapters 4 and 5 focus on the reflection of light from a shock wave front propagating through a 1D photonic crystal, or material with a periodic modulation of the dielectric.[73, 31, 30]

Photonic crystals in 1D are essentially multilayer films of the sort used in optical coatings and filters. They usually consist of alternating layers of high and low index of refraction materials. Bandgaps exist in these materials with frequency ranges that are functions of the crystal lattice constant and the dielectric values of the primitive unit cells that comprise the crystal. Light is not allowed to propagate within the bandgap frequency regions. As a shock wave propagates through the crystal, the lattice constant is compressed and the dielectric of the individual layers may be altered, resulting in a shift in the bandgap frequencies of the shocked crystal.

Chapters 4 and 5 consider the effect on light propagation of the changing frequency of the bandgaps as the shock propagates. Theoretical treatment of this electromagnetic problem is considerably more simple than that of the electronic phenomena in Chapter 2 because Maxwell's equations can be solved exactly, at least numerically. Numerical and analytical solutions to Maxwell's equations are determined in these Chapters for a time-dependent dielectric that represents the shocked photonic crystal.

In Chapter 4, it is discovered that several remarkable phenomena can occur. These new phenomena include the capture of light at the shock wave front and re-emission at a tunable pulse rate and carrier frequency across the bandgap, resulting in

a Doppler-like frequency shift enhanced by as much as 10,000 times. Also, bandwidth *narrowing* of an input signal by a factor or 10 or more can occur. This is to be distinguished from the ubiquitous bandwidth broadening, which is relatively easy to accomplish. Both of these effects do not occur in any other physical system, and are all realizable under experimentally accessible conditions. Furthermore, their generality make them amenable to observation in a variety of time-dependent photonic crystal systems, which has significant technological implications.

For some photonic crystal systems, Chapter 5 discusses how it is possible to observe a *reversed* Doppler shift and other anomalous Doppler effects in light reflected from the moving shock front. Non-relativistic reversed Doppler shifts have never been observed in nature.

Chapter 2

Electronic excitations in shocked nitromethane

The nature of electronic excitations in crystalline solid nitromethane under conditions of shock loading and static compression are examined. Density functional theory calculations are used to determine the crystal bandgap under hydrostatic stress, uniaxial strain, and shear strain. Bandgap lowering under uniaxial strain due to molecular defects and vacancies is considered. *Ab-initio* molecular dynamics simulations are done of all possible nearest neighbor collisions at a shock front, and of crystal shearing along a sterically hindered slip plane. In all cases, the bandgap is not lowered enough to produce a significant population of excited states in the crystal. The nearly free rotation of the nitromethane methyl group and localized nature of the HOMO and LUMO states play a role in this result. Dynamical effects have a more significant effect on the bandgap than static effects, but relative molecule velocities in excess of 6 km/sec are required to produce a significant thermal population of excited states.

2.1 Introduction

The last two decades have produced significant new insights into the basic science of high explosives. Experiments and theory have suggested that the sensitivity of high explosives to initiation by mechanical perturbations or shocks is a strong function of solid-state properties including crystal structure, defects, and dislocations. [65, 11, 29, 47, 6] Behind a shock front lies a region that is far from equilibrium, where solid-state properties may determine the rates and mechanisms through which the material reaches equilibrium.

Any complete microscopic description of the initiation of high explosives will elucidate the mechanisms of energy transfer into the individual molecules from a shock wave.[19] No such theory currently exists in a widely agreed upon form.

One possible energy transfer mechanism involves shock-wave induced electronic excitations of the molecules. In 1971, Williams suggested that excited states play a role in the initiation and propagation of detonation waves in explosives.[72] A similarity between shock decomposition products to those of photochemical processes was later pointed out by Dremin, *et. al.*[14] A correlation has been reported between the impact sensitivity of a homologous series of explosives and the energies of their optically forbidden electronic transitions across the bandgap.[58] Gilman has proposed metallization at the shock front resulting from bending of covalent bonds.[21] Such metallization has been found to occur under static pressure conditions in the covalently bonded crystalline semiconductors Si and Ge. These materials undergo a phase transition to a metallic phase at pressures comparable to those found in detonating energetic materials.[59] Finally, Kuklja, *et. al.,* have proposed bandgap lowering and electronic excitations around crystal defects under compression as a mechanism for detonation initiation.[36]

Chemistry is thought to begin to occur on a 10 or 100 picosecond time scale behind a shock front in some energetic materials.[65] This requires a fast mechanism of energy transfer from the shock wave to the molecular degrees of freedom. A mechanism for energy transfer from the shock directly into molecular electronic degrees of freedom is appealing because electronic excitation to an unstable energy surface can result in rapid dissociation of a molecule. A similar mechanism has been found to be a cause of rapid migration of interstitials in crystalline silicon subjected to radiation.[2]

Manaa, *et. al.*, have done *ab initio* complete active space self-consistent field studies of molecular nitromethane (CH_3NO_2).[42] They found that the HOMO and

LUMO states can be made to cross by bending the nitro group out of the CNOO plane by approximately 50 degrees. This is the lowest energy HOMO-LUMO crossing point. This molecular geometry is similar to the triplet (excited) state geometry, which lies 0.6 eV below in energy. These results suggest that non-radiative transitions from the excited state to a vibrationally hot ground state may be possible.

In this work we examine mechanisms of electronic excitations by a shock wave in solid nitromethane. Nitromethane is one of the simplest model energetic materials, and is an analogue of commonly used energetic materials such as TATB (1,3,5-triamino-2,4,6-trinitrobenzene) and TNT (2,4,6 trinitrotoluene). Here, we study the effect of the various conditions found in a shock or detonation wave on the bandgap of the solid.

2.2 Computational details

Density functional theory calculations were performed using the PW91[51] and PBE[52] generalized gradient approximations (GGAs) of Perdew. These exchange-correlation functionals produced nearly identical results in comparison cases. Calculations utilized Troullier-Martins pseudopotentials[68] and Vanderbilt ultrasoft pseudopotentials.[69] Plane waves with kinetic energy cutoffs of 25 Rydbergs and 40 Rydbergs were used with the Vanderbilt and Troullier-Martins pseudopotentials, respectively. Results obtained using the two sets of pseudopotentials are in good agreement. All calculations were converged with respect to k-point spacing in the Brillouin zone. In many cases, a single k-point was sufficient due to the minimal amount of dispersion across the single particle bands. Stresses reported here were calculated using an analytic approach based on plane-wave basis functions.[49]

Nitromethane is in the liquid state at room temperature and pressure, but most practical energetic materials are in a solid state under these conditions. We have chosen to study the crystalline form of nitromethane in analogy with other energetic materials. The primitive cell of nitromethane at zero pressure contains four molecules. Figure 2-1 contains two projections onto the lattice planes, and the top side of Figure 2-2 contains a perspective view. The atomic positions have been relaxed within the experimental lattice parameters. The space group is $P2_12_12_1$ with orthorhombic lattice vectors a=5.1832 Å, b=6.2357 Å, and c=8.5181 Å at T=4.2K.[66] Adjacent molecules along the c axis have alternating nitro and methyl groups which gives the unit cell a neutral overall dipole moment. Rotation of the methyl group has a very low barrier of about 118K.[67] It is therefore essentially a free rotor at higher temperatures. The molecular lattice is similar to a face-centered structure, with each molecule having 12 nearest neighbor molecules. The atomic positions and bond lengths of the relaxed structure at the experimental lattice size were found to be within 3% of the experimentally determined positions and bond lengths at T=4.2K.[66] Unless otherwise noted, all atoms in the unit cell were relaxed in the calculations presented here.

The calculated bandgap for the crystal at zero pressure is 3.28eV. The HOMO-LUMO gap for a single molecule is 3.75eV. This is similar to the 3.8eV HOMO-LUMO gap for a single molecule calculated using multi-configuration self-consistent field (MCSCF) techniques by Manaa, *et. al.*[43] Electron-impact spectroscopy techniques have been used to measure this transition for molecular nitromethane.[16] The intensity was observed to have an onset at 3.1eV and a maximum intensity at 3.8eV. We find that the relatively weak intermolecular interactions in the solid phase cause the bandgap to differ from the isolated molecule HOMO-LUMO energy difference only slightly.

The error associated with the bandgaps presented here is roughly estimated to be around 0.5 eV. Bandgaps calculated for unit cells relaxed within the local-density approximation (LDA)for exchange and correlation energy were all within 0.3 eV of the GGA values presented here. While bandgaps calculated within the LDA are typically a factor of two less than experimental values,[55] we believe the gaps presented here to be more accurate for the following reason. One of the assumptions associated with DFT quasiparticle energies is that removal or addition of a particle to a state leaves the total density unchanged.[55] The HOMO and LUMO states of a nitromethane molecule are both localized to the atoms in the nitro group, which

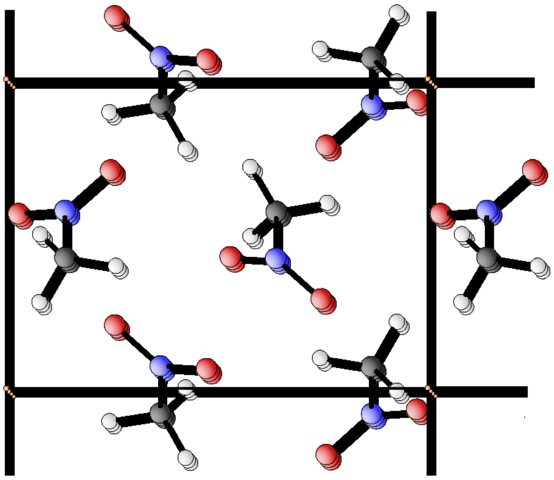

(a) zy plane

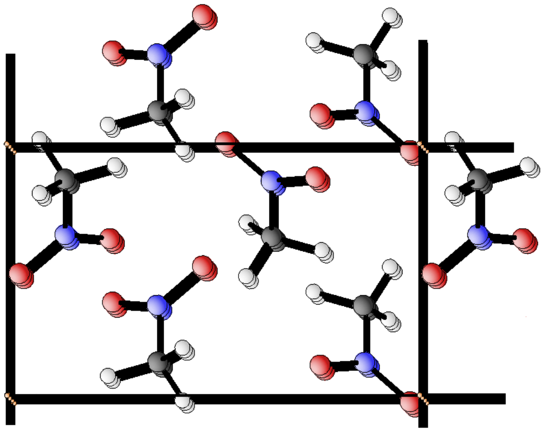

(b) zx plane

Figure 2-1: Two projections of nitromethane unit cell at zero pressure and zero temperature on, (a) the zy plane; (b) the zx plane. Hydrogen atoms are white, carbons atoms are gray, nitrogen atoms are blue, and oxygen atoms are red.

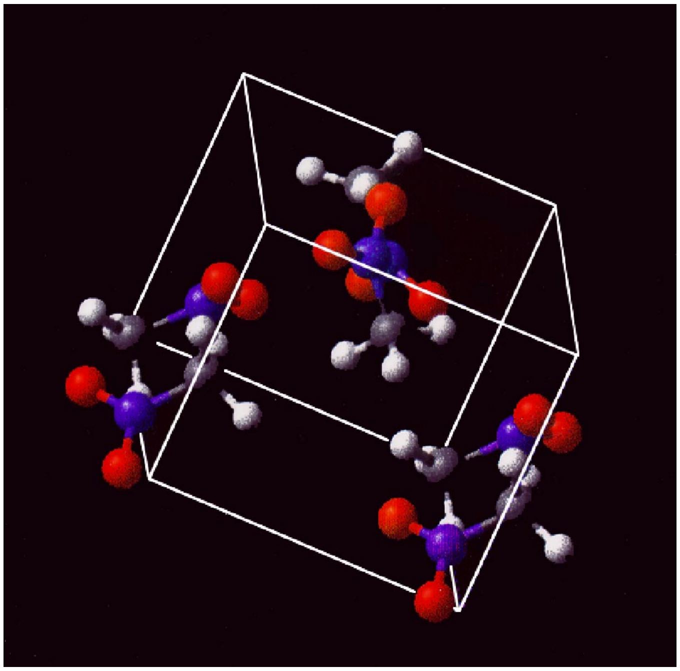

(a) $p = 0$ GPa

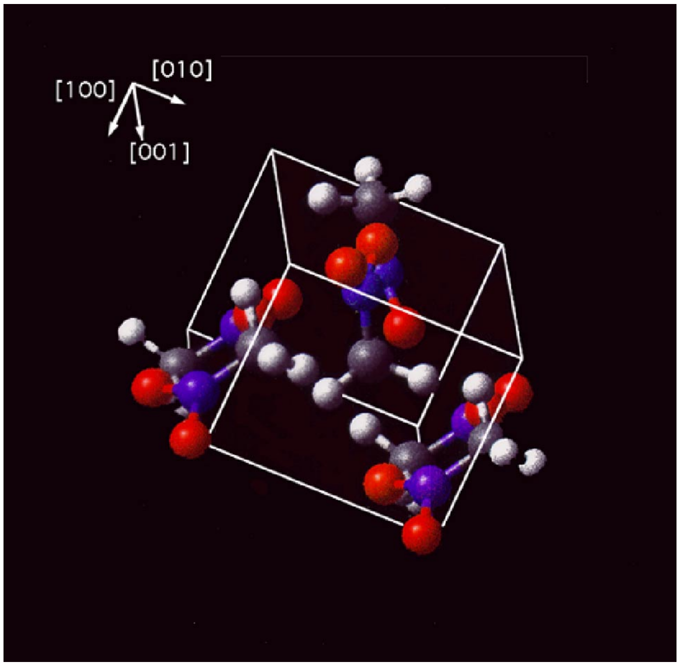

(b) $p = 180$ GPa

Figure 2-2: Comparison of the unit cell at 0 GPa (a) and 180 GPa (b) hydrostatic pressure. (Comparison is approximately to scale.) The orientation of the molecules is roughly the same at the two pressures, except for a significant rotation of the methyl group.

results in a relatively minor change in the total density when an electron is transferred from the HOMO to the LUMO. Therefore, the other occupied states do not require significant adjustments since the Kohn-Sham Hamiltonian is a functional only of the total density. Indeed the calculated HOMO-LUMO gap for a single molecule is almost identical to the experimental value. We expect to observe a similar behavior for the crystal bandgap. The nitromethane solid bandgap has been calculated within density functional theory using a bandgap correction based on the above idea.[55] The difference between the corrected and uncorrected bandgaps was found to be only 0.2 eV.[45] Manaa, *et. al.,* also report good agreement between DFT and complete active space self-consistent field methods for molecular nitromethane.[42]

If, upon compression or molecular distortion, the molecular orbitals rearrange such that the HOMO state density is no longer similar to the LUMO state density, we would expect to see an artificial lowering in the bandgap analogous to that seen in semiconductor systems. However, we also expect the dielectric screening to increase as the system density increases. This will reduce the significance of non-local many-body effects neglected in the exchange-correlation energy approximation used here. These effects lead us to expect our calculated bandgaps to be equal to or less than the true bandgaps.

This has been demonstrated in more accurate quasiparticle calculations on solid Xenon[5] within the GW approximation of Louie, *et. al.*[28] LDA bandgaps were shown to underestimate the experimental and GW approximation bandgaps at all densities up to metallization. Furthermore the difference between the LDA bandgap and the GW and experimental bandgaps diminished as the density increased. This effect was attributed to the increase of dielectric screening at higher densities.

As another preliminary check on the theoretical approximations employed, the molecular vibrational frequencies were computed by calculating the molecular Hessian and then diagonalizing the dynamical matrix. All vibrational frequencies were found to be within 5% of experimental values with the exception of the very high frequency CH symmetric stretch modes. These frequencies were up to 9% higher than experimental values.

2.3 Static conditions

2.3.1 Hydrostatic compression

In regions sufficiently far behind the shock front for the stress tensor to be equilibrated, a condition of hydrostatic compression exists. Starting at the experimental atmospheric pressure lattice size, the unit cell was compressed up to a hydrostatic pressure of 180 GPa with 6 intermediate pressure points. At each pressure, the lattice vectors and atoms in the unit cell were relaxed according to the forces. Table 2.1 contains the calculated lattice vectors at the pressures considered here. There is a lack of experimental lattice constant data at these higher pressures, but we expect the agreement between experiment and DFT to improve as the pressure increases the strength of the intermolecular interactions.

Hydrostatic Pressure (GPa)

	2	10	30	60	90	120	150	180
a	5.183	4.496	4.174	3.998	3.878	3.802	3.725	3.674
b	6.235	5.772	5.199	4.925	4.745	4.615	4.522	4.448
c	8.518	8.211	7.476	7.090	6.852	6.621	6.496	6.353

Table 2.1: Nitromethane lattice constants, in Ångstroms, calculated at various pressures.

In the pressure range explored, the crystal structure maintained the $P2_12_12_1$ symmetry. No bond bending was observed, but the 180 GPa molecules have bond lengths shortened by 7-15%. A phase transition of the methyl group rotation angle was observed to occur between the 10 and 30 GPa calculations. Such a transformation has been observed experimentally at 3.5 GPa.[9] It is possible that the zero pressure orientation of the hydrogens is only metastable in the 10 GPa calculation. There is also experimental evidence for a structural phase transition at 7 GPa at higher temperatures,[7] but a spontaneous phase transition was not observed in the calculations. The $P2_12_12_1$ structure is at least metastable in this pressure range at zero temperature. Cortecuisse, *et. al.*, have speculated that the phase transition at 7 GPa is associated with an increase in the number of molecules in the unit cell. A unit cell of 8 molecules with the a axis doubled and relaxed at 30 GPa was also found to be at least metastable.

Figures 2-2 and 2-3 contain the unit cell configurations and band structures at 2 GPa and 180 GPa. The bands at low pressure are relatively flat compared to high pressure where dispersion plays a role. As the pressure increases, band dispersion first appears in the mid-valence range, leaving the HOMO state relatively flat. This result is most likely associated with the extended nature of the states in this range. These states are delocalized over the whole molecule, while the HOMO state is localized on the nitro group. Intermolecular interactions should have a greater effect on orbitals that extend over the entire molecule, since they have larger overlaps than localized orbitals.

The bandgap change as a function of pressure is given in Figure 2-4. The HOMO-LUMO gap of a single molecule in the geometry of the 180 GPa calculation was found to be 3.96eV using MCSCF techniques.[44] This indicates that condensed phase effects are important in producing the band gap reduction as a function of pressure. The detonation pressure and temperature of nitromethane has been experimentally determined to be about 13 GPa and 2000K respectively,[8] and there is not a significant change in the bandgap in the vicinity of this pressure. Even compressing the crystal to a pressure an order of magnitude higher than that observed in developed detonation waves results in a bandgap lowering to around 2eV, which is not sufficiently low to provide a significant thermal conduction band population at the observed temperatures.

These results are qualitatively comparable to those of other theoretical studies. Hartree-Fock calculations have been performed by Kunz, *et. al.*, on RDX (hexahydro-1,3,5-trinitro-s-trizine), lithium azide (LiN_3), sodium azide (NaN_3), and lead azide $Pb(N_3)_2$.[36, 75] Upon compression to densities associated with detonation, most of these materials also showed some bandgap lowering, but not enough to produce a significant population of excited states at temperatures associated with detonation.

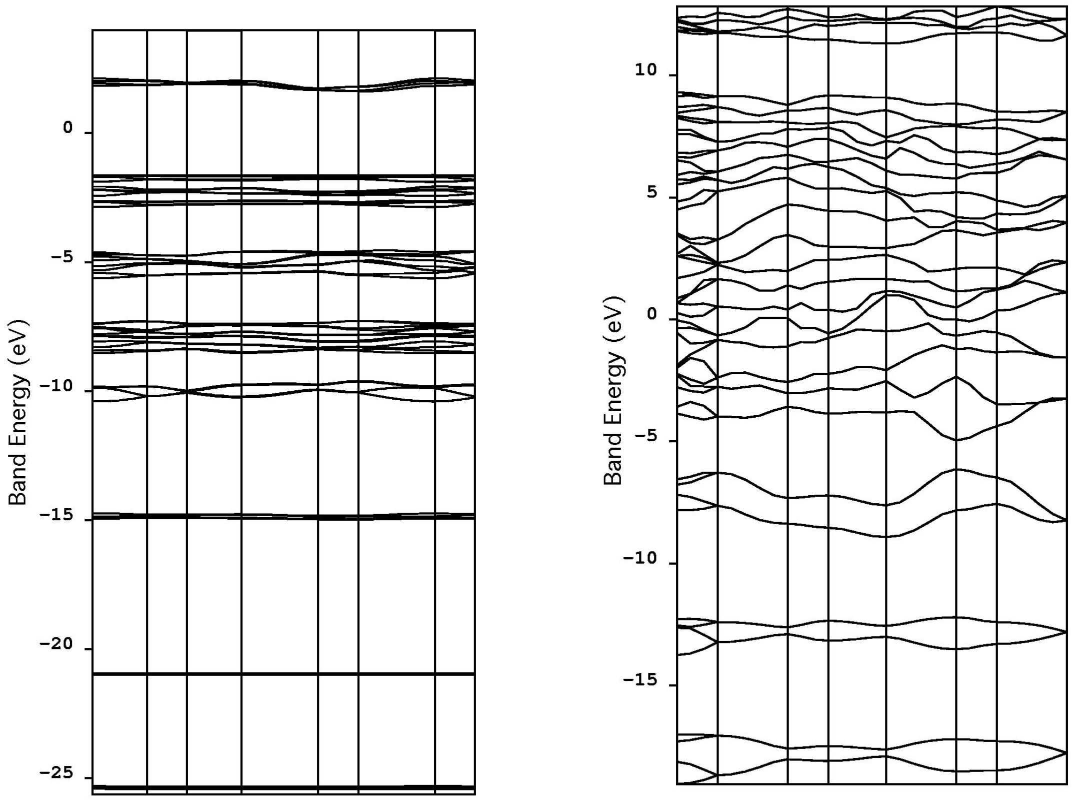

(a) $p = 0$ GPa (b) $p = 180$ GPa

Figure 2-3: Comparison of single particle band structures at zero (a) and 180 GPa (b) hydrostatic pressure. The top four bands are conduction bands.

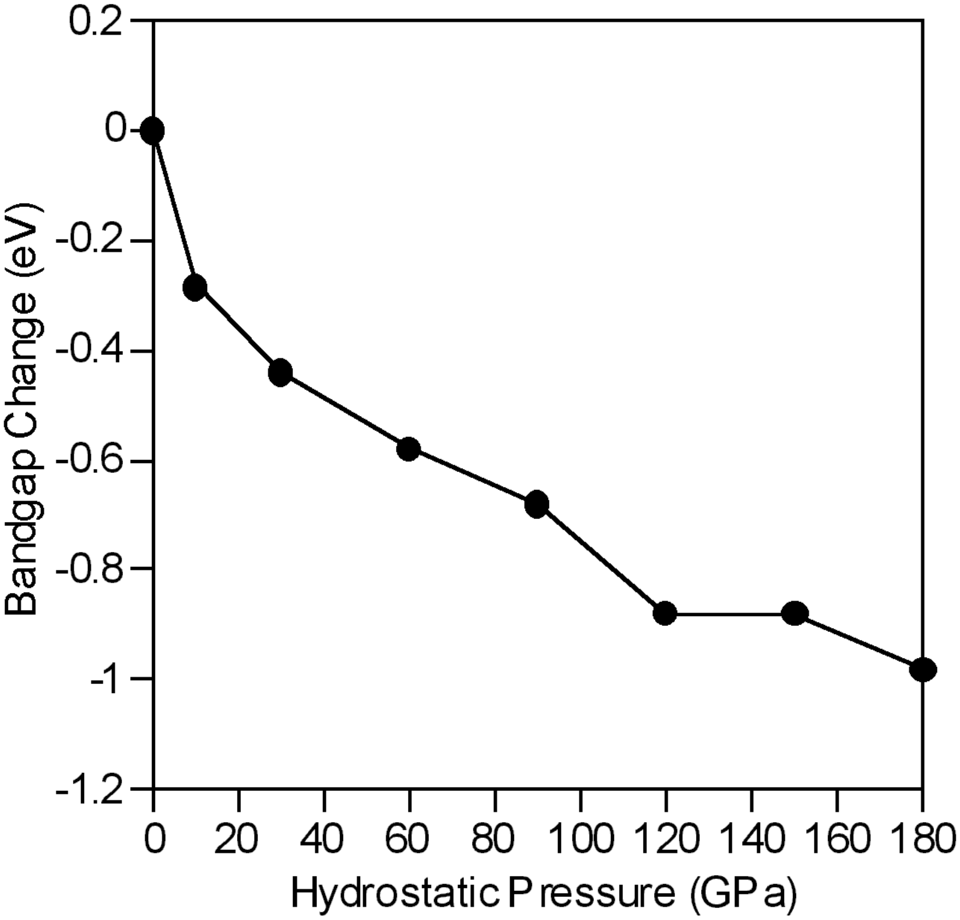

Figure 2-4: Nitromethane bandgap change as a function of hydrostatic pressure. All bandgaps are plotted relative to the zero pressure state.

2.3.2 Uniaxial compression

Before the crystal relaxes to a state of hydrostatic stress, a state of uniaxial strain exists immediately after the shock front passes. This uniaxial strain state may last for picoseconds or much longer, depending on the timescale for plastic deformation. The relaxation from this strain state may involve shearing along crystal slip planes or shear wave propagation.

The unit cell at zero pressure was uniaxially strained along each of the three lattice vectors and the molecules within the cell were relaxed at each strain state. Uniaxial strain destroys the $P2_12_12_1$ symmetry in cases of extreme strain. Figure 2-5 shows the relaxed unit cell upon strain of 0.3 along the c axis. There is no significant distortion of the molecular bond angles, although the molecules have reoriented. Figure 2-6 shows the stress in the direction of compression for each of the three compression axes.

Figure 2-7 shows the bandgap change as a function of compression along each of the three lattice axes. There does not appear to be any significant orientational dependence as a function of the strain axis. With the uniaxial strains associated with detonation around 0.2, the bandgaps are lowered to 3eV. As in hydrostatic compression, this lowering is not enough to allow a significant thermal population of conduction electrons.

If we move closer to the shock front, the molecules have insufficient time to reorient to relax the uniaxial strain. Shock compression without relaxation can be modeled by simply translating the molecules toward each other in the direction of uniaxial compression. This simplistic approach is intended to capture some of the dynamics of the compression in a static calculation.

Figure 2-8 shows the bandgap change as a function of compression without relaxation along each of the three lattice axes. The data indicate an orientational dependence, with the largest bandgap lowering occuring for compression along the c axis. Compression along this axis brings the nitro groups closer to methyl groups of neighboring molecules. In particular, it brings a hydrogen on one molecule directly

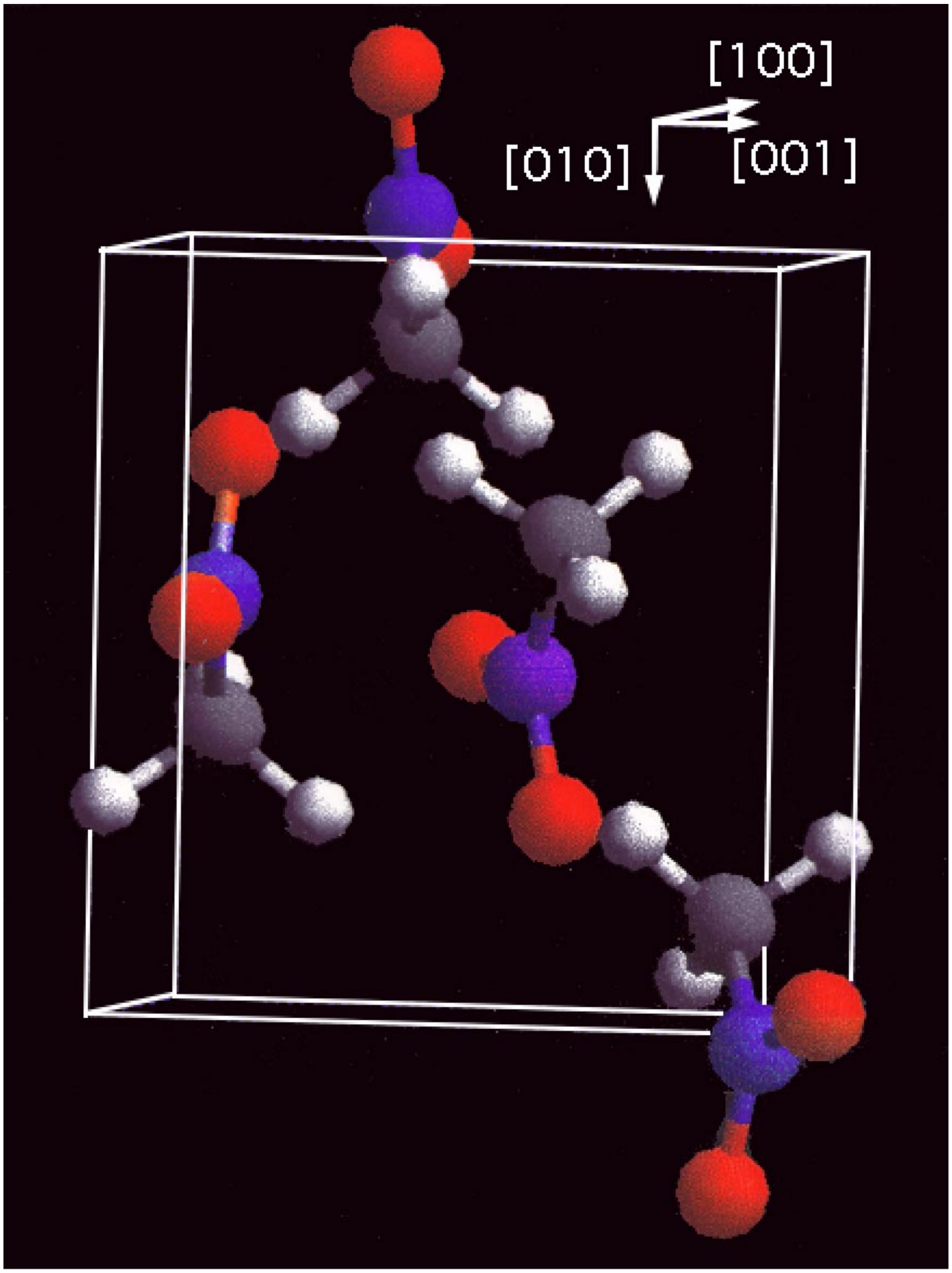

Figure 2-5: Nitromethane unit cell relaxed under a uniaxial strain of 0.35 (3.0 Å) along the c axis direction. Note the molecules are reoriented so that the nitro groups are closer to being in the ab plane than they are in the unstrained state.

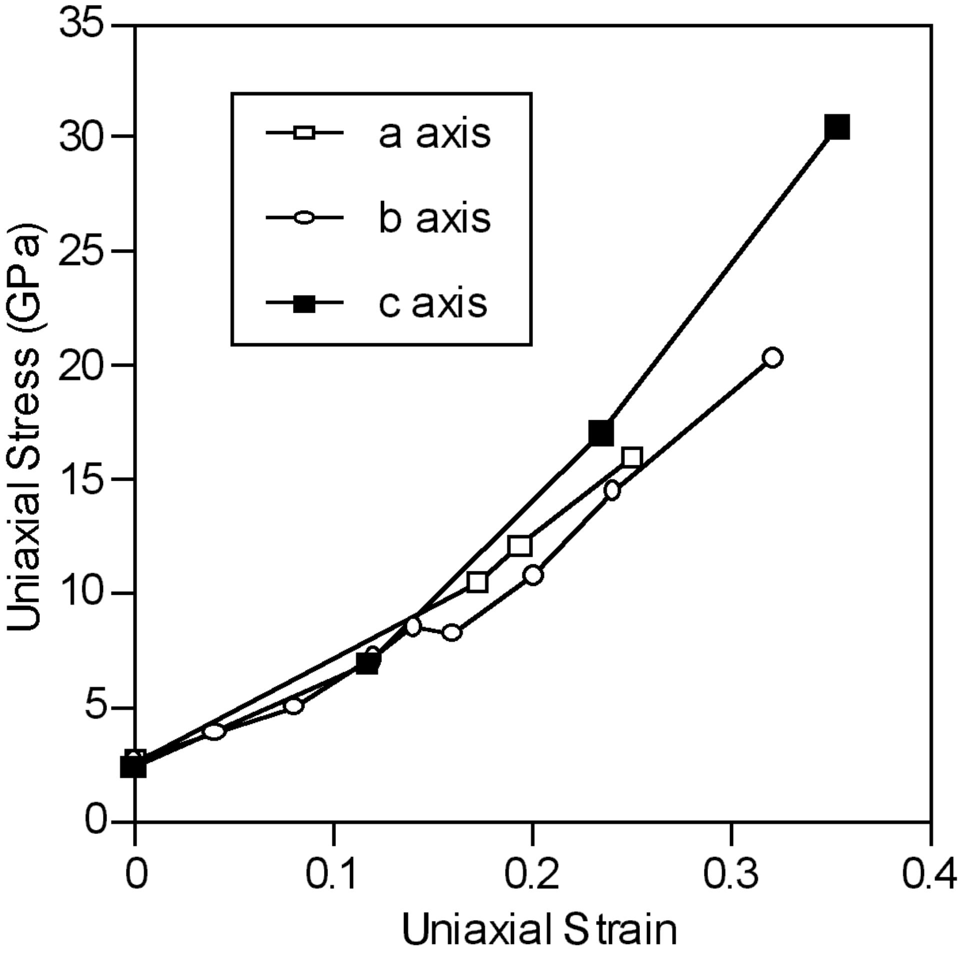

Figure 2-6: Nitromethane uniaxial stress in the direction of uniaxial compression.

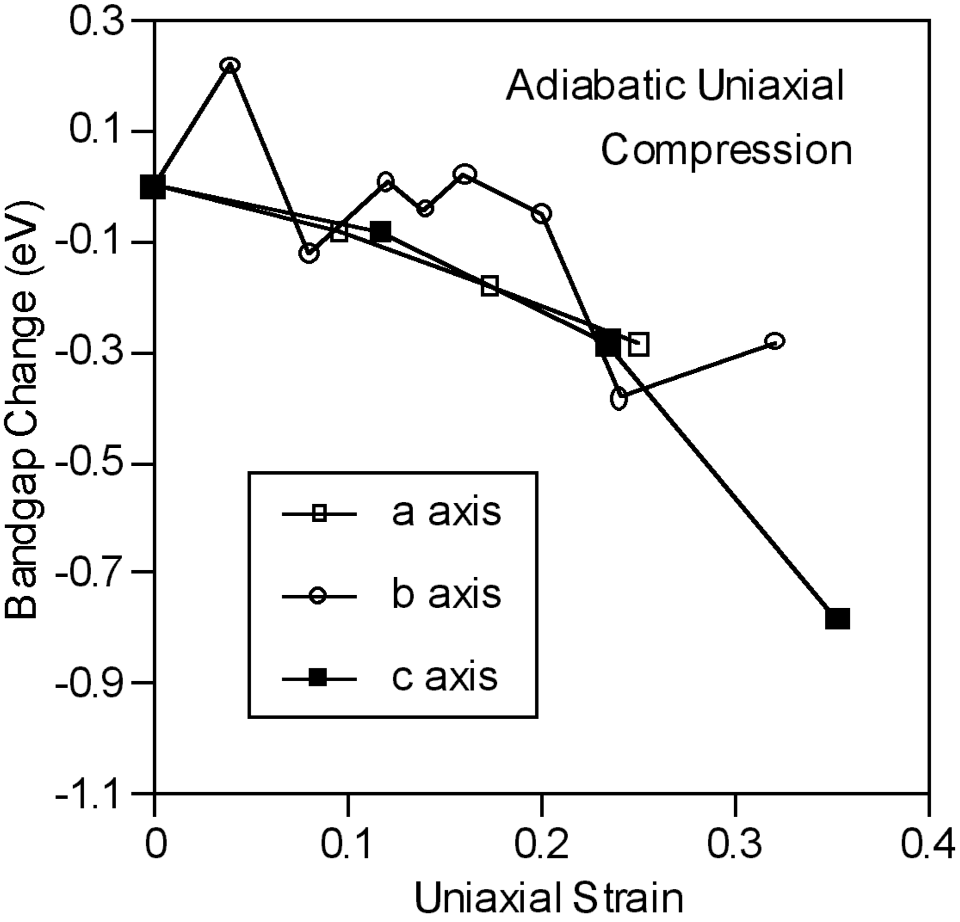

Figure 2-7: Nitromethane bandgap change as a function of uniaxial strain. Bandgaps are plotted relative to the unstrained state.

toward an oxygen on a neighboring molecule. Compression along the other directions does not bring close contact atoms on neighboring molecules directly towards each other. We expect this transient effect to be very short lived because the energy barrier for methyl rotation is only 170K at atmospheric pressure. The methyl groups will quickly rotate to avoid such a close contact between two atoms. This effect will be addressed in more detail in the section on dynamical effects. It is interesting to note that the a axis is a nearest neighbor direction while the b axis is not, yet the bandgap behavior as a function of compression is nearly identical for these two axes. This is likely due in part to the localization of the HOMO and LUMO states to the nitro group.

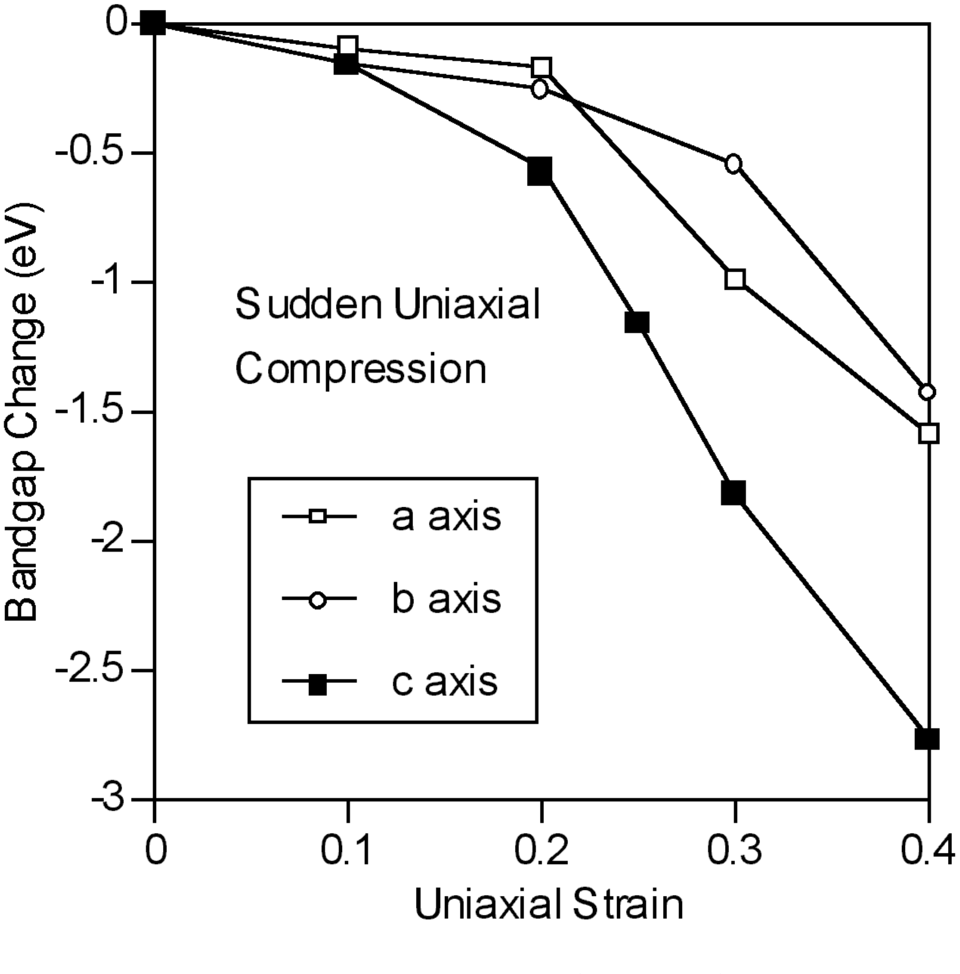

Figure 2-8: Nitromethane bandgap change as a function of uniaxial strain without unit cell relaxation. Bandgaps are plotted relative to the unstrained state.

A similar increased gap lowering for compression of molecules without relaxation was observed by Kuklja, *et. al.*[37] Without allowing the structure geometry to relax, RDX molecules were placed in a configuration resembling an edge dislocation. The bandgaps for the compressed and uncompressed structures were considerably lower than those for other model defect structures where molecules had been simply removed from the perfect crystal lattice. The removal of molecules from the relaxed lattice can be accomplished without creating close intermolecular contacts. However, we have observed here that relaxation of the lattice is very important to obtain a reliable bandgap for any other molecular configuration. A comparison of Figures 2-7 and 2-8 demonstrates this.

2.3.3 Shear

Strong positive correlations between the impact sensitivity and population of vacancies and defects in high explosives suggest that vacancies and defects play a key role in high explosive initiation. A state of shear strain may exist around defects or along slip planes as a result of the uniaxial compression that occurs at the shock front.

A static state of shear strain was modeled by varying the angle between the a and c lattice vectors (γ). This was done in two fashions: while keeping the lattice vector lengths fixed, and while adjusting the c vector length to keep the cell volume constant (constant density). A third state of shear was considered where the a lattice vector was increased while the c lattice vector was decreased such that the density remained constant. The results of these calculations are similar to those presented here.

Figure 2-9 shows the bandgap change as a function of γ for the variable and fixed density cases. Very little gap lowering results from the shearing in both cases. As in the hydrostatic compression and uniaxial compression, the molecules rearrange themselves but exhibit little geometric distortion.

2.3.4 Molecular defect

It has been suggested that defects in molecular crystals are sites where increased gap lowering can occur under pressure.[37] We consider, as a simple defect, a flipped

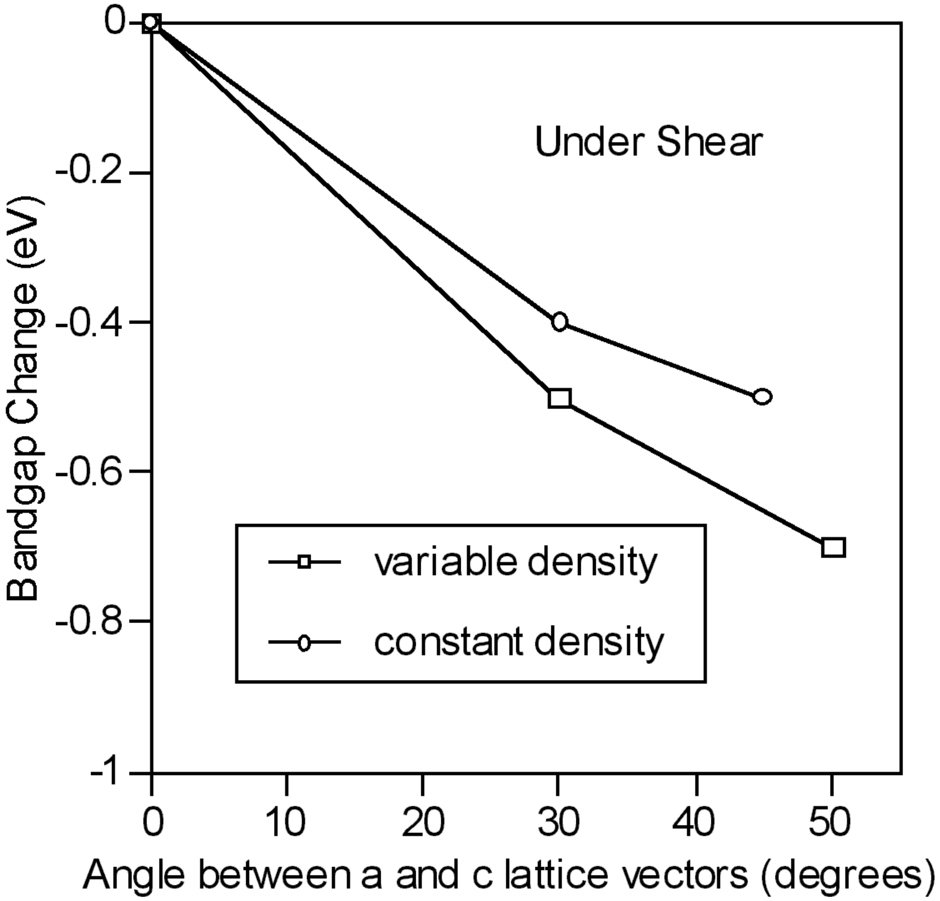

Figure 2-9: Nitromethane bandgap change as a function of unit cell shear. Bandgaps are plotted relative to the unstrained state. The angle between the a and c lattice vectors (γ) was varied. In one data set, the c lattice vector length was fixed at all angles. In the other set, the length was varied to keep a constant density at each angle.

molecule in the unit cell, as shown in Figure 2-10. The motivation for this defect is to increase the interactions between HOMO and LUMO states of the flipped molecule and HOMO and LUMO states of a neighboring molecule by bringing them closer together. In this defect configuration, the periodic boundary conditions create an infinite row of molecules along the c axis direction with neighboring nitro groups.

This structure was compressed uniaxially and relaxed, with bandgap change results in Figure 2-11. The molecular geometries upon compression are within 2-3% percent of the zero pressure values, with little or no bond distortion. The bandgap for the unstrained unit cell is about 3.0 eV, which is 0.3 eV lower than that of the perfect crystal. The bandgap decreases more quickly with uniaxial strain than it does for the perfect crystal, particularly at high strains. However, the bandgap still does not lower enough to produce a significant population of molecular excited states.

2.3.5 Molecular vacancy

Another type of lattice defect is a missing molecule. We have simulated such a defect by removing a single molecule from a 16 molecule supercell. Periodic copies of the vacancy are separated by about 9 Å in the unstrained configuration.

Relaxation of the vacancy in the unstrained lattice resulted in almost no distortion from the unperturbed lattice. The bandgap for the relaxed vacancy in the unstrained supercell was lowered about 0.4 eV from the perfect crystal bandgap. This result is on the scale of the energy difference between the perfect crystal bandgap and the HOMO-LUMO gap of an isolated molecule, which is due entirely to intermolecular interactions.

The supercell was strained to 80% and 60 % of the unstrained volume by straining all three lattice vectors by the same amount. The relaxed structures showed some molecular reorientation around the vacancy. However, all molecules showed little displacement from their perfect crystal locations.

Figure 2-12 is a comparison of the bandgaps for the system with and without the molecular vacancy as a function of volume strain. The unstrained data are under hydrostatic compression. The vacancy provides room for molecules to reorient to

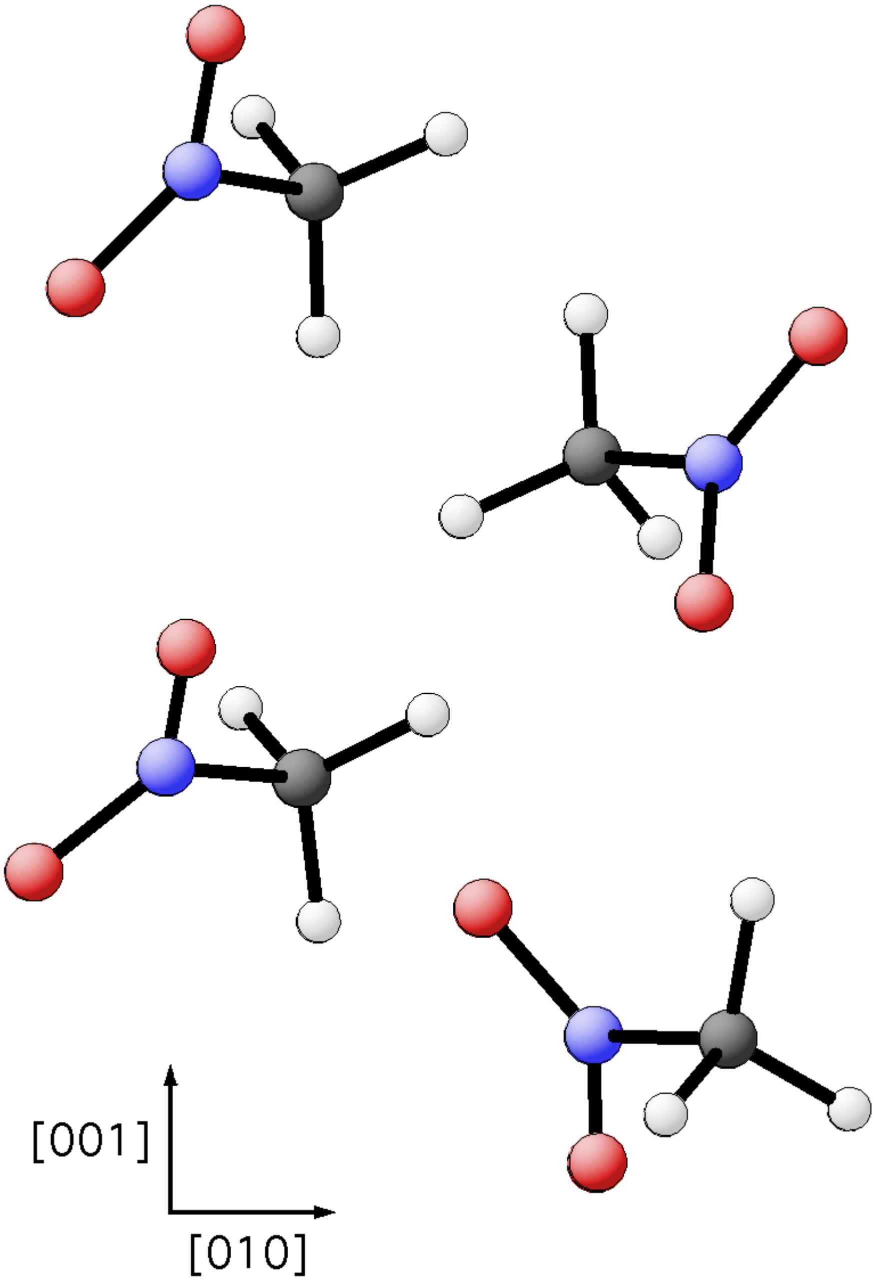

Figure 2-10: Nitromethane unit cell molecules with a flipped molecule defect. There is an infinite row of molecules along the [001] axis oriented in approximately the same fashion.

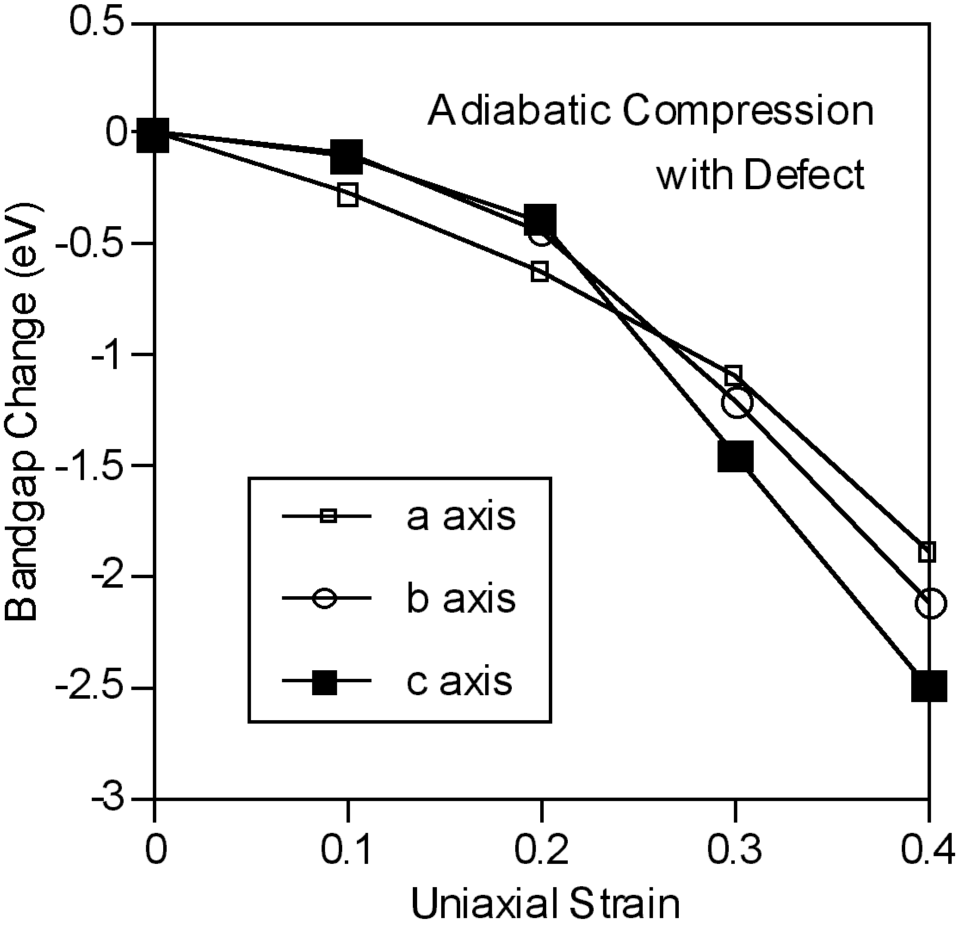

Figure 2-11: Nitromethane bandgap change for a unit cell with a molecular defect as a function of uniaxial strain. Bandgaps are plotted relative to the unstrained state, which has a bandgap about 0.5 eV lower that the perfect crystal in its unstrained state.

avoid bandgap-lowering close contacts. For this reason we might expect the bandgap to decrease less quickly with strain than for systems without a molecular vacancy.

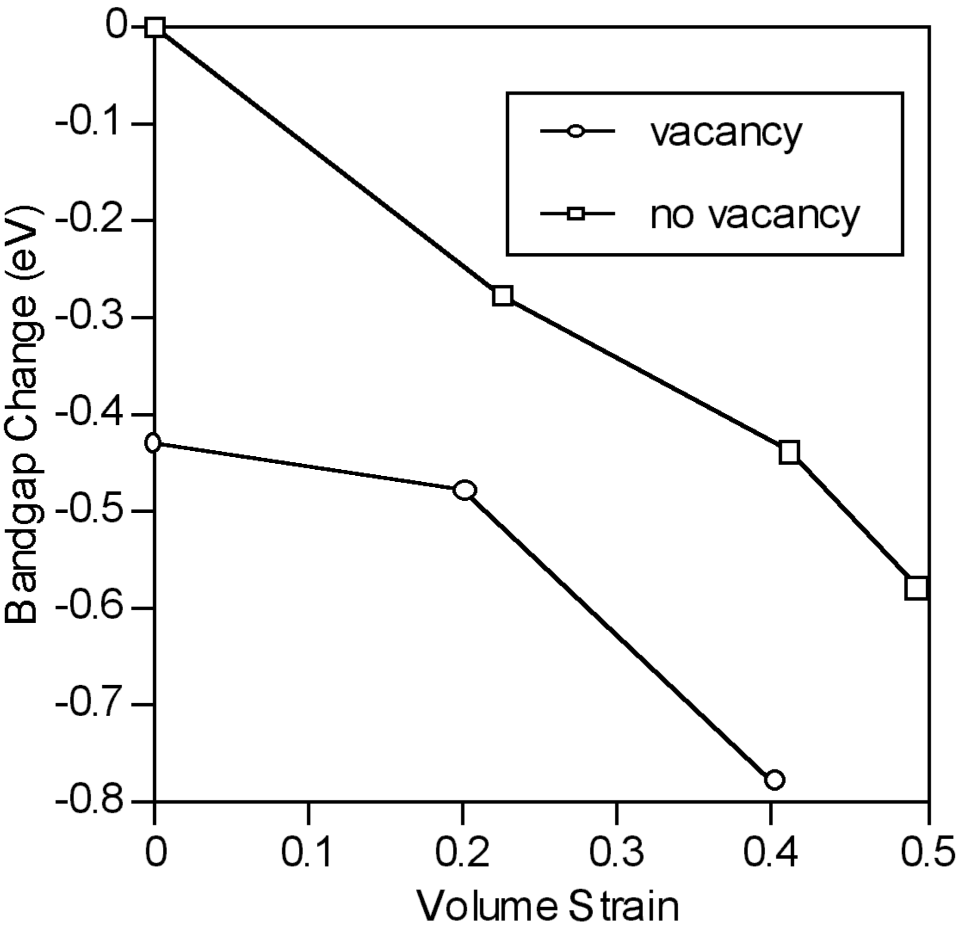

Figure 2-12: Nitromethane bandgap change for a unit cell with and without a molecular vacancy as a function of volume strain. Bandgaps are plotted relative to the unstrained states for each system.

These results are notably different from the results of Kuklja, *et. al.,* who have done Hartree-Fock calculations on RDX crystals with various configurations of molecular vacancies. [37] Bandgaps calculated with a form of perturbation theory correction decreased around 2 eV upon compression of the crystal to 80% of the unstrained volume. We may speculate that, in addition to comparing different materials, the different behavior may be due to the fact that relaxation of the molecular positions and geometries was allowed in the work here, in addition to the use a different theoretical approach to the bandgaps.

We can qualitatively summarize the results of all of the static calculations presented here with two points. The bandgap is not lowered enough to create significant thermal populations of excited states under static conditions with strain states comparable to or greater than those of detonation. Also, upon compression and relaxation, the molecules find a way to rearrange to maintain molecular geometries close to their zero pressure values. These two points suggest that if significant bandgap lowering is to occur, molecular bond distortion is required.

2.4 Dynamical effects

Our results indicate significant bond distortion in nitromethane requires the inclusion of dynamical effects. The lowest energy HOMO-LUMO crossing point found by Manaa, *et. al.,* occurs when the nitro group is flipped up out of the CNOO plane. The energy required in this bending mode for the HOMO-LUMO gap to be significantly lowered is about 3eV. With detonation temperatures around 2000K in nitromethane, only non-equilibrium processes can be expected to contribute such a large energy to a single bending mode on the molecule. The shock front is a region out of equilibrium where it may be possible for specific vibrational modes of the system to have transiently large populations. At 2000K, the total vibrational energy contained in a single molecule in the solid is about 3.5eV. Therefore it is at least conceivable that if energy on this scale is contained in a few molecular modes, significant gap lowering could occur via this mechanism. We will see that large changes in the perfect crystal bandgap are more likely to occur via dynamical effects than static effects.

2.4.1 Dynamical effects at the shock front

Once the molecules are uniaxially compressed by the shock, they rearrange to their relaxed geometries. It is possible that dynamical bond bending occurs during this rearrangement process. We modeled this process for a rapid shock compression along the c axis by doing constant energy *ab-initio* molecular dynamics starting with a unit cell with the molecules translated toward each other. The unit cell was also strained

0.2 along the c axis to reproduce the uniaxial strain associated with a roughly 13 GPa detonation wave. A 1 fs time step was used with a Verlet algorithm for integration of the equations of motion through about 270 fs. The internal temperature of the molecules was initially at T=0, with no vibrational energy. The bandgap started at 0.6 eV below the unstrained crystal bandgap and immediately increased. It did not dip below this value for the remainder of the simulation, which is consistent with the minimal bond distortion observed during the rearrangement.

The solid phase molecules exist in a face-centered cubic lattice, with 12 nearest neighbor molecules. Two neighbors are in the $[001]$ and $[00\bar{1}]$ lattice directions, two are along the $[100]$ and $[\bar{1}00]$ directions, and the remaining eight are along the $[221]$, $[\bar{2}21]$, $[2\bar{2}1]$, $[\bar{2}\bar{2}1]$, $[22\bar{1}]$, $[\bar{2}2\bar{1}]$, $[2\bar{2}\bar{1}]$, and $[\bar{2}\bar{2}\bar{1}]$ directions. The latter 8 nearest neighbors lie along four directions in the crystal which can be shown identical using the four group operations of the $P2_12_12_1$ symmetry. The periodicity of molecular orientations along these directions is four. It is two along the $[001]$ lattice direction, and one along the $[100]$ lattice direction.

By accounting for these symmetries and periodicities, we have done *ab-initio* molecular dynamics simulations of the molecular collisions associated with shock wave propagation along all nearest neighbor directions in the crystal. This was realized by colliding molecules along the three unique nearest-neighbor directions in the crystal. Collisions along the $[100]$ and $[221]$ lattice directions were accomplished using an 8 molecule supercell with the length of the a axis doubled.

Detonation waves in nitromethane propagate around 6 km/sec.[22] The molecular collision velocities at the shock front depend on the width of the front. This width can be as large as hundreds of molecules in crystals with defects and vacancies, or as short as a few molecules in perfect crystals. We expect the larger molecular collision velocities to be about 2 km/sec, which roughly corresponds to a shock front width of two or three molecules. However, molecular collision velocities near the shock velocity are not inconceivable in special cases.

Collisions along all three directions were calculated for collision velocities between 2 km/sec and 6 km/sec (between 0.02 Å/fs and 0.06 Å/fs). A 1 fs time step was used for the 2km/sec calculations and 0.5 fs was used for the higher collision velocities. All simulations were run for around 100 fs. The internal temperature of the molecules was initially at T=0, with no vibrational energy.

The maximum observed changes in the HOMO-LUMO gaps as a function of collision velocity are given in Figure 2-13. This gap minimum was obtained near the peak of the collision in all cases. Figure 2-13 indicates that the bandgap can be significantly effected at higher collision velocities , but it is still too large for a significant thermal population of excited states to exist.

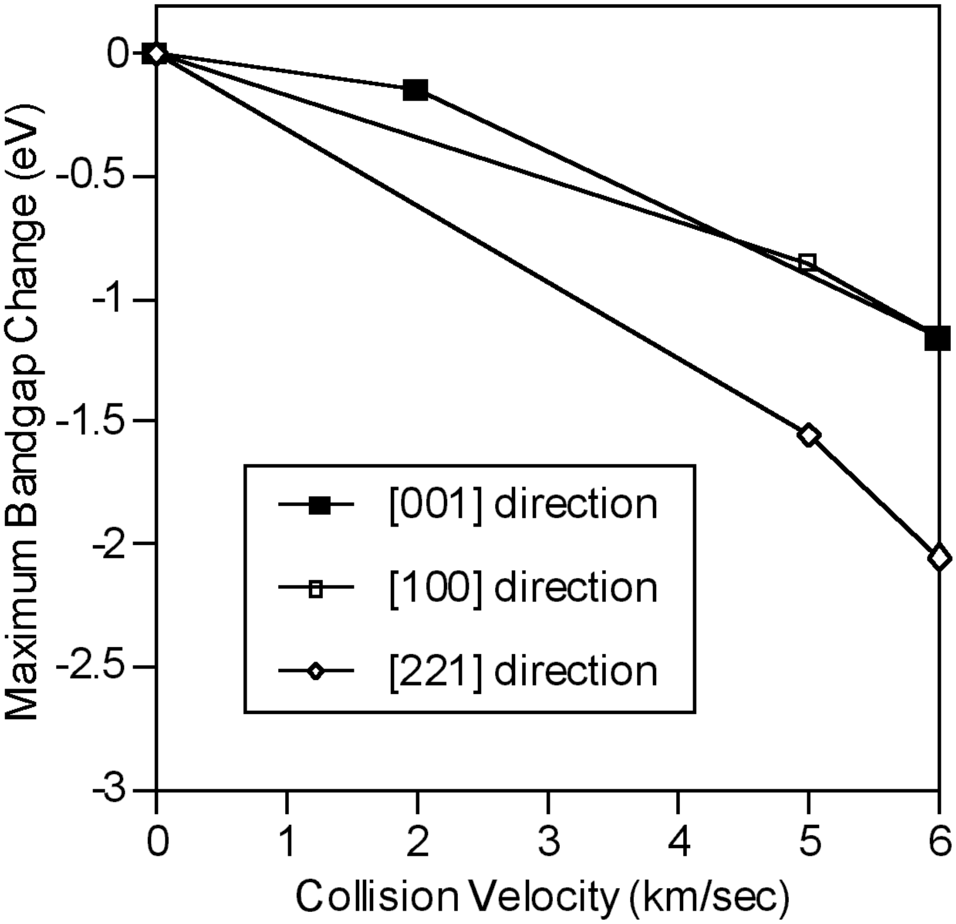

Figure 2-13: Maximum bandgap change attained during intermolecular collisions along nearest neighbor directions in the crystal. Bandgaps are plotted relative to the unstrained crystal bandgap.

Little bond bending or stretching was observed in the 2 km/sec collision, although some vibrational energy was deposited into the molecular modes. The 5 km/sec and

6 km/sec collisions showed large amounts of energy being transferred into the CN stretching and methyl rotation degrees of freedom. CN stretching vibrational amplitudes were around 15% after these collisions. The 6 km/sec collision along the [100] axis was also done using a GGA spin-polarized exchange-correlation functional.[52] Results obtained were identical to the non-spin-polarized exchange-correlation functional results.

A molecular collision of 10 km/sec along the c direction was also considered. This collision resulted in immediate rupture of the CN bond. The formation of new species lowered the bandgap 1.4eV. At the larger collision energies, energy sufficient for bond breaking may be directly channeled into bond breaking modes. This eliminates the need for a fast excited state decomposition mechanism.

2.4.2 Crystal shearing along a slip plane

For shock pressures greater than a few GPa, plastic deformation mechanisms can play a role in the energy transfer from the shock to molecular degrees of freedom. When a system is placed under uniaxial strain, it can plastically deform along slip planes to achieve a hydrostatic stress state. The presence of large vacancies can facilitate this strain relaxation mechanism. Dick, *et. al.,* have suggested that localized slip along sterically hindered slip planes in the crystal causes molecular bond distortion.[12]

Dick has proposed that detonation in nitromethane is most easily initiated when shocked along directions which require slip along sterically hindered slip planes to relieve the uniaxial stress.[10] As an exemplary sterically hindered slip system, we have considered slip along the (102) plane in the $[\bar{2}01]$ direction, which can be active for relief of uniaxial strain along the [001] direction. Figure 2-14 shows a view down this slip plane. The $[\bar{2}01]$ direction is into the page, and shearing is accomplished by moving the top and bottom planes directly into and out of the page.

Ab-initio molecular dynamics of slip along the (102) plane in the $[\bar{2}01]$ direction were done with an 8 molecule supercell with the a lattice vector doubled for proper boundary conditions. Slip along this system could result from uniaxial strain along the [001] direction. This axis was strained 0.2 and molecules relaxed. The molecules

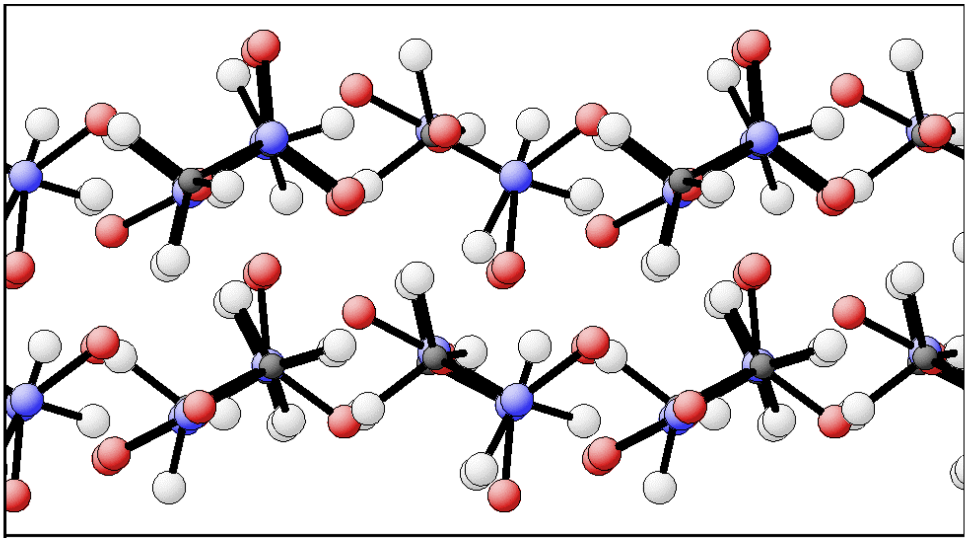

Figure 2-14: A view in the $[\bar{2}01]$ direction along the shearing plane. Shearing is accomplished by the bottom and top planes moving directly into and out of the page.

on opposite sides of the (102) plane were given velocities of 0.03 Å/fs in opposite directions along the $[\bar{2}01]$ axis. This velocity, which is near the shock velocity, is probably larger than might actually occur during slip, but it should accentuate dynamical effects and molecular distortion that occurs during slip. The periodicity of the simulation resulted in single-molecule planes travelling in alternately opposite directions. The simulation was run for 160 fs with a time step of 1 fs. The molecules were initially at T=0, with no vibrational energy.

The coherent motion of the molecules was dispersed after about 50 fs after making close to half of a lattice translation in the $[\bar{2}01]$ direction. After this point the system appeared to be transforming to a molecular liquid. After 140 fs, molecular CN bonds began to break. A HOMO-LUMO gap dropped 1.6eV at its lowest in the time observed. This gap lowering is similar to the lowering for the nearest-neighbor molecular collisions of the same 6 km/sec velocity. The HOMO-LUMO gaps appeared to gradually decrease as the energy from translational motion of the molecules was transferred into the molecular vibrational modes. Some bond bending was observed, but no significant bending of the nitro group out of its plane was observed. Bond bending during the shearing process seems to have been largely avoided through the rotation of the methyl group. Stresses that might have resulted in bond bending in more rigid molecules were relaxed by rotation of the CN bond axis. This particular molecular mode was observed to be the recipient of a significant amount of the shearing energy.

2.5 Discussion

The work of Manaa, *et. al.,* suggests extreme molecular distortions are required to close the HOMO-LUMO gap in nitromethane. However the intermolecular interactions in nitromethane are probably too weak to allow for such significant covalent bond distortion within the molecules under static conditions.

If bandgap closure does occur, it is most likely to be the result of dynamical effects that may occur around defects and vacancies or during shearing of the molecular crystal. The HOMO-LUMO gap decreases observed at high velocities in the dynamical simulations were much more significant than the bandgap decreases for the perfect crystal under realistic static conditions. These dynamical bandgap changes were comparable in magnitude to the molecular defect bandgap changes for large values of uniaxial strain. Perhaps dynamical effects which involve high velocity collisions between the nitro groups of defect molecules are one of the most likely sources of electronic excitations.

The work of Manaa, *et. al,* suggests roughly 3eV must be channeled into the CNOO bending mode for the HOMO-LUMO gap to significantly decrease. With temperatures associated with detonation in the 0.2 eV range, this can only occur in regions far from equilibrium where energy from the shock has good coupling into this mode. It may, however, be possible for molecular decomposition to occur before such extreme energies are possessed in any single molecular degree of freedom. For example, an energy of 3eV in the CN stretching mode will result in dissociation of the methyl and nitro groups.[43]

Some speculation may be made about the role of electronic excited states in the detonation of other high explosives like TATB and TNT. These molecules are larger than nitromethane and may have fundamentally different electronic structures. If the HOMO and LUMO states are localized on the nitro groups, as in nitromethane, then we would not expect significant bandgap lowering to occur under compression or around defects. Larger molecules may, however, be more susceptible to bond bending during shearing processes than nitromethane due to the lack of a single freely rotating methyl group which adjusts to relieve molecular strain on the whole molecule. One might generally expect the slip planes of crystals of larger molecules to be more sterically hindered than nitromethane, which could increase the likelihood of bond bending. However, larger molecules have more bonds to relax applied stresses, which might lower the chances of any single bond being excessively stressed. In light of these observations, it is not clear how to rigorously extrapolate the nitromethane results to larger molecules. However, the similarly weak intermolecular interactions in these materials under normal conditions sheds some degree of doubt on the likelihood of significant bandgap lowering under shock loading.

2.6 Summary

We have observed in this work that under the conditions of hydrostatic stress, uniaxial strain, and shear strain associated with shock loading in a detonation wave, the bandgap of crystalline nitromethane and nitromethane with molecular defects and vacancies does not decrease enough for a significant thermal population of molecular excited states. Under these conditions, the molecules rearrange such that no significant molecular geometric distortion occurs. This is facilitated by the nearly free rotation of the molecule along the CN bond axis, which adjusts to minimize stress on the molecule. The localization of the HOMO and LUMO states on the nitro group also plays a role in this result. We also expect little geometric distortion and bandgap lowering to occur around larger defects and vacancies for these reasons.

We have also modeled the molecular collisions at shock fronts and during shearing of the crystal. It was determined that if significant bandgap lowering occurs, it is most likely to occur via dynamical effects. However, molecular collision velocities in excess of 6 km/sec appear to be required to produce a significant thermal population of molecular excited states. The nearly free rotation of the methyl group plays a key role in relaxing stresses on the molecule during these dynamical simulations.

The small methyl group rotation barrier and the localized nature of the HOMO and LUMO states of nitromethane appear to be the biggest factors in keeping the bandgap relatively large during shock conditions. For these reasons, the extension of these results to larger explosive molecules like TATB and TNT is not clear. The possibility of electronic excitation in these materials certainly deserves careful investigation.

Chapter 3

Tractable dynamical molecular dynamical studies of shock compression

A new multi-scale simulation method is formulated for the study of shocked materials. The method combines molecular dynamics and the Euler equations for compressible flow. Treatment of the difficult problem of the spontaneous formation of multiple shock waves due to material instabilities is enabled with this approach. The method allows the molecular dynamics simulation of the system under dynamical shock conditions for orders of magnitude longer time periods than is possible using the popular non-equilibrium molecular dynamics (NEMD) approach. An example calculations are given for model potentials for silicon in which a computational speedups of 10^5 and 10^8 are demonstrated. Results of these simulations are consistent with the recent experimental observation of an anomalously large elastic precursor on the nanosecond timescale.

3.1 Introduction

Study of the propagation of shock waves in condensed matter has led to new discoveries ranging from new metastable states of carbon[74] to the metallic conductivity of hydrogen in Jupiter[48, 71] to the possibility of delivery of life to planets via meteorite impact.[18] Shock waves are currently the only practical way to simultaneously probe the high temperature and high pressure behavior of matter, but progress in understanding the microscopic details of shocked materials has been extremely difficult. Highly non-equilibrium regions may exist that give rise to the formation of unexpected metastable states of matter and determine the structure, instabilities, and time-evolution of the shock wave.[34, 40, 65, 54] Some progress in understanding these microscopic details can be made through molecular dynamics simulations.[33, 20, 35, 26] The popular non-equilibrium molecular dynamics (NEMD) approach to atomistic simulations of shock compression involves creating a shock on one edge of a large system and allowing it to propagate until it reaches the other side. The computational work required by NEMD scales at least quadratically in the evolution time because larger systems are needed for longer simulations. When quantum mechanical methods with poor scaling of computational effort with system size are employed, this approach to shock simulations rapidly becomes impossible. Another approach that utilizes a computational cell moving at the shock speed has the same drawbacks.[77] This Chapter presents a method which circumvents these difficulties by requiring simulation only of a small part of the entire system. The effects of the shock wave passing through this small piece of the system are simulated by dynamically regulating the applied stress which is obtained from a continuum theory description of the shock wave structure. Because the size of the molecular dynamics system is independent of the simulation time in this approach, the computational work required to simulate a shocked system is nearly linear in the simulation time, circumventing the scaling problems of NEMD.

Molecular dynamics simulations have been performed that utilize a shock Hugoniot-based thermodynamic constraint for the temperature at fixed volume.[41] This approach is a thermodynamic one for a single shock wave and fails to capture the spontaneous formation of multiple shock waves and dynamical effects like long-lived metastable phases, elastic-plastic phase transitions and chemical reactions, which are ubiquitous in shocked condensed matter. The new method outlined in this Chapter is a method for the dynamical simulation of shock waves that solves these problems. It enables the *dynamical* simulation of shock waves in systems that have material instabilities which lead to the formation of multiple shock waves and chemical reactions that can change the speed of shock propagation with time. It is a tractable method that requires no *a priori* knowledge of the system phase diagram, metastable states, or sound speeds.

3.2 Method for simulation of a single shock wave

We model the propagation of the shock wave using the 1D Euler equations for compressible flow, which neglect thermal transport,

$$\frac{d\rho}{dt} + \rho u_x = 0 \tag{3.1}$$

$$\frac{du}{dt} + v p_x = 0 \tag{3.2}$$

$$\frac{de}{dt} + p\frac{dv}{dt} = 0 \tag{3.3}$$

Here u is the local speed of the material in the laboratory frame (particle velocity), v is the specific volume, $\rho = 1/v$ is the density, e is the energy per unit mass, and p is the negative component of the stress tensor in the direction of shock propagation, $-\sigma_{xx}$. The complete time derivatives are $\frac{df}{dt} \equiv f_t + uf_x$ and subscripts denote partial derivatives. These equations represent the conservation of mass, momentum, and energy respectively everywhere in the wave. Neglecting thermal transport in high temperature shocks is valid in systems where electronic mechanisms of heat conduction are not important, i.e. usually less than a few thousand K in insulators.[76] While continuum theory is not rigorously applicable at elastic shock fronts which can be atomistically sharp, the correct dynamics will be approximated in these special regions. We seek solutions of these equations which are steady in the frame of the shock wave moving at speed $\mathrm{v_s}$. We consider the variables to be functions of $x - \mathrm{v_s}t$, in which case $\frac{\partial}{\partial t}$ becomes $-\mathrm{v_s}\frac{\partial}{\partial x}$. This substitution, and integration over x yields a variation of the Hugoniot relations,

$$u = \mathrm{v_s}\left(1 - \frac{\rho_0}{\rho}\right), \tag{3.4}$$

$$p - p_0 = \mathrm{v_s}^2 \rho_0 \left(1 - \frac{\rho_0}{\rho}\right), \tag{3.5}$$

$$e - e_0 = p_0\left(\frac{1}{\rho_0} - \frac{1}{\rho}\right) + \frac{\mathrm{v_s}^2}{2}\left(1 - \frac{\rho_0}{\rho}\right)^2. \tag{3.6}$$

Variables with subscripts 0 are the values before the shock wave, and we have chosen $u_0 = 0$, i.e. the material is initially at rest in the laboratory frame. In the language of shock physics, Eq. 3.5 for the pressure is the Rayleigh line and Eq. 3.6 for the internal energy is the Hugoniot at constant shock velocity. These equations apply to a system which has a time-independent steady-state in the reference frame moving at the shock speed $\mathrm{v_s}$.

For the molecular dynamics simulation, we employ the Lagrangian,

$$L = T\left(\{\dot{\vec{r}}_i\}\right) - V\left(\{\vec{r}_i\}\right) + \frac{1}{2}Q\dot{v}^2 + \frac{1}{2}\frac{\mathrm{v_s}^2}{v_0^2}(v_0 - v)^2 + p_0(v_0 - v) \tag{3.7}$$

where T and V are kinetic and potential energies per unit mass, and Q is a mass-like parameter for the simulation cell size. It can be seen that Eq. 3.7 implies Eq. 3.6 when $\dot{v} = 0$ because $T + V = e$. The equation of motion for the system volume is,

$$Q\ddot{v} = \frac{\partial T}{\partial v} - \frac{\partial V}{\partial v} - p_0 - \frac{\mathrm{v_s}^2}{v_0^2}(v_0 - v) \tag{3.8}$$

which reduces to Eq. 3.5 when $\ddot{v} = 0$. We use the scaled atomic coordinate scheme of Ref [1] to deal with the variable computational cell size. This scheme introduces a volume dependence for T and V. Strain is only allowed in the shock direction, i.e. $v_0 - v = -\epsilon_{xx} v_0$ where ϵ_{xx} is the uniaxial strain. The pressures in Eq. 3.8, including the thermal contribution, are taken to be the uniaxial x component of stresses. Computational cell dimensions transverse to the shock direction are fixed, as in NEMD simulations. This approach allows the simulation of shocks propagating in any direction which is difficult or impossible with NEMD.

Simulation of a single shock wave may be accomplished by dynamically varying the uniaxial strain of the system according to Eq. 3.8. By choosing a small representative sample of the shocked material, it is assumed that stress gradients and thermal gradients in the actual shock wave are negligible on the length scale of the sample size. While the thermal energy is assumed to be evenly distributed throughout the sample, thermal equilibrium is not required.

To simulate a shock to a given pressure, the initial state parameters which define the MD constraint in Eq. 3.7 are chosen (ρ_0, p_0, e_0.) A guess for $\mathrm{v_s}$ is made for the constraint to take the system to the desired final pressure. If the final pressure is other than the desired one, improved guesses for $\mathrm{v_s}$ can be made and simulated again until the desired $\mathrm{v_s}$ is determined. The final shock pressure increases with increasing $\mathrm{v_s}$. The simulation of a shock to a given particle velocity using this approach is a straightforward extension.

3.3 Stability of simulated waves

There are two criteria for the mechanical stability of a shock wave.[15] The first one requires $\mathrm{v_s} > c_0$, where c_0 is the speed of sound in the pre-shocked material. The second criterion requires $u_1 + c_1 > \mathrm{v_s}$, where the subscript 1 denotes the post-shock state.

The constraints of Eq. 3.5 and 3.6 take the system through states which satisfy these stability criteria. The line between points A and E in Figure 3-1 depicts a Rayleigh line for a single shock on a Hugoniot. Points A and E are stationary points of Eq. 3.8. The Rayleigh line slope magnitude must be greater than the Hugoniot slope at point A to be an unstable stationary point of Eq. 3.8, and vice-versa at point E to be a stable point of Eq. 3.8. These conditions are required for the compression to proceed up along the Rayleigh line.

The Hugoniot and isentrope have a first-order tangent at point A. Therefore the stability condition $c_0 < \mathrm{v_s}$ is automatically satisfied at point A if compression proceeds up along the Rayleigh line since the Rayleigh line slope is $-\frac{\mathrm{v_s^2}}{v_0^2}$ and the Hugoniot

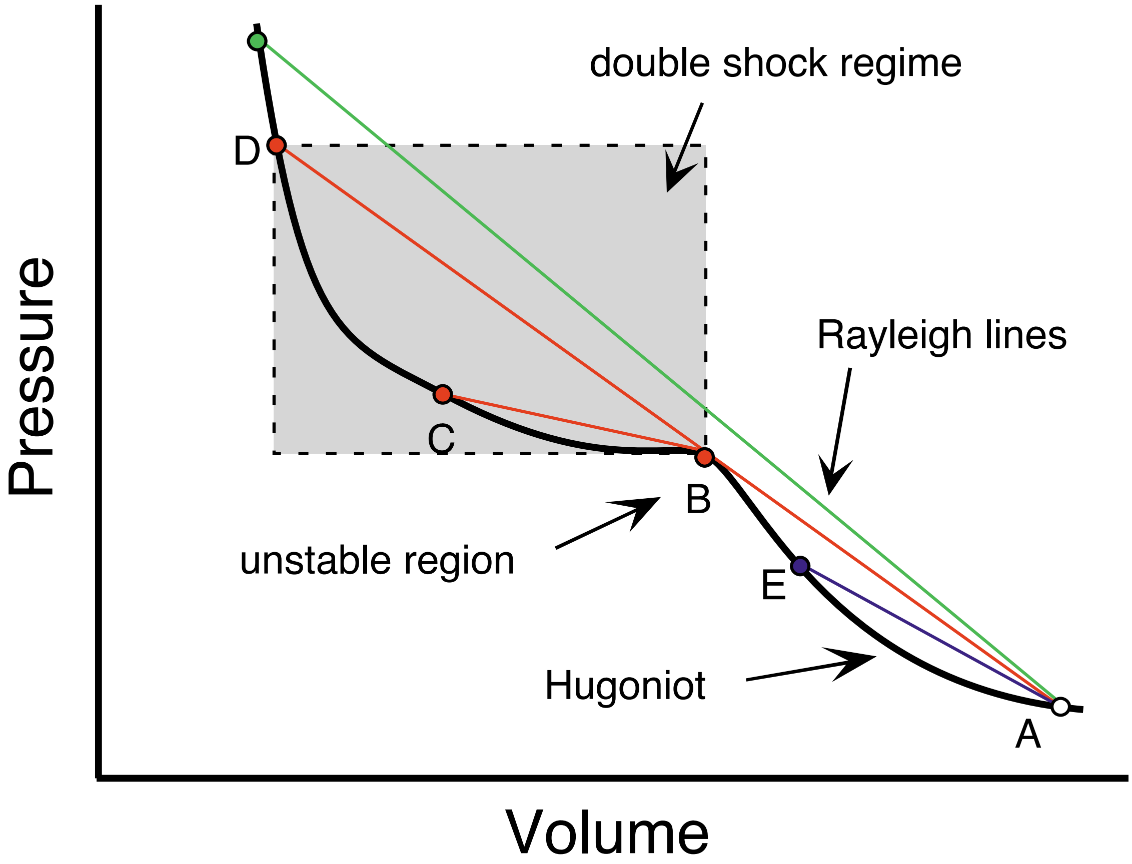

Figure 3-1: Rayleigh lines on a hypothetical Hugoniot.

slope is $-\frac{c_0^2}{v_0^2}$. Furthermore, since the Rayleigh line slope magnitude is less than the Hugoniot slope at point B, it can be shown that $u_1 + c_1 > \mathrm{v_s}$ which is the other stability condition. Therefore the constraint Eq. 3.8 has stable points only where the shock waves are stable.

3.4 Treatment of multiple shock waves

The above method describes the simulation of a single stable shock wave. However, it is not always possible to shock to a given pressure or particle velocity using this technique. For example, Figure 3-1 shows how it may not be possible to connect a straight Rayleigh line to all final pressures when there is a region of negative curvature in the Hugoniot, $\frac{d^2p}{dv^2} < 0$. Such regions of negative curvature are common in condensed phase materials and may be a result of phase transformations or may be the shape of a single phase Hugoniot. In Figure 3-1, it is not possible to connect state A to any state between B and D with a straight Rayleigh line. Therefore it is not possible for a single shock wave to compress the system to a pressure between that of states B and D. While a single Rayleigh line is insufficient to meet the pressure boundary condition in this region, two Rayleigh lines are sufficient. The first goes from A to B and is tangent to the Hugoniot at point B. This tangency implies $u_B + c_B = v_{s,AB}$ at point B which is a point of instability. Therefore the wave from A to B terminates and a second wave forms from B to C. The mechanical stability criteria are satisfied at points A and C.

Figure 3-2 shows a flowchart that illustrates how to determine the set of Rayleigh lines that are stable and meet the boundary conditions without any *a priori* knowledge of the system. A shock wave instability exists when the boundary condition falls within a discontinuity in the set of final pressures as a function of shock speed, as in the inset figure in Figure 3-2. The existence of such a discontinuity can be determined when sufficient trial values of $\mathrm{v_s}$ have been simulated. If the boundary condition falls within the discontinuity, the entire process is repeated with point B as the initial state to find the shock speed that meets the boundary condition. If further instabilities are

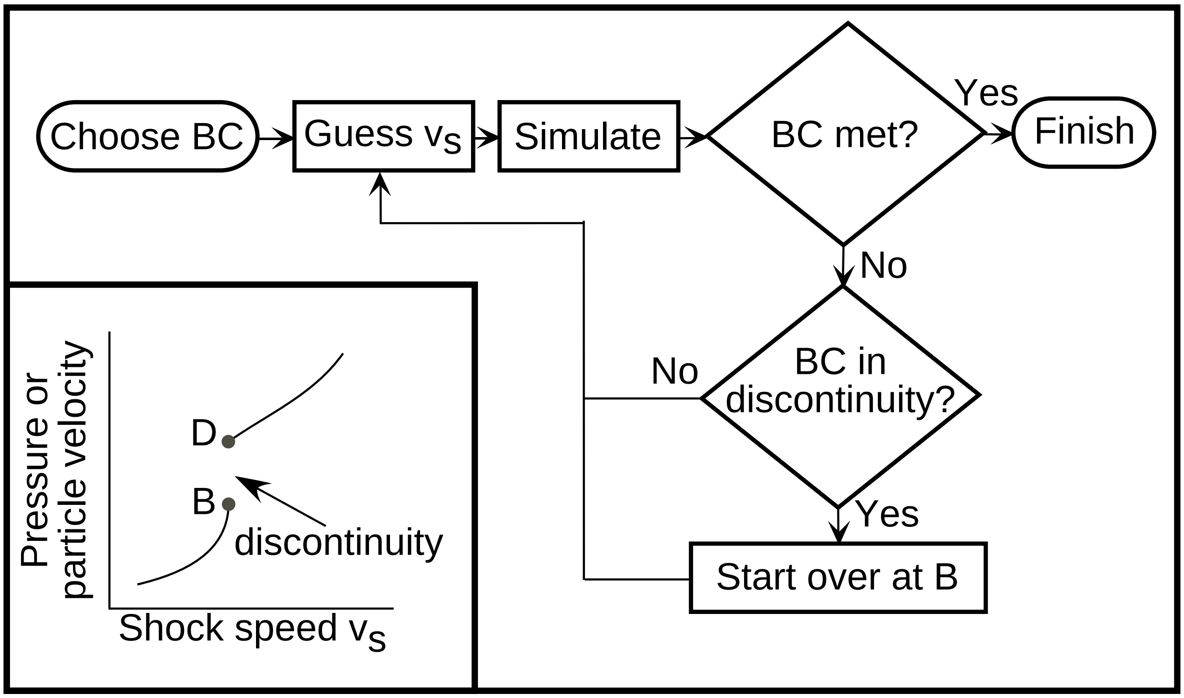

Figure 3-2: Flowchart for simulation of a shock to a chosen pressure or particle velocity boundary condition (BC). Instabilities due to regions where $\frac{d^2p}{dv^2} < 0$ along the Hugoniot can give rise to a discontinuity in the inset plot.

discovered that prevent the boundary condition from being met with a single shock, the process is continued.

3.5 Time-dependence of the p-v space path

The formation and evolution of multiple waves becomes more complicated when chemical reactions or phase transitions occur. Volume decreasing phase transformations cause the pressure at point B in Figures 3-1 and 3-2 to decrease with time. Parameterization of the p-v space path with Rayleigh lines is valid when the timescale of this pressure change is less than the time required for a material element to reach the final shocked state.

The rate at which the pressure at point B decreases can be determined using the shock change equation.[32, 17] If we assume the internal energy is $e = e(p, v, \lambda)$, where λ is the reaction parameter for the phase transition, then the rate of pressure change in the moving frame of the shock wave at the metastable point B is given by,

$$\frac{dp}{dt}|_{\mathrm{v_s}} = \frac{\rho(u - \mathrm{v_s})^2 \alpha \dot{\lambda}}{2}. \tag{3.9}$$

Here, λ ranges between 0 and 1, $\alpha = \rho \frac{\partial v}{\partial \lambda}|_{p,H}$, where H is the enthalpy, and we have made use of the fact that $\mathrm{v_s} - u = c = \sqrt{\frac{\partial p}{\partial \rho}|_{s,\lambda}}$ and $\frac{\partial u}{\partial p}|_{Hugoniot} = \frac{\partial u}{\partial p}|_{Rayleigh} = \frac{1}{\rho_0 \mathrm{v_s}}$ at the point of instability where the Hugoniot and Rayleigh lines share a common tangent. We take the parameter $\alpha\dot{\lambda}$ to be $\frac{\delta v}{v \delta t}$ where δt is the time required for a volume change δv at the start of chemistry or plastic deformation, which is taken to be the point where the rate of simulation compression is slowest.

The approximation of the p-v space path by more than one Rayleigh line in the case of volume decreasing reactions is justified when the Rayleigh lines do not change appreciably during the simulation,

$$\frac{dp}{dt}|_{\mathrm{v_s}} << \frac{\Delta p}{\Delta t}, \tag{3.10}$$

where Δp and Δt are the pressure change and time duration of a given simulation respectively. In a two-shock wave, the time the system spends going from the initial state to the final state Δt is a function of the shock speeds associated with each wave, and is linear in time and the difference between wave speeds. In the long time limit, $\frac{dp}{dt}|_{\mathrm{v_s}}$ decreases exponentially with time.[15] Therefore, the Rayleigh line validity condition is satisfied in the long simulation time limit. During times when this condition is not satisfied, the *p*-*v* space path a material element follows is more complicated than straight Rayleigh lines, but such situations are transient.

3.6 Application to an elastic-plastic transition in silicon

As a first illustrative example, we apply the new method to an elastic-plastic transition in a model potential for silicon. The elastic-plastic transition is characterized by irreversible deformation from the elastically strained material state. Elastic-plastic transitions are common in most shocked solid phase systems.

Figure 3-3 shows shock speed as a function of particle velocity for shock waves propagating in the [011] direction in silicon described by the Stillinger-Weber potential.[62] This potential has been found to provide a qualitative representation of condensed properties of silicon. Data calculated using the NEMD method are compared with results of the new method presented in this Chapter. NEMD simulations were done with a computational cell of size 920Å × 12Å × 11Å unit cells (5760 atoms) for a duration of about 10-20ps. Simulations with the new method were done with a computational cell size of 19Å × 12Å × 11Å unit cells (120 atoms). Both simulations were started at 300K and zero stress. Since the NEMD simulations were limited to the 10ps timescale by computational cost, simulations with the new method were performed to calculate the Hugoniot on this 10ps timescale for comparison. The final particle velocity in these simulations was taken to be a point of steady state after a few ps. The Rayleigh line validity condition Eq. 3.10 is satisfied for the simulations performed in the two-shock regime, giving a typical value for $\frac{dp}{dt}|_{v_s}$ of 0.1 GPa/ps,

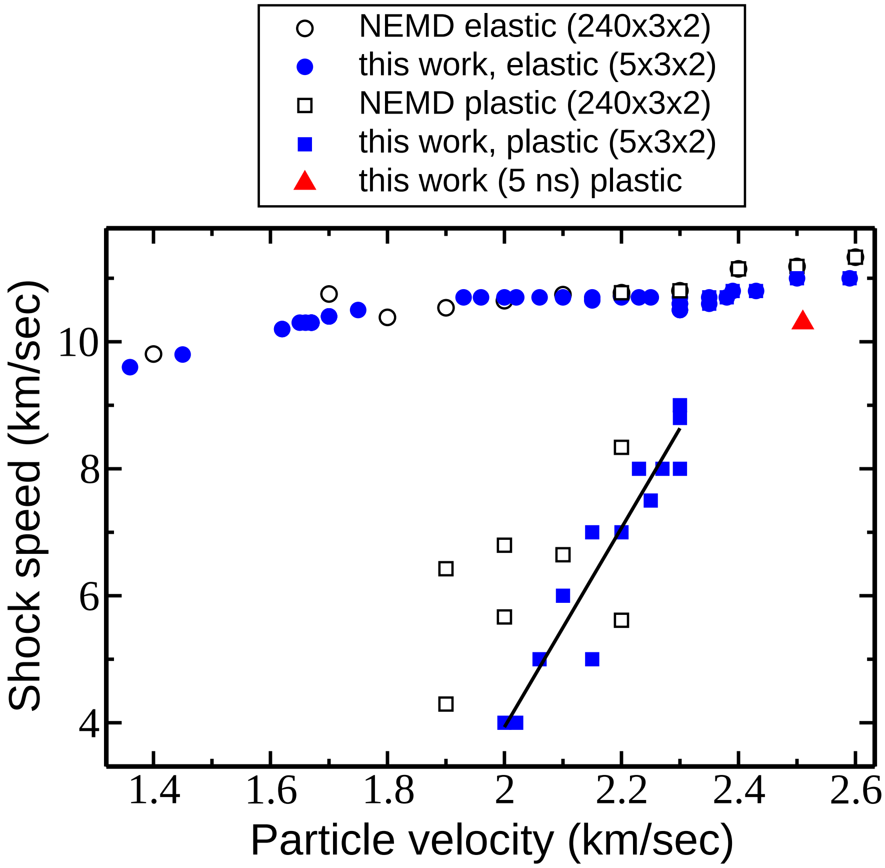

Figure 3-3: Comparison of calculated Hugoniots for the NEMD approach and the method presented in this Chapter for roughly 10 ps runs. Note the ability to utilize much smaller computational cell sizes with the new method. Also included is one data point for a 5 ns simulation using this work which would be prohibitive with NEMD requiring a factor of 10^5 increase in computational effort.

while $\frac{\Delta p}{\Delta t}$ is always greater than 0.5 GPa/ps for all simulations in Figure 3-3.

Figure 3-3 indicates a single shock wave exists below 1.9 km/sec particle velocity. Above this particle velocity, an elastic shock wave preceeds a slower moving shock characterized by plastic deformation. Agreement between the two methods is good for all regions except for the plastic wave speed for particle velocities less than 2.1 km/sec. The wide range of values for the plastic wave speeds in NEMD simulations in this regime is due to lack of adequate simulation time to reach a steady state plastic wave speed. Plastic deformation occurs slowly in NEMD simulations in this regime, while it tends to occur all at once in the relatively small simulation cell used for the new method. Therefore the new method tends to reach the final particle velocity more quickly than the NEMD simulations. Better agreement on short timescales in this regime can be obtained by conducting longer NEMD simulations and by using a larger simulation cell for the new method simulations.

One of the primary advantages of using the method outlined in this Chapter is the ability to simulate for much longer times than is possible with NEMD. As an example, Figure 3-3 shows the result of a 5 ns simulation performed along a Rayleigh line corresponding to a shock speed of 10.3 km/sec. The uniaxially compressed elastic state required 5 ns to undergo plastic deformation. The difference in particle velocity between the 10 ps and 5 ns simulations at this shock speed is 0.8 km/sec, suggesting that the elastically compressed state is metastable with an anomalously large lifetime. This is consistent with experimental observations of shocked silicon that indicate an anomalously high pressure elastic wave exists on the nanosecond timescale.[40] In addition to the simulations performed with the Stillinger-Weber potential, we have performed more accurate tight-binding[57] 120 atom simulations using the method of this Chapter that also suggest an anomalously high pressure elastic wave precursor exists on the 10 ps timescale.

This simulation done with NEMD would require *more* than 5 ns simulation time due to the time required for the equilibration of the first and second wave speeds according to Eq. 3.9. For an $\mathcal{O}(\mathcal{N})$ method of force evaluation, the computational cost of this simulation with the NEMD method would be at least 10^5 times greater, and therefore not tractable.

3.7 Simulation of double shock waves with a boundary condition

The simulation of a shock wave that leaves the material at a particular final particle velocity or pressure is of particular interest in making contact with experiments. Gun experiments and NEMD simulations usually apply a constant particle velocity boundary condition at the edge of the material.

When chemical reactions are present, the method for performing simulations to a given pressure or particle velocity depends on the sign of the volume change due to chemical reactions. If the chemical reactions result in an increase in volume, there are no shock instabilities and a single Rayleigh line solution is still valid. If the chemical reactions result in a decrease in volume, there may be an instability and a formation of a new shock. The strategy for performing these simulations involves doing *multiple* simulations with each one starting in the material pre-shocked state and each one of longer duration than the previous simulation. Each successive simulation employs a series of Rayleigh line constraints designed to take the system to the final boundary condition.

The bottom of Figure 3-4 shows a schematic of the evolution of a shock wave propagating in a system with a volume-reducing phase transformation. A fixed pressure is applied to the left side which launches a single shock wave. As the phase transformation occurs, a second shock wave forms which lowers the pressure of the first wave. The material in the first wave is in phase 1, and the second wave consists of material in phase 2.

The top of Figure 3-4 shows Hugoniots and Rayleigh lines for this hypothetical two phase system. In this case, the $p - v$ space path through which a small piece of material evolves is a function of how long the shock has been propagating. At any given point in the shocked material, we approximate this path as a series of Rayleigh lines where the single wave constraint Equation 3.8 applies in the volume region of applicability of each Rayleigh line.

Suppose a single shock is simulated to state B in phase 1 with a constant pressure post-shock boundary condition. However, phase 1 is metastable at this pressure and decays to phase 2 with some characteristic timescale. When this transition occurs, point B becomes an unstable point of Equation 3.8 and compression occurs. Since the transition initially occurs at the constant boundary condition pressure, point B also becomes a region of negative curvature along the Hugoniot which gives rise to a shock wave instability and splitting. Therefore a newly formed wave takes the system

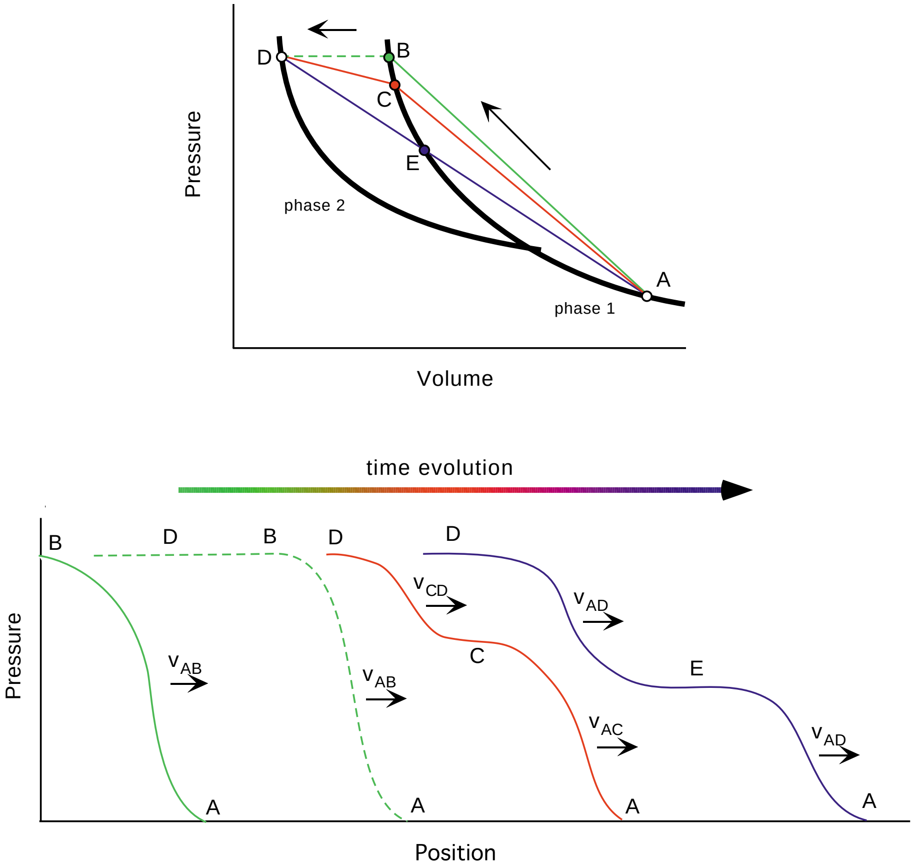

Figure 3-4: Example of shock wave evolution into two waves via a metastable state. Rayleigh lines are drawn on a hypothetical two-phase diagram above, and pressure profiles of the shock waves at instants in time are given below.

from B to D, the dotted green line. As time progresses, this chemical reaction drains energy from the first shock wave which lowers its shock speed (red lines). The change in shock speeds is simulated by starting a *new simulation* in state A subject to the constraints of the red Rayleigh lines. This is equivalent to simulation of a material element farther away from the constant pressure source which launches the shock.

The applicability of the approach outlined in this Chapter to shock wave simulation is only strictly rigorous in the case where steady waves exist. In the case discussed in this section, chemical reactions that have not reached completion can result in unsteady waves. Some assumptions are required to treat such waves using this approach. It is necessary to assume that chemical reactions behind the shock occur at successively slower rates. Since successive simulations model the shock effects on a material element further away from the surface where the shock is initiated, as in Figure 3-4, chemistry that occurs nearer the surface where the shock was initiated is ignored. This approximation can be justified if each successive simulation has a longer duration than the previous one, which means neglected chemistry occurring in material closer to the origin of the shock wave occurs in a smaller amount of material than the current simulation encompasses.

There is some ambiguity about when to begin a new simulation when a boundary condition has been deviated from in a given simulation, but when the boundary condition is met and the Rayleigh line validity condition Equation 3.10 holds, the simulation is valid.

3.7.1 Another silicon application: Transition to a metastable state

This section presents some preliminary results of simulations based on the ideas of the previous section regarding the simulation of shock waves to a given boundary condition. We focus here on crystalline silicon as an exemplary material where the accurate treatment of extreme atomic scale phenomena is difficult and requires the use of quantum mechanical approaches. Silicon has a complex phase diagram with many

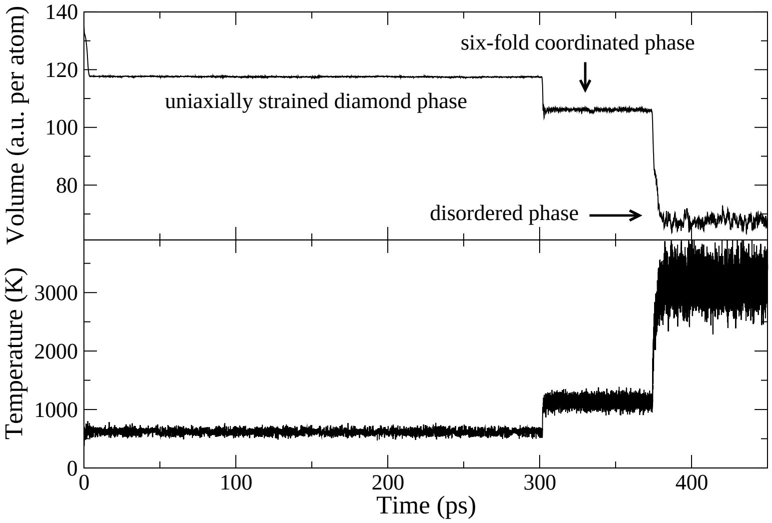

Figure 3-5: Volume and temperature of the shocked material as a function of time.

metastable structures, allowing for the possibility that the system can be shocked into a metastable state. Shock experiments that have been performed on the diamond phase of silicon indicate an orientational anisotropy in the shock wave structure.[23] Spontaneous shock wave splitting is observed in these experiments, although the underlying states of matter which give rise to these waves is not known.

The tight binding model for silicon of Sawada[57] was employed with the new method. A computational cell with 108 atoms was used to simulate shocks to a pressure of 32GPa in the [111] direction of the diamond phase. The calculations were performed with the system confined in the direction of shock compression between two "pistons" of silicon atoms fixed in the diamond structure with periodic boundary conditions in the direction transverse to the shock propagation direction. Some velocity dependent damping is applied to the equation of motion of atoms constrained in the pistons.

problems.

The volume and temperature as functions of time are depicted in Figure 3-5. The initial temperature is 600K and final pressure is 32 GPa. Figure 3-6 presents the $p-v$ paths for simulations at successively later times. The constraint Rayleigh lines are shown in red and the simulation trajectory for the last simulation is in black.

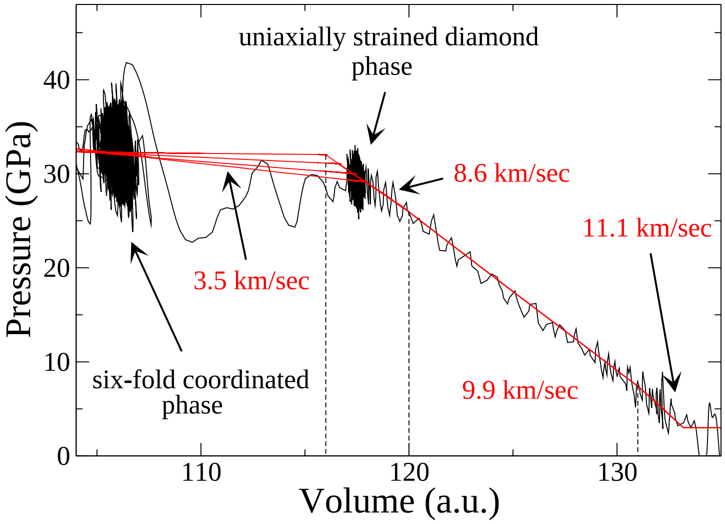

Figure 3-6: Pressure as a function of volume. The Rayleigh line associated with each shock wave is in red.

Using the method outlined above for determination of a region where a Rayleigh line is tangent to the Hugoniot, it was determined that three shock waves exist of speeds 11.1, 9.9, and 8.4 km/sec that result from regions of negative curvature in the Hugoniot for uniaxial compression of the diamond phase. In these waves, the system is compressed without plastic deformation as in Figure 3-1. These wave splittings are due to the presence of regions in the phase diagram of the diamond phase where $\frac{\partial^2 p}{\partial V^2}|_{Hugoniot} < 0$ for uniaxial compression in the [111] direction. It is possible that these waves are artifacts of the "piston" boundary conditions employed, but their presence does not have a significant effect on the metastable phase observed. Rather than simulate each of these shock waves separately, we have simulated the entire structure in each molecular dynamics run by increasing each shock wave speed by 0.1 km/sec so that there is little or no time spent in the states between waves.

The final shock wave consists of a martensitic phase transformation to a metastable 6-fold coordinated structure, followed by a transformation to a disordered phase for the remainder of the simulation. Before addressing the nature of this six-fold coordinated phase, we discuss the time-evolution of the third elastic wave due to the phase transformation.

Parameters and results of the molecular dynamics simulations and are given in

shock wave	speed	pressure	volume	lifetime τ
1	11.1	7.5	131	-
2	9.9	26.7	119.6	-
3	8.6	32	115.8	43
4	1	32.2	107	81
3	8.44	31	116.6	114
4	2.2	32.2	105	49
3	8.43	30	117	133
4	2.9	32.2	106	>239
3	8.42	29.1	117.9	297
4	3.45	32.1	106	72

Table 3.1: Pressure and volume regions of applicability for each of the four shock waves observed at successively later points in time. The first three waves are elastic and the fourth is the transformation to the six-fold coordinated phase. Speeds are km/sec, volumes are atomic units per atom, pressures are in GPa, and times are picoseconds.

Table 3.7.1. Since this transformation appears to be of a martensitic type, the applicability of Equation 3.9 is suspect because it is based on continuum theory which assumes that the reaction is described by a continuous reaction parameter, or there is at least a mixed phase region in the case of a martensitic transformation. Therefore, it is difficult to make a definitive statement about the validity of the Rayleigh line parameterization in this martensitic case. Use of a larger simulation cell may alleviate this problem by giving rise to a mixed phase region which will make Equation 3.9 more applicable.

This simulation is of the evolution of the shocked system on the 100 picosecond timescale, which is two orders of magnitude longer than would be possible with the non-equilibrium molecular dynamics simulation of the entire shock wave structure. The computational work required for the order N^3 method of force evaluation for this tight binding model to do this simulation with non-equilibrium molecular dynamics shock wave approach is about 10^8 times greater. This is another illustration of the tremendous power of this new method.

The 6-fold coordinated structure formed in the final wave is shown in Figure 3-7 looking down the [110] axis. This phase has bonding structure similar to the diamond

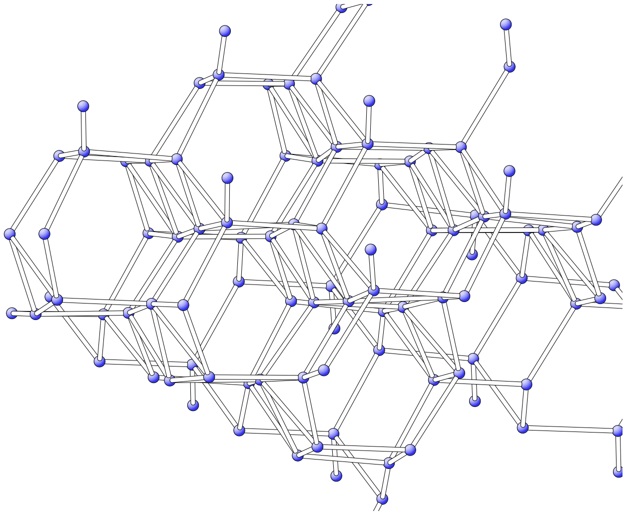

Figure 3-7: Molecular dynamics snapshot of the metastable six-fold coordinated phase viewed down the [110] direction. Bonds down the [110] direction distinguish this phase from the diamond structure. Some of these bonds are missing, resulting in five-fold coordinated atoms.

phase but possesses additional bonds connecting all atoms down the [110] axis, although some of these bonds are missing, resulting in five-fold coordinated sites. These missing bonds are presumably associated with crystal defects.

The six-fold coordinated phase was also observed to form in a larger computational cell with 216 atoms under a constant uniaxial stress of 35 GPa. The phase transformation was initiated away from the "piston" boundaries fixed in the diamond phase, which suggests it is not likely an artifact of that particular type of boundary condition. Further evidence was seen in non-equilibrium shock molecular dynamics simulations of shocks in the [111] direction with piston velocities from 1.7 kmps to 2.0 kmps. These simulations only lasted 1 picosecond, but the six-fold coordinated phase is observed near the piston which launches the shock. Non-equilibrium shock molecular dynamics simulations with a small shear velocity of 0.2 km/sec in the $[1\bar{1}0]$ direction produced more volume of the six-fold coordinated phase before the end of the simulation. This shear direction brings atoms along the [110] direction closer to each other. A small amount of the same shear strain occurred during the martensitic phase transformation in the simulation using the new method. Such shear strain is not considered in Equation 3.8 and may be present the shock wave propagating in a direction other than the [111] direction. The further interpretation of the formation of this metastable state may require closer consideration of this issue.

The metastability of the six-fold coordinated phase for short times in the simulations non-hydrostatic stress conditions does not necessarily imply it is also metastable under hydrostatic stress. Density functional theory calculations on the six-fold coordinated phase indicate that it is probably very short lived or unstable under hydrostatic stress, although it is metastable under small amounts (1-2 GPa) of shear stress. [56] This phase has a very soft phonon mode which can relax the system to the simple hexagonal phase or the *Imma* space group phase[46] under hydrostatic conditions. The non-hydrostatic unit cell is body-centered orthorhombic with the same basis atoms as the experimentally identified *Imma* structure, but the shortest lattice vector for the experimentally observed *Imma* phase is the longest for the phase observed here, which suggests a different bonding structure.

The six-fold coordinated phase observed here seems to have a lifetime on the order of 100 picoseconds, which might make it difficult to detect experimentally. Another issue in the observation of this short lived phase is the role of plastic deformation. None was observed in the simulations until the formation of the six-fold coordinated phase. Over longer time scales, plastic deformation is expected to occur at lower pressures which might preclude this high pressure martensitic transformation directly from the diamond phase. Experiments done on longer time scales suggest the Hugoniot elastic limit for silicon is in the 5-10 GPa range. In addition to the relatively short time scale simulations performed here, the finite size of the computational cell may enhance the resistance of the material to plastic deformation. Nevertheless, there is some experimental evidence for the lack of plastic deformation on nanosecond time scales in the work of Loveridge-Smith, *et al.*[40] xray diffraction was performed on diamond phase silicon shocked in the [001] direction to uniaxial strains of up to 11%. No plastic deformation was observed during the several nanosecond observation time.

Chapter 4

The color of shock waves in photonic crystals: Adiabatic effects in shocked photonic crystals

Unexpected and stunning new physical phenomena result when light interacts with a shock wave or shock-like dielectric modulation propagating through a photonic crystal. These new phenomena include the capture of light at the shock wave front and re-emission at a tunable pulse rate and carrier frequency across the bandgap, and bandwidth narrowing as opposed to the ubiquitous bandwidth broadening; these phenomena occur while maintaining quantum coherence. These effects do not occur in any other physical system, and are all realizable under experimentally accessible conditions. Furthermore, their generality make them amenable to observation in a variety of time-dependent photonic crystal systems, which has significant technological implications.

4.1 Introduction

Photonic crystals[73, 31, 30] are a promising and versatile way to control the propagation of electromagnetic radiation. Nevertheless, very little attention has been given to the effects of non-stationary photonic crystals on electromagnetic radiation propagation. It has been shown that the frequency of light can be changed across a bandgap in a photonic crystal which is physically oscillating.[60, 61] However, the frequency of oscillation is required to be of the order of the bandgap frequency in the photonic crystal. Such oscillation frequencies are impossible for light of $1\mu m$ wavelength.

In this paper, we consider the influence of a propagating shock-like modulation of the dielectric in a photonic crystal on the electromagnetic radiation inside. This scenario can cause light to be trapped at the shock front and transferred in frequency from the bottom of a bandgap to the top or vice-versa. The frequency conversion can be accomplished in an adiabatic fashion arbitrarily slowly and therefore does not require the movement of material at speeds near that of light. We will also demonstrate anomalous Doppler shift effects involving reverse single frequency shifts and/or multiple frequency generation. Furthermore, we present techniques which allow the bandwidth of a pulse of light to be increased or decreased by orders of magnitude. These last three effects arise when light reflects from the moving shock-like modulation of the dielectric.

There is no non-quantum mechanical way, that we are are of, to significantly narrow the bandwidth of a wavepacket, and changing the frequency of light an arbitrary amount with high efficiency is a challenging problem. Acousto-optical modulators can change the frequency by a part in 10^{-4}, but larger changes in frequency are desirable for most applications. Non-linear materials can be used to produce large changes in light frequencies through multi-photon combination. However, high intensities are required and the frequencies produced are still limited by the range of input frequencies and phase-matching constraints. Production of an arbitrary frequency shift in a given system is not possible.

Of additional interest in optical applications is the ability to trap and manipulate pulses of light. Few technologies exist to trap 100% of the energy of a pulse of light for a period of time which is determined while the light is trapped. Existing approaches for stopping light for a period of time require the presence of materials which are orders of magnitude colder than room temperature.[38, 53] We describe here a new physical phenomenon associated with a shock-like modulation of the photonic crystal dielectric that enables light to be trapped for a controlled period of time.

4.2 Computational Experiments

In this section we present an overview and brief discussion of our results from computation experiments. A thorough analysis and explanation of these results will be given in the following sections.

To explore the phenomena associated with light scattering from a shock-like wave in a photonic crystal, we perform finite difference time domain (FDTD)[63] simulations of Maxwell's Equations in one dimension, single polarization, and normal incidence for a system described by a time-dependent dielectric $\epsilon(x, t)$.

A typical shock-like profile considered in this work is depicted in Figure 4-1. It corresponds to the dielectric function given by,

$$\epsilon(\hat{x} = \frac{x}{a}, \hat{t} = \frac{ct}{a}) = 6 + 7 \sin\left[\pi\left(3\hat{x} - \frac{v}{c}\hat{t}\right) - \frac{\pi}{\gamma}\log\left(2\cosh\left(\gamma\left(\hat{x} - \frac{v}{c}\hat{t}\right)\right)\right)\right], \quad (4.1)$$

where v is the shock speed, and a is the period of the pre-shocked crystal. The photonic crystals on both sides of the shock front have periodic variations of ϵ ranging from 1 to 13. The thickness of the shock wave front is given by γ^{-1}, which we take to be 0.05. Figure 4-1 describes this shock wave propagating to the right, leaving a compressed lattice behind. The shocked lattice is identical to the original but with a smaller lattice constant. In this case, the shock wave compresses the lattice by a factor of two. This choice of large compression is for illustrative purposes only. The observed phenomena are reproducable using scenarios with considerably less compression, to be discussed later. The interface moves at the shock speed v and the material behind also moves uniformly at a slower speed known as the particle speed. The particle speed is $\frac{v}{2}$ in this case.

The bandgaps for the crystals which exist in front of and behind the shock front are depicted in Figure 4-2. Note there is an overlapping bandgap which extends over

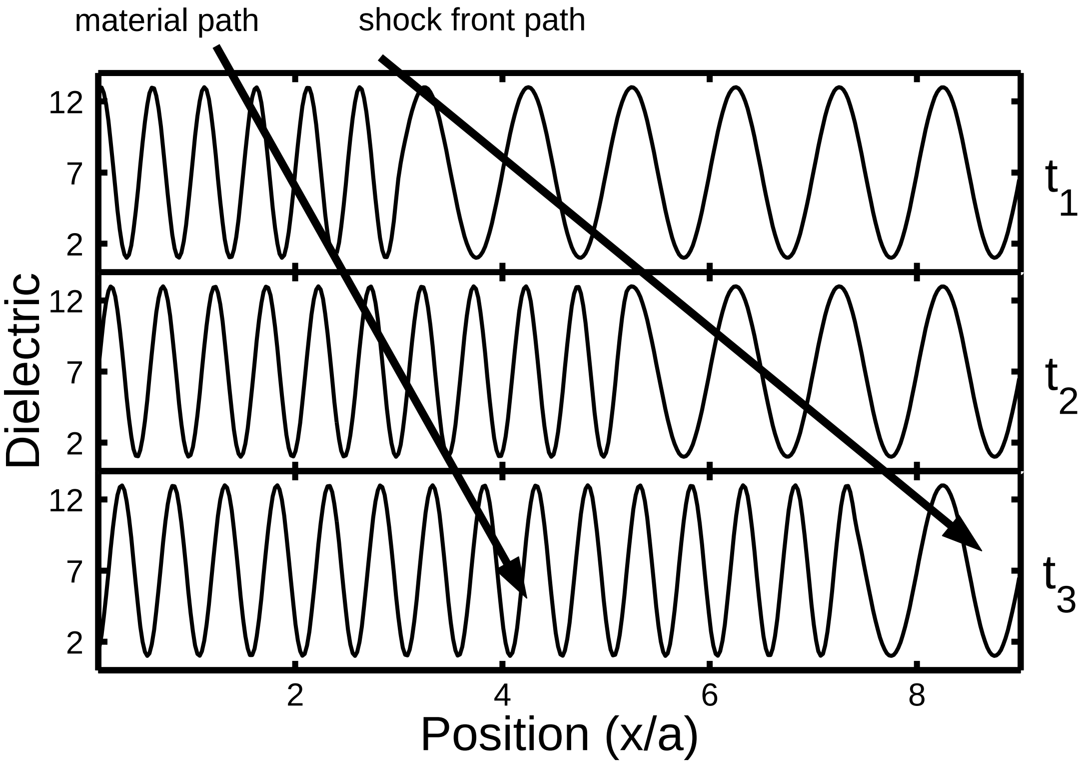

Figure 4-1: The dielectric described by Equation 4.1 as a function of position for three equally-spaced instants in time, $t_1 < t_2 < t_3$. Arrows follow the shock front and material paths which move at different speeds.

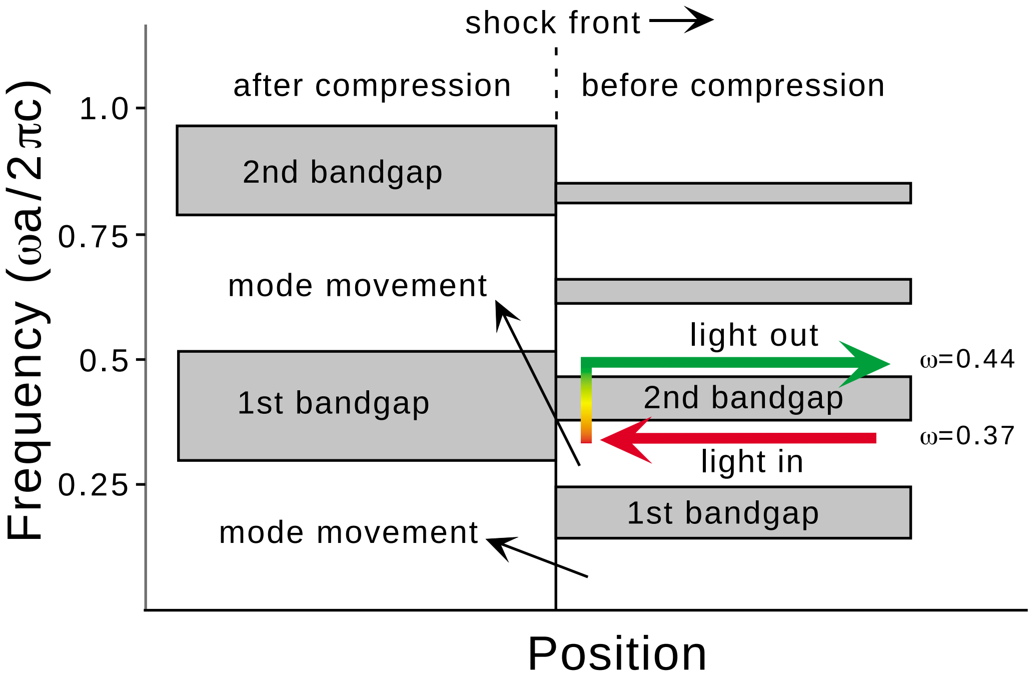

Figure 4-2: Schematic of a shock wave moving to the right which compresses the lattice by a factor of two. Light incident from the right (red arrow) will be converted up in frequency at the shock front and escape to the right. The black arrows indicate the adiabatic evolution of the modes for the lowest two bands.

the entire crystal formed by the second bandgap on the right and the first bandgap on the left.

Consider now electromagnetic radiation incident from the right (opposite to the direction of shock propagation) with frequency just below the second bandgap as shown in Figure 4-2. Under certain conditions, we find that some of this radiation is converted up in frequency to the top of the bandgap where it propagates away from the shock. For example, Figure 4-3 shows the magnetic field for a simulation where the shock front (dashed line) propagates to the right with $v = 3.4 \times 10^{-4}c$. The panels in Figure 4-3 are obtained by Fourier transforming the magnetic field over windows of time ($\Delta t = 200a/c$) centered at the times shown in the upper right corners. Light is initially spatially contained in a Gaussian distribution centered around $x/a = 40$ at the band edge frequency. As the Gaussian distribution moves and broadens to the left, most of the incident light is trapped in a localized state at the shock front in the overlapping bandgap frequency region of the two photonic crystals. While it is trapped, it evolves up in frequency through the pre-shocked bandgap and is released to the right of the shock with about 20% change in frequency in this case. The amount of frequency shift in this example can be tuned by adjusting the size of the bandgap of the pre-shocked crystal. The shock wave propagates about $0.5a$ in Figure 4-3, and this frequency conversion process is observed once for every lattice unit the shock wave traverses, resulting in a pulsed output for a continuous wave input. The pulse rate can be controlled with the shock speed. Qualitatively similar effects were observed for a slower shock velocity of $v = 3.4 \times 10^{-5}c$.

An additional consequence of this scenario is the localization of light for a controlled period of time. If the speed at which the shock-like interface moves can be controlled, then the light can be confined in the gap region for a time that is determined by that shock speed. Note that the propagation speed of light is near zero while trapped at the shock front, which may have useful applications in telecommunications or quantum optics.

Figure 4-4 contains results of a simulation similar to that in Figure 4-3, but with a faster moving shock front of $v = 3.4 \times 10^{-3}c$. Light in this simulation starts out as a Gaussian centered at $x/a = 220$ with the bandgap edge carrier frequency. The Fourier transform of magnetic field which produced this Figure utilized a longer time period ($\Delta t = 6000a/c$) than those of Figure 4-3 and shows the entire upconversion of light from below the gap to the top of the gap as the shock front passes through several lattice periods. The light trapped at the shock front appears to exist in discrete frequencies and escapes at the top of the gap in discrete frequencies. This discretization can be loosely interpreted as a result of repeated bounces of the light between the moving material on the left and the fixed material on the right, and is commensurate with the periodic nature of the pulsed output. The interpretation of the output light in Figures 4-3 and 4-4 as equally-spaced discrete frequencies or pulses is a matter of frequency resolution in the detection apparatus.

The frequency of the localized state at the shock front observed in Figure 4-3 is well defined in the limit of a slowly propagating shock where $\frac{d\omega}{dt} \ll \omega^2$. However,

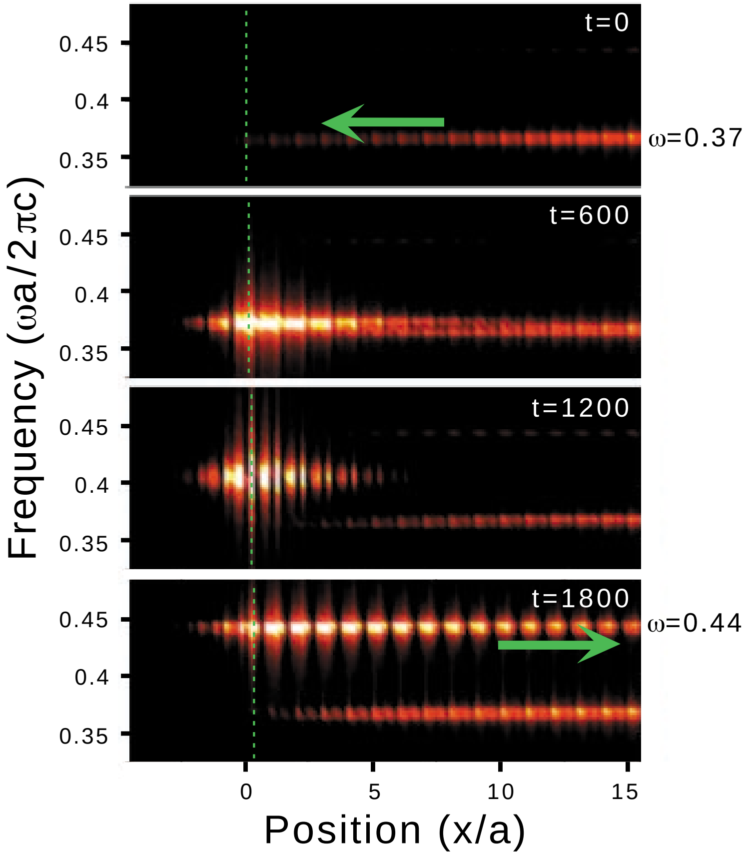

Figure 4-3: Depicted are four moments in time during a computer simulation of the shock in Figure 4-1 moving to the right with $v = 3.4 \times 10^{-4}c$. Time is given in units of a/c. The shock front location is indicated by the dotted green line. The light begins the simulation below the gap in the unshocked material at $\omega = 0.37$ as in Figure 4-2. As the light propagates to the left, most of it is trapped at the shock front until it escapes to the right at $\omega = 0.44$.

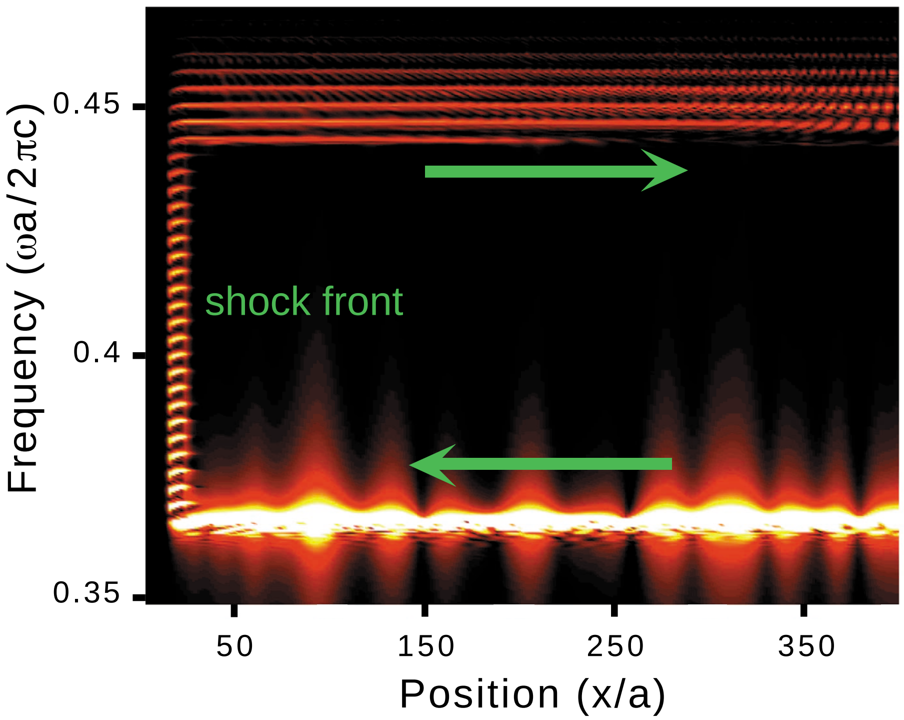

Figure 4-4: Depicted is a computer simulation of the shock in Figure 4-1 moving to the right with $v = 3.4 \times 10^{-3}c$. Light at $\omega = 0.37$ below the bandgap is converted up in frequency at the shock front and propagates away as discrete frequencies around $\omega = 0.45$. The frequencies are separated by $2\pi v/a$.

for shock speeds sufficiently fast for this condition to break down, the localized mode possesses an effective bandwidth which is on the order of the bandgap frequency width. Figure 4-4 is approaching this regime, where it is almost more appropriate to think of the light continuously moving up through the bandgap rather than in a pulsed fashion as in Figure 4-3.

The shock-like dielectric modulation of Figure 4-1 can also be used to *narrow* the bandwidth of a pulse of light. This is accomplished by confining the light between the moving shock front on the left and a reflecting surface of the right. Figure 4-5 contains results of such a simulation where the bandwidth of input light is reduced by a factor of 4. The shock is moving with $v = 10^{-4}c$ and $\gamma^{-1} = 2$. The narrowing process can become more effective for slower shock velocities, larger simulation cells, and narrower initial bandwidths.

4.3 Analysis

4.3.1 Simple adiabatic theory

The phenomena observed in Figures 4-3 and 4-4 can be largely understood by considering the time-evolution of the various allowed modes as the shock propagates. Each time the shock wave propagates through one lattice unit, the crystal on the right in Figure 4-2 is reduced in length by one lattice unit and the crystal on the left is increased by one lattice unit. Since the number of allowed values of k in a band is equal to the number of lattice periods in the crystal (ignoring polarization degeneracy,) each time the shock wave passes over one lattice unit, the number of states in each band in the pre-shocked crystal must decrease by one and increase by one in the post-shocked crystal. This transfer process is indicated by the mode movement arrows in Figure 4-2 for the lowest two bands. Note that to accomplish this in the case of the second band, it is necessary for a mode to move up through the overlapping gap formed by the 2nd bandgap in the preshocked region and the 1st bandgap in the postshocked region.

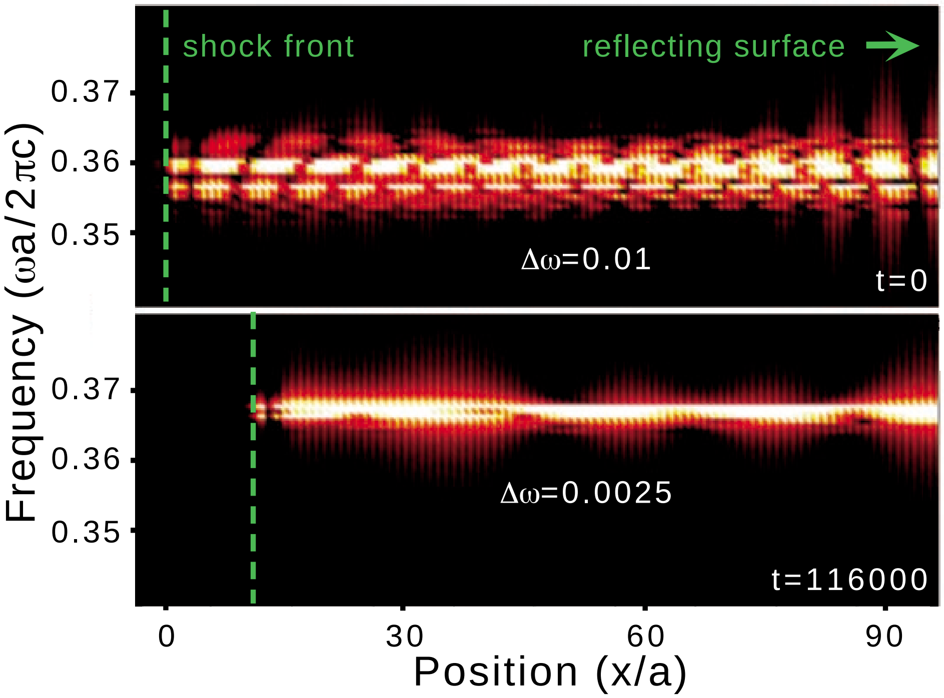

Figure 4-5: Depicted are two moments in time during computer simulation of the shock in Figure 4-1. The shock front is indicated by the dotted green line, and time is given in units of a/c. Light is confined between the reflecting shock front on the left and a fixed reflecting surface on the right. As the shock moves to the right with $v = 10^{-4}c$, the bandwidth of the confined light is decreased by a factor of 4.

Indeed, the large frequency changes in Figures 4-3 and 4-4 are a direct result of the adiabatic evolution of the light through this overlapping bandgap. The light is essentially trapped in a cavity which is “squeezed” as the shock compresses the lattice, thereby increasing the frequency. This occurs once each time the shock propagates through a lattice unit.

While a significant change in the frequency of electromagnetic radiation through mechanical means usually requires the interaction with objects that are moving at a significant fraction of the speed of light, the adiabatic approach does not have this requirement. The adiabatic nature of the evolution of the radiation up in frequency through the total system bandgap has the property that it can be done arbitrarily slowly with the same large shifts in frequency. This key physical mechanism liberates the shocked photonic crystal from the impossible task of interface propagation near the speed of light. Finally, we note that a time-reversed, frequency lowering effect also occurs in this adiabatic picture.

4.3.2 Non-adiabatic theory

The adiabatic picture is valid as long as the scattering processes involved with the incident light reflecting from the shock wave do not introduce frequency components that are significantly outside the original input pulse bandwidth. Therefore, the more time the incident light spends interacting with the shock front, the more likely it is for this condition to hold.

To develop a non-adiabatic theory, we focus on a scenario where the incident light is at a frequency that falls within the gap of the *compressed* crystal. Far away from the shock front, the electric field in the pre-shocked photonic crystal is given by,

$$E\left(x,t\right) = E_0 e^{ikx} w_{k,n}(x) e^{-i\omega t}, \tag{4.2}$$

where k and n denote the translational and band indicies, and $w_{k,n}\left(x\right)$ has the periodicity of the lattice, $w_{k,n}\left(x+a\right) = w_{k,n}\left(x\right)$.

Since the frequency of the incident light lies within the bandgap of the compressed photonic crystal, an effective model of the shock front is a mirror with a space-dependent dependent E field reflection coefficient, $R(x)$, where x is the mirror position. R has the property that $|R(x)| = 1$ since the incident light reflects from the bandgap of the post-shocked crystal. In general R has some frequency dependence but we will consider the bandwidth of the incident light sufficiently small to neglect it. If the shock front is stationary, the boundary condition in terms of incident and reflected light is,

$$E_1 e^{ik_1 x} w_{k_1,n}(x) e^{-i\omega_1 t} = E_0 R(x) e^{ik_0 x} w_{k_0,n}(x) e^{-i\omega_0 t}, \tag{4.3}$$

where k_0 and k_1 correspond to the incident and reflected states respectively, and E_0 and E_1 are constants.

For light near the band edge at $k = 0$, the frequency has the form $\omega = \omega_0 + \alpha k^2$. This substitution can be made without loss of generality because the condition near any band edge can be obtained by considering $k \rightarrow k - k_{edge}$ and a redefinition of the function $w_{k,n}(x)$. If we assume that the shock is moving sufficiently slowly that the reflected light has the form of a single Bloch state, we can make the substitution $x \rightarrow x_0 - vt$ to obtain a relation for the boundary condition at the shock front. This gives,

$$\frac{E_1(t)}{E_0} = e^{i(\alpha k_1^2 - \alpha k_0^2)t} e^{-i(k_1 - k_0)(x_0 - vt)} R(x_0 - vt) \left[\frac{w_{k_0,n}(x_0 - vt)}{w_{k_1,n}(x_0 - vt)} \right], \tag{4.4}$$

where $E_1(t)$ now has some amplitude time-dependence due to the term in brackets.

It can be shown that near a band edge where k is small,

$$w_{k,n}(x) \approx iku_n(x) + \frac{d}{dx} u_n(x), \tag{4.5}$$

where $u_n(x)$ has the periodicity of the lattice and is independent of k. We can simplify

Equation 4.4 by noting that when $k_1 u_{k_1,n}(x_0 - vt) \ll \frac{d}{dx} u_{k_1,n}(x_0 - vt)$ and likewise for k_0, the term in brackets in Equation 4.4 is unity, and $E_1(t)$ is time-independent. Since we consider small k near the Brillouin zone center, this should be the case most of the time. If we now also take $R(x) = -1$ as for a metallic mirror, the time-dependence of Equation 4.4 must satisfy,

$$\alpha k_1^2 - \alpha k_0^2 + (k_1 - k_0)v = 0. \tag{4.6}$$

This gives a frequency shift of,

$$\omega_1 - \omega_0 = \frac{v^2}{\alpha} + 2vk_0 = \frac{v(v + v_{g,0})}{\alpha}. \tag{4.7}$$

The last relation is given in terms of the group velocity defined by $v_g = \frac{d\omega}{dk} = 2\alpha k$. The relation between incident and reflected group velocities can be expressed as $v_{g,1} = -2v - v_{g,0}$. If $v < 0$ and $v_{g,0} < 0$, the mirror is moving to the right and incident light propagates to the left.

There are two remarkable features of Equation 4.7. The first is that in the slow velocity limit where $|2vk_0| \gg |\frac{v^2}{\alpha}|$, the Doppler shift $2vk_0$ is much smaller in magnitude than the usual vacuum Doppler shift $2v(k_0 - 2\pi/a)$ because $k_0 \ll 2\pi/a$ near the Brillouin zone center. The second notable feature is that for $v < 0$, above the bandgap where $\alpha > 0$ the Doppler shift is positive, whereas below the bandgap where $\alpha < 0$ the Doppler shift is negative. Therefore incident light is Doppler shifted away from the bandgap region on both sides of the bandgap.

It is interesting to note that the term in brackets in Equation 4.4 changes phase slowly except when $\frac{d}{dx} u_n(x_0 - vt) \approx k u_n(x_0 - vt)$, when the phase can change very rapidly. This indicates that the reflected frequencies are very sensitive to the position of the reflector in these special regions for light where $|k| \ll 2\pi/a$. This property could be useful in resolving the motion of objects which have oscillation amplitudes much smaller than the wavelength of the light they are reflecting, or for mechanical modulation of optical signals.

4.3.3 Connection between non-adiabatic and adiabatic theory

Consider the non-adiabatic model associated with the scenario of Figure 4-1. We will now show that in the limit $v \rightarrow 0$, the non-adiabatic model reduces to the adiabatic limit and provides some new physical insight. As we previously discussed, the adiabatic limit is achievable by increasing the time the incident light spends interacting with the shock front. Therefore, we take the adiabatic limit by considering the effect of repeated bounces of the light from the slowly moving reflector where each bounce is described by Equation 4.4. We assume that the light bounces between the slowly moving reflector and a fixed reflector positioned a distance $L \gg a$ away in the crystal. Let $R(x) \equiv e^{i\theta(x)}$, and let the term in brackets in Equation 4.4 be denoted by $e^{iP(x_0 - vt)}$. Assigning unit magnitude for the term in brackets in Equation 4.4 is acceptable for all time in the limit of small v where $k_1 \rightarrow -k_0$. Then the time dependence of Equation 4.4 requires,

$$\alpha k_1^2 + k_1 v = \alpha k_0^2 + k_0 v + \theta'(x_0 - vt_0)v + P'(x_0 - vt_0)v, \tag{4.8}$$

where θ and P have been linearized about t_0, which is valid in the limit $v \rightarrow 0$. Primes denote derivatives. Then after p bounces of the light between the stationary and moving reflectors,

$$\alpha k_p^2 + k_p v = \alpha k_0^2 + k_0 v - \sum_{j=1}^{p-1} 2k_j v + \sum_{j=0}^{p-1} \left(\theta'(x_0 - vt_j)v + P'(x_0 - vt_j)v\right). \tag{4.9}$$

The number of bounces of the light p that occur during a time a/v when the reflector moves through one lattice constant is, $p = \frac{av_g}{2Lv}$. The variation of v_g over this time can be neglected in the limit $L \gg a$.

Taking the limits $v \to 0$ ($p \to \infty$) and $L \ll a$ give,

$$\alpha k_\infty^2 = \alpha k_0^2 + \frac{v_g}{2L} \int_0^a \left(\theta'\left(x_0 + x\right) + P'\left(x_0 + x\right)\right) dx.$$

The periodicity of the crystal gives the property that $\theta(x+a) - \theta(x) = 2\pi\ell$ and the periodicity of $w_{k,n}$ gives the property that $P(x+a) - P(x) = 2\pi m$, where ℓ and m are integers. This substitution and some simplification gives the final result for the adiabatic change in k during the propagation of the shock over one lattice constant,

$$\Delta k = \frac{\pi(\ell + m)}{L}. \tag{4.10}$$

The integer m is related to the particular bandgap around which $w_{k,n}$ describes states. It can be shown that for a sinusoidal dielectric, $m = -1$ above and below the first bandgap, $m = -2$ above and below the second bandgap, and so on. The integer ℓ is also related to the particular bandgap from which light is reflecting. For a sinusoidal dielectric, $\ell = 1$ for the first bandgap, $\ell = 2$ for the second, and so on for the higher bandgaps. While quantum numbers are preserved in an adiabatic evolution, the k values we refer to here change during an adiabatic evolution because they are convenient labels, not quantum numbers.

When Equation 4.10 is applied to the scenario in Figure 4-2, $\ell + m = 1 - 2 = -1$ which indicates that the k quantum number of light will adiabatically decrease one k quantum for each lattice constant the shock wave moves. This is consistent with the adiabatic picture presented above which shows that one mode of the system must move up through the total system gap per lattice unit the shock traverses in Figure 4-2. Furthermore, the invariance of the adiabatic picture to the details of crystal structure provides a general proof that the above statements about m and ℓ hold for all crystals.

Another interesting case is when the shock interface separates two crystals of differing bandgap sizes such that light near the first bandgap in the pre-shocked crystal reflects from the first bandgap of the post-shocked crystal. In this case, $\ell + m = 1 - 1 = 0$ indicating there is no net Doppler shift for small shock velocities. This absence has been observed in FDTD simulations.

While there are numerous ways to increase the bandwidth of a wave packet, there are, to our knowledge, currently no non-quantum mechanical ways to decrease the bandwidth. An important implication of this adiabatic evolution of light is that the bandwidth of a pulse of light can be modified in a controlled fashion while bouncing between the moving shock wave and a fixed reflecting surface as in Figure 4-5. Equation 4.10 indicates the width of a wavepacket in crystal momentum space δk should be preserved after many bounces because every k state moves by the same amount. The dispersion relation near a band edge indicates the bandwidth $\delta\omega$ for a wavepacket of width δk is a function of k near the band edge, $\delta\omega = 2\alpha k \delta k$. Therefore the bandwidth of a pulse will be altered as it evolves through k-space during the bouncing. This fact enables the compression of the bandwidth of a pulse of light to a vanishing amount in the limits of a large separation between the two reflecting surfaces and slowly moving shock front.

In Figure 4-5, a wavepacket of mean wavevector k is shifted up in frequency toward the band edge, causing the bandwidth to decrease. The bandwidth is modified without a very large change in average frequency. However, if the wavepacket reaches the band edge, it will be trapped at the shock front and converted up in frequency until it is expelled at the frequency of the top of the bandgap. In this case, there is a large average frequency shift in addition to a narrowing in bandwidth. Both of these effects may have useful applications.

4.4 Practical considerations

The new physical phenomena presented in this work are quite general and also observable in 2D and 3D systems. The generalized shock-like profiles of the dielectric of the type discussed in the previous sections may be generated by a variety of means. It is possible to launch a physical shock wave into the photonic crystal. Materials are routinely shocked to GPa and higher pressures using lasers and gun facilities and optical techniques involving the reflection of light from a moving shock front are used as diagnostics in shock experiments.[24, 4] A photonic crystal with any type of structure may be used to observe the predicted effects, including a multilayer film. While we have considered large compressions for illustrative purposes, the same phenomena are readily observable with compressions of a few percent or less through the use of deliberately designed defect bands or overlapping bandgaps formed by higher frequency bandgaps in the pre and post-shocked crystals. Typical shock speeds of 10^4 m/sec and a readily achievable Q for the trapped mode of 10^3 are sufficient to observe all the effects described in this work. For example, a photonic crystal consisting of a silicon/silicon-dioxide multilayer film can be fabricated and shocked to a strain of a few percent without significantly increasing the material absorption or changing the dielectric response. If light is shined into this shocked crystal with frequency components within roughly $10^{-3}\omega_{\text{edge}}$ of the lower edge of a higher bandgap ω_{edge} (e.g., the 30th bandgap, depending on the amount of strain), reflected light with a frequency shift on the order of 1% will be observed. The pulse rate will be around 10GHz for light of wavelength $1\mu m$. The bandwidth narrowing scheme as presented in Figure 4-5 can also be realized with this system by making the photonic crystal 100 lattice units in length and shining the light into the side of the system at a shallow angle so that it bounces between the shock front and other reflecting mirror surface about 1000 times and then exits the system from the other side. For this scenario, a bandwidth narrowing on the order of a factor of 10 is expected for input light, of frequency ω, further from the bandgap edge and bandwidth $10^{-3}\omega$.

Alternatively, materials which undergo a change in the dielectric constant under an applied electric field or applied change in temperature can be modulated in a time-dependent shock-like fashion. Such an approach might make possible the control of the shock velocity and shock front thickness through time-dependent control of the local dielectric at all points in the system. Time-dependent changes in the dielectric can also be generated using materials with a non-linear optical response. Finally, MEMS devices provide an avenue for the generation of time-dependent effects in photonic crystals. For example, the adiabatic transfer of light between the bottom and top of a bandgap may be accomplished by varying the air spacing between two photonic crystals of differing lattice constants in an oscillatory fashion. As another example, consider a rotating disk containing a spiral photonic crystal pattern. Small millimeter diameter MEMS disks have been made to rotate at millions of RPM in microengines.[39] Light reflecting from the edge of such a disk will see a dielectric modulation identical to that of Figure 5-5 as viewed in a reference frame where the shock front is stationary. This Figure will be discussed in the next Chatper. All of the phenomena presented in this work may be realized using variations on this approach.

Chapter 5

Anomalous Doppler effects in photonic crystals: Non-adiabatic effects in shocked photonic crystals

Reversed Doppler shifts have never been observed in nature and have only been speculated to occur in pathological systems with simultaneously negative effective permittivity and permeability.[70, 3] This work presents a different, new physical phenomenon that leads to a reversed Doppler shift in light. It arises when light is reflected from a moving shock wave propagating through a photonic crystal. In addition to reflection of a single frequency, multiple discrete reflected frequencies or a 10 GHz periodic modulation can also be observed when a single carrier frequency of wavelength 1 μm is incident.

5.1 Introduction

In 1843, Johann Christian Doppler proposed an effect whereby the frequency of waves emitted from a moving object is shifted from the source frequency. The Doppler shift phenomenon has since realized applications ranging from weather and aircraft radar systems to satellite GPS to the measurement of blood flow in unborn fetal vessels to the detection of extrasolar planets. The Doppler effect predicts that light shined by an observer onto an object moving toward him will be reflected with a higher frequency. In this Letter, we show that the established theory behind the Doppler shift breaks down for light reflected from a shock wave propagating in a photonic crystal,[73, 31, 30] or material with a periodic modulation of the dielectric. We employ detailed numerical simulations and analytical theory to prove that anomalous Doppler shifts, both in sign and magnitude, can be observed. These effects are realizable under readily experimentally-accessible conditions.

5.2 Computational experiments

To explore the phenomena associated with light scattering from a shock wave in a photonic crystal, we perform finite difference time domain (FDTD)[63] simulations of Maxwell's Equations in one dimension, single polarization, and normal incidence for a system described by a time-dependent dielectric $\epsilon(x,t)$. These simulations solve Maxwell's equations with no approximations except for the discretization, and are known to excellently reproduce experiments.

The effects of a shock wave propagating in a 1D photonic crystal are shown in Figure 5-1. The pre-shocked crystal (on the right) is comprised of two materials with identical bulk moduli (and therefore identical sound speeds) but differing dielectric. One layer has length $d_1 = 0.2a$ and the other has length $d_1 = 0.8a$, where a is the pre-shock lattice constant. The compression of the lattice by the shock wave has two key effects on the photonic crystal: the lattice is compressed and the dielectric is changed through a strain dependence. If we focus on materials where the dielectric constant is increased with compression, these two main effects affect the bandgap frequency in opposing ways in the shock-compressed material: decrease of the lattice constant increases the bandgap frequency, but increasing the dielectric lowers the bandgap frequency. The bandgap can be made to decrease in frequency upon compression if materials with a sufficiently large dielectric dependence on strain are employed, $\frac{d\epsilon}{ds}$, where material strain is given by s. Materials that are used for acousto-optical modulation in particular can have a large negative dielectric dependence on strain.[13]

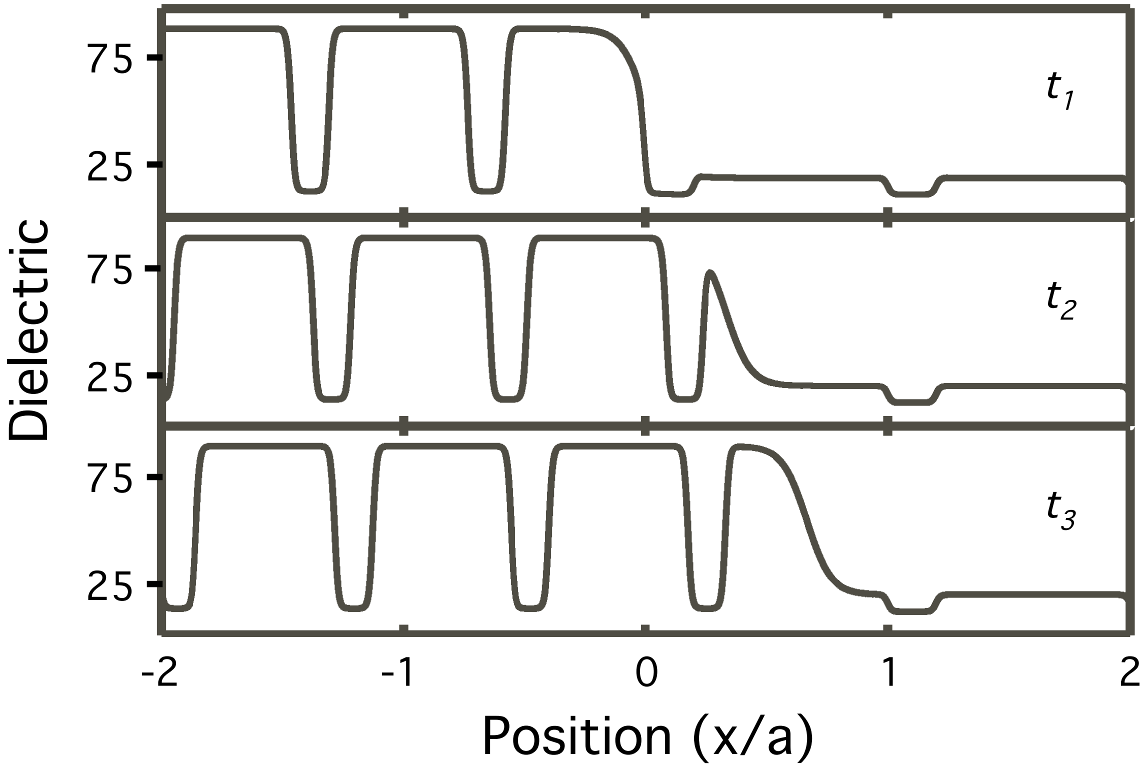

Figure 5-1: Dielectric as a function of position for three equally-spaced instants in time, $t_1 < t_2 < t_3$. The shock front moves at a constant velocity, and the material behind the shock moves at a smaller constant velocity. For this model, the dielectric ranges from 2.1 to 11.0 before the shock front and 3.7 to 89.4 behind the shock front. These large values are for computational tractability only. All the results of this work can be observed with physical values as discussed in the text.

As an illustrative example, we have chosen parameters for our model system with $\frac{1}{\epsilon_1}\frac{d\epsilon_1}{ds_1} = -2.9$ and $\frac{1}{\epsilon_2}\frac{d\epsilon_2}{ds_2} = -26.5$, a bulk modulus for both materials of 37 GPa, and a shock pressure of 10 GPa. The strain dependence of the dielectric is exaggerated purely due to the computational requirement of very long simulations and fine spatial discretization for realistic parameters. All effects proposed in this Chapter can be observed in experimentally accessible scenarios. For example, a photonic crystal with a bandgap width of $10^{-2}\omega_{gap}$ made mostly of tellurium shocked to a strain of around 1% will produce frequency shifts of $3 \times 10^{-7}\omega$ which are readily observable experimentally. Experimental details will be discussed later.

The time-dependent 1D dielectric shown in Figure 5-1 is composed of bilayer regions where the location of the interfaces between bilayers in the shocked crystal $\left(x_{1,j}(\hat{t}), x_{2,j}(\hat{t})\right)$ (in units of the pre-shocked lattice constant a) are given in terms of the locations of the interfaces between bilayer regions in the unshocked crystal $(\tilde{x}_{1,j}, \tilde{x}_{2,j})$ as,

$$x_{i,j}(\hat{t}) = \tilde{x}_{i,j} - \frac{p}{2B}\left(\tilde{x}_{i,j} - v\hat{t}\right)\left(\tanh\left(-\gamma\left(\tilde{x}_{i,j} - v\hat{t}\right)\right) + 1\right) \tag{5.1}$$

The shock speed is v, the shock front thickness is given by γ^{-1}, the final shock pressure by p, and the bulk modulus for both materials by B. The time has units of $\hat{t} \equiv at/c$. The variation of $\epsilon(\hat{x} \equiv \frac{x}{a})$ in the shocked crystal is given in terms of the bilayer interfaces as (neglecting the strain dependence of $\epsilon(\hat{x})$),

$$\begin{aligned} \epsilon(\hat{x}, \hat{t}) &= \frac{1}{2}(\epsilon_1 + \epsilon_2) + \\ \frac{1}{2}(\epsilon_2 - \epsilon_1)\tanh(\delta(\hat{x} - x_{1,j})), &\frac{1}{2}(x_{1,j} + x_{2,j-1}) \leq \hat{x} < \frac{1}{2}(x_{2,j} + x_{1,j}) \\ \epsilon(\hat{x}, \hat{t}) &= \frac{1}{2}(\epsilon_1 + \epsilon_2) + \\ \frac{1}{2}(\epsilon_2 - \epsilon_1)\tanh(-\delta(\hat{x} - x_{2,j})), &\frac{1}{2}(x_{2,j} + x_{1,j}) \leq \hat{x} < \frac{1}{2}(x_{1,j+1} + x_{2,j}). \end{aligned} \tag{5.2}$$

The time-dependence of ϵ enters from the time-dependence of the dielectric region interfaces, $\left(x_{1,j}(\hat{t}), x_{2,j}(\hat{t})\right)$. The dielectric alternates between ϵ_1 and ϵ_2 with tanh splines of width δ^{-1} between regions to prevent a moving discontinuity. To account for the strain dependence of the two dielectric regions, we apply a transform to the dielectric given by Equation 5.2,

$$\epsilon(\hat{x},\hat{t}) \rightarrow \epsilon(\hat{x},\hat{t}) \times \left[1 + \left(\frac{1}{\epsilon_1}\frac{d\epsilon_1}{ds_1} + \left(\frac{1}{\epsilon_2}\frac{d\epsilon_2}{ds_2} - \frac{1}{\epsilon_1}\frac{d\epsilon_1}{ds_1}\right)\frac{(\epsilon(\hat{x},\hat{t}) - \epsilon_1)}{(\epsilon_2 - \epsilon_1)}\right)\frac{p}{2B}\left(\tanh(-\gamma(\hat{x} - v\hat{t})) + 1\right)\right]. \quad (5.3)$$

In Figure 5-1, the thickness of the shock wave front (γ^{-1}) is 1, $\delta^{-1} = \frac{1}{60}$. Figure 5-2 is a schematic of the bandgap frequencies in front of and behind the shock front for the dielectric given in Figure 5-1. The 1st bandgap is lowered in frequency as the shock compresses the photonic crystal. Consider now continuous-wave electromagnetic radiation incident from the right (opposite to the direction of shock propagation) with frequency within the 1st bandgap of the post-shock crystal as shown in Figure 5-2. The frequency of this radiation is far from the 1st bandgap edge in the pre-shock crystal. The incident light is reflected and acquires a *reversed* Doppler shift, i.e. lowered frequency in this case.

Figure 5-3 shows the magnetic field for a FDTD simulation where this reversed Doppler effect is observed. The shock front (dashed line) has thickness $\gamma^{-1} = 2$ and propagates to the right with $v = 1.5 \times 10^{-2}c$, which is chosen to be artificially high for computational considerations. The panels in Figure 5-3 are obtained by Fourier transforming the magnetic field over windows of time ($\Delta t = 500a/c$) beginning at the times shown in the upper right corners. The top panel shows light incident from a source on the right, and the bottom panel shows this light reflecting with a decreased frequency.

Figure 5-4 shows a similar FDTD simulation where the shock front is considerably sharper, $\gamma^{-1} = 0.1$. Here, $v = 3 \times 10^{-3}c$ and the Fourier transform is performed over a time ($\Delta t = 3500a/c$). Multiple, equally-spaced reflected frequencies are observed in this case. These frequencies are a result of the time-periodic nature of the shock propagation over a periodic structure. The interpretation of the reflected light as

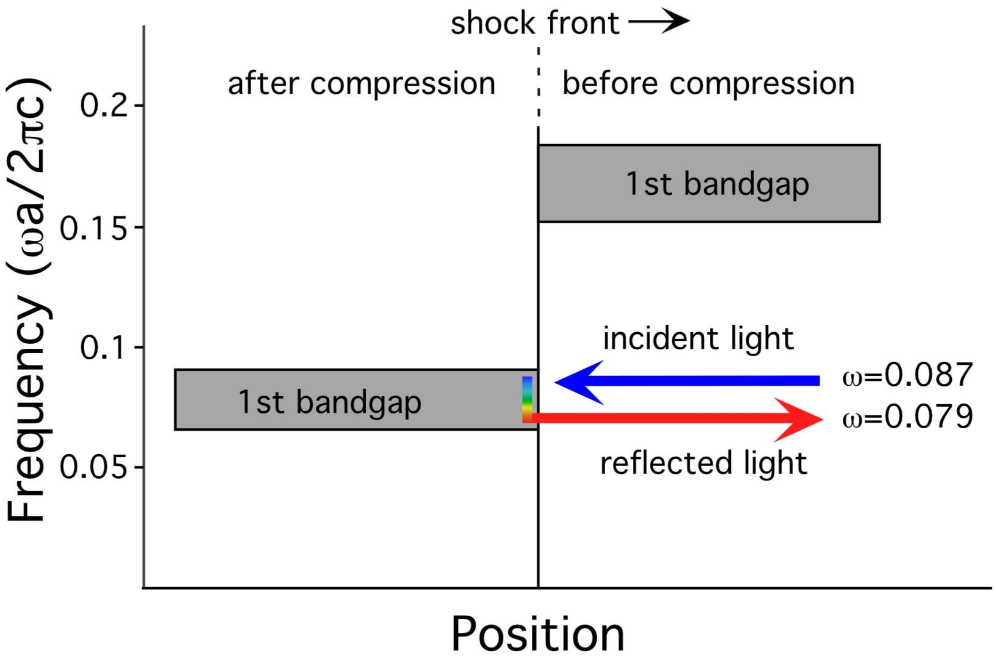

Figure 5-2: Schematic of a shock wave moving to the right that compresses the lattice but lowers the bandgap frequency due to a strain dependence of the dielectric. Light incident from the right reflects from the post-shock bandgap with a *reversed* Doppler shift.

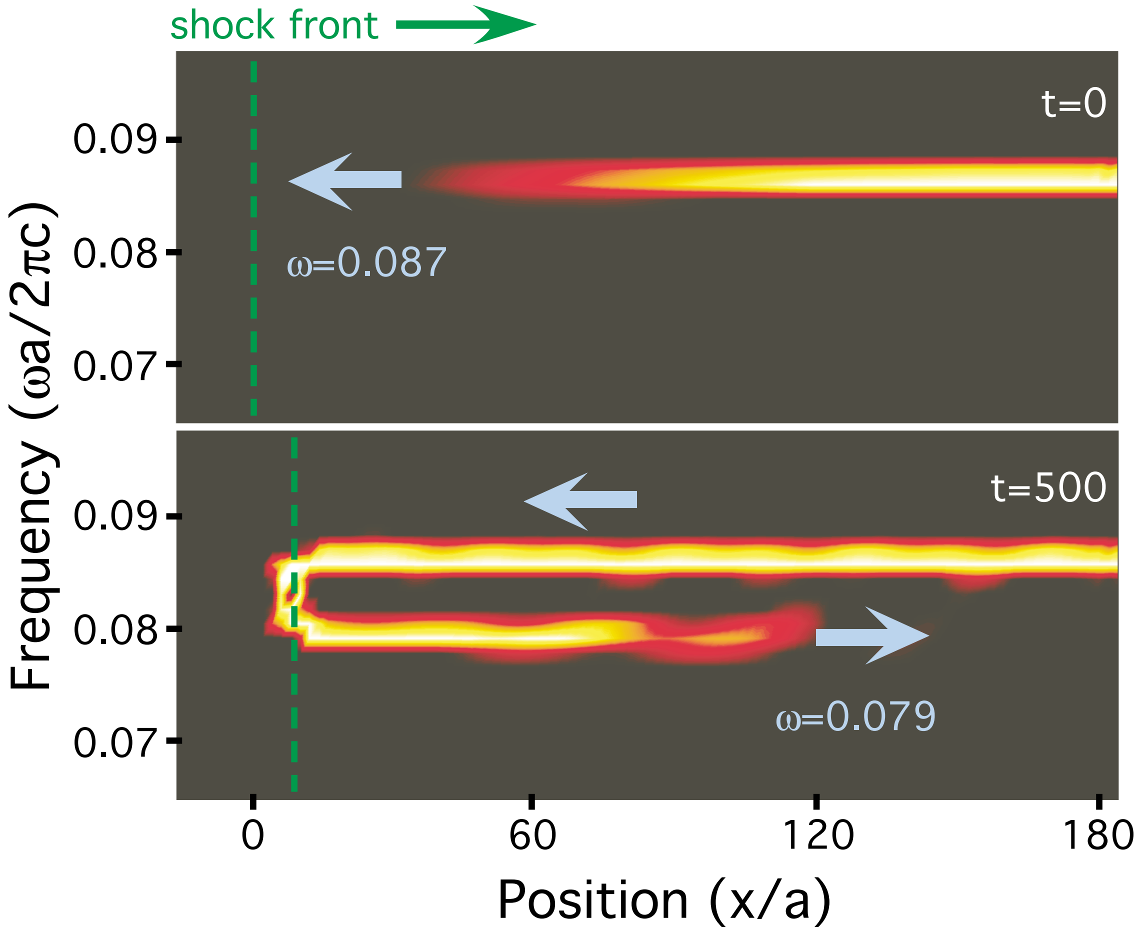

Figure 5-3: Reverse Doppler effect. Two moments in time during a computer simulation of a pulse of light reflecting from a time-dependent dielectric similar to Figure 5-1. The shock front is moving to the right and its location is approximately indicated by the dotted green line. Light incident from the right receives a negative, i.e. *reversed*, Doppler shift upon reflection from the shock wave. Time is given in units of a/c.

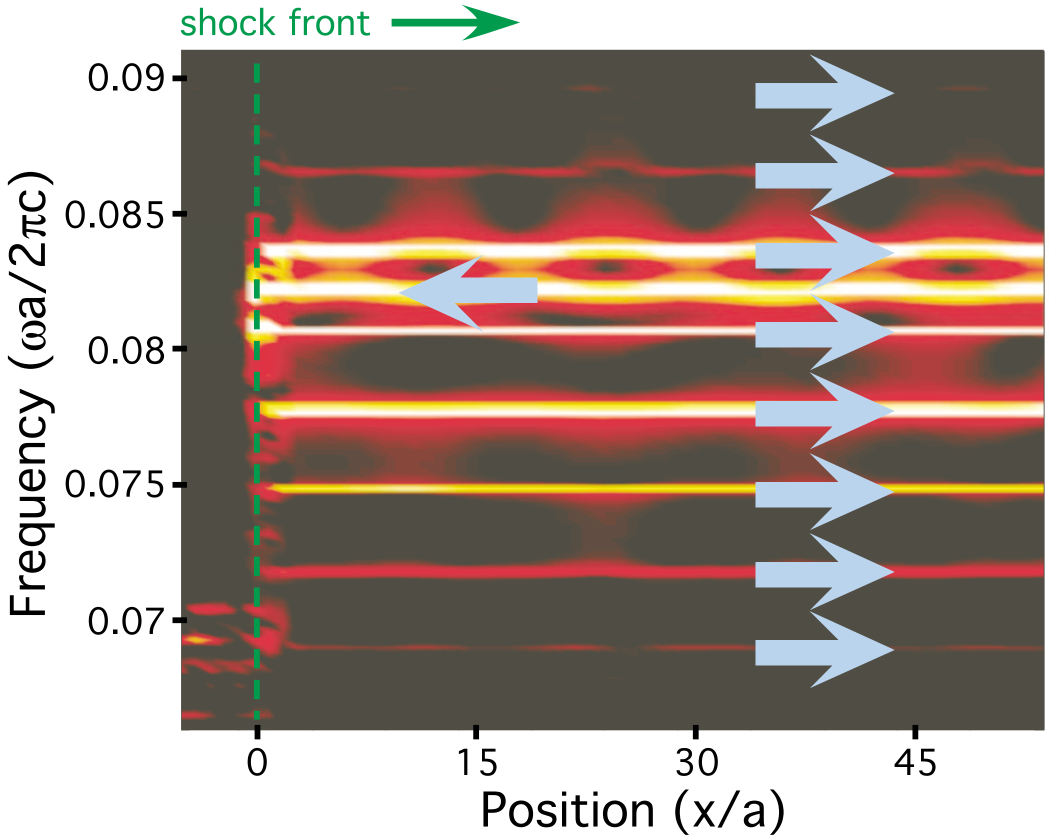

Figure 5-4: Computer simulation of a pulse of light reflecting from a dielectric similar to Figure 5-1, but with a sharper shock front than in Figure 5-3 (by a factor of 20). The shock front is moving to the right and its location is approximately indicated by the dotted green line. Light incident from the right is reflected in multiple equally-spaced frequencies due to the relatively sharp shock front.

multiple equally-spaced frequencies or a temporally periodic modulation of a single carrier frequency is a matter of resolution in the experimental apparatus. For light of 1 μm wavelength, the periodic modulation has a frequency around 10 GHz.

5.3 Analysis

The new physics presented here can be understood in terms of a simple analytical theory. We focus on a scenario where the incident light is at a frequency that falls within the gap of the post-shock, *compressed* crystal. An effective model of the shock front is a mirror with a space-dependent E field reflection coefficient, $R(x)$, where x is the mirror position. R has the property that $|R(x)| = 1$ since the incident light reflects from the bandgap of the post-shock crystal. In general R has some frequency dependence but we will consider the bandwidth of the incident light sufficiently small to neglect it. If the shock front is stationary, the condition on the electric field at the shock front in terms of the incident and reflected light is,

$$\sum_j E_j e^{-i(\omega_j t - k_j x)} = R(x) E_0 e^{-i(\omega_0 t + k_0 x)}, \tag{5.4}$$

where k_0 and k_j correspond to the respective incident and reflected wavevectors in the uniform medium and E_0 and E_j are constants. The reflection coefficient $R(x)$ can be written $R(x) = \sum_G \beta_G e^{-iGx}$ which is the most general form with the property that $R(x)$ is periodic in the pre-shock lattice, $R(x) = R(x + a)$. The reciporical lattice vectors G are $2\pi q/a$ where q is an integer. This substitution and letting $x \to x_0 + vt$, where v is the shock speed, yield the frequency shifts required by the time dependence of Equation 5.4 in the non-relativistic limit,

$$\omega_G - \omega_0 = (2k_0 + G)v. \tag{5.5}$$

The reflected light has frequency components ω_G that differ from the usual Doppler shift, $2k_0v$, by the amount Gv. The amplitude of each of the reflected components is,

$$|E_G| = |\beta_G||E_0|. \tag{5.6}$$

When $R(x)$ pertains to the ℓth bandgap, one can readily show that $|\beta_{\frac{-2\pi\ell}{a}}| > |\beta_{\frac{-2\pi q}{a}}|$ for all $q \neq \ell$. This is related to the discussion of Equation 4.10. Therefore, as the shock front is broadened, $R(x) \rightarrow \beta_{\frac{-2\pi}{a}} e^{\frac{i2\pi x}{a}}$ for light reflecting from the first bandgap. The reverse Doppler shift scenario in Figure 5-3 corresponds to this case where the only dominant component of $R(x) = \sum_G \beta_G e^{-iGx}$ is the one corresponding to $G = -2\pi/a$. Other frequency components of $R(x)$ are suppressed by the relatively broad shock front width in this case. Equations 5.5 and 5.6 indicate that the reflected light should have a single frequency with a negative shift if $v > 0$, $k_0 > 0$, and $|2k_0| < 2\pi/a$, which is the case in Figure 5-3. In Figure 5-4, the relatively sharp shock front gives rise to multiple reflected frequencies separated by $\frac{2\pi v}{a}$.

Equation 5.5 predicts that when $2k_0 = -G$ and there is only one reflected frequency component, the Doppler shift is zero. Likewise, if $2k_0 > -G$, the Doppler shift is positive (normal) but has a magnitude that is smaller than the usual $2k_0v$ Doppler shift. Both of these scenarios have been observed in our finite difference simulations.

We would like to emphasize that it is not possible to observe these anomalous effects by simply translating a photonic crystal through a uniform medium because the reflection coefficient for the photonic crystal in that case is constant, as in the case of a metal mirror. The key new physical phenomena presented here result from the fact that the shocked photonic crystal region "grows" into the pre-shocked region giving rise to a time-dependent reflection coefficient. It is also interesting to note that the velocity of the material behind the shock front plays no role in the Doppler shift phenomenon. Only the shock front velocity is relevant.

5.4 Practical considerations

In the finite difference simulations, we have chosen a 10GPa shock with large shock speeds and large strain dependence of the dielectric due to consideration for computational effort. The effects presented here are just as easily observable over a wide range of shock pressures, realistic shock speeds (1-10km/sec), and realistic values of $\frac{1}{\epsilon}\frac{d\epsilon}{ds}$. Materials are routinely shocked to GPa and higher pressures using lasers and gun facilities. Optical techniques involving the reflection of light from a moving shock front are used as diagnostics in shock experiments.[24, 4] Spectroscopic techniques possess ample resolution to observe the shifts proposed here which are comparable to a normal Doppler shift from an object moving on the order of 100 m/s.[27] It is also interesting to note that measurement of the properties of the reflected light in such an experiment allows determination of the shock front thickness as in Figures 5-3 and 5-4. This is currently difficult or impossible to accomplish in present-day experiments and is a new tool for the study of shock waves.

For small shock pressures, the requirement that the light be in the linear dispersion frequency region of the pre-shocked crystal (away from the band edge) can be accomplished by using a crystal with a small bandgap, e.g. by using a large layer of a material with large negative $\frac{d\epsilon}{ds}$ and a small layer of another material with a different dielectric. In this case, the condition on $\frac{d\epsilon}{ds}$ for the bandgap to decrease upon compression is $\frac{1}{\epsilon}\frac{d\epsilon}{ds} < -2$. Materials used for acoustic light modulation, like Te, or other high dielectric materials can be used to satisfy this condition. Alternatively, if light is reflected from the *rear* of the shock front (i.e. the incident light propagates the same direction as the shock), materials with $\frac{1}{\epsilon}\frac{d\epsilon}{ds} > -2$ (i.e. all other materials) can be employed to observe a reversed Doppler shift if the incident light is of a frequency within the bandgap of the pre-shock crystal.

Shock impedance matching between the two bilayers of the photonic crystal is important for the propagation of a steady shock wave. A wide variety of optical materials of varying impedances exist to simultaneously establish good impedance matching and dielectric contrast, for example Te and LiF. These two materials are not required to possess identical sound speeds because the reflection coefficient $R(x)$ is periodic in time even when the sound speeds differ. Differing bulk moduli between the two materials has little effect on the gap position when one of the bilayers is substantially smaller than the other.

While the emphasis of this work has been on the observation of anomalous Doppler shifts in a shocked photonic crystal, similar shifts can be observed in a variety of time-dependent photonic crystal systems. The key requirement is a time-dependent reflection coefficient. Materials that undergo a change in the dielectric constant under an applied electric field or applied change in temperature can be modulated in a time-dependent shock-like fashion, and micro electro-mechanical systems (MEMS) may also be used to observe the same phenomena.

5.5 Generalized shock wave

In this section, we consider a generalized shock wave containing only the essential features necessary for observing anomalous Doppler shifts. Consider a dielectric of the form,

$$\epsilon\left(\hat{x}=\frac{x}{a},\hat{t}=\frac{ct}{a}\right)=7+3\left[1-\tanh\left(\gamma\left(\hat{x}-\frac{v}{c}\hat{t}\right)\right)\right]\sin(2\pi\hat{x}). \tag{5.7}$$

This is shown in Figure 5-5. In this case, a moving interface exists between a photonic crystal and a uniform dielectric medium. The photonic crystal does not move relative to the uniform medium, but movement of the interface causes an expansion or growth of the crystal region. Practical methods of generating such a modulation involve materials that undergo a change in the dielectric constant under an applied electric field or applied change in temperature modulated in a time-dependent shock-like fashion.

Figure 5-6 shows the effect of this dielectric on a Gaussian pulse which propagates toward the moving interface from the uniform dielectric region. The light is at a

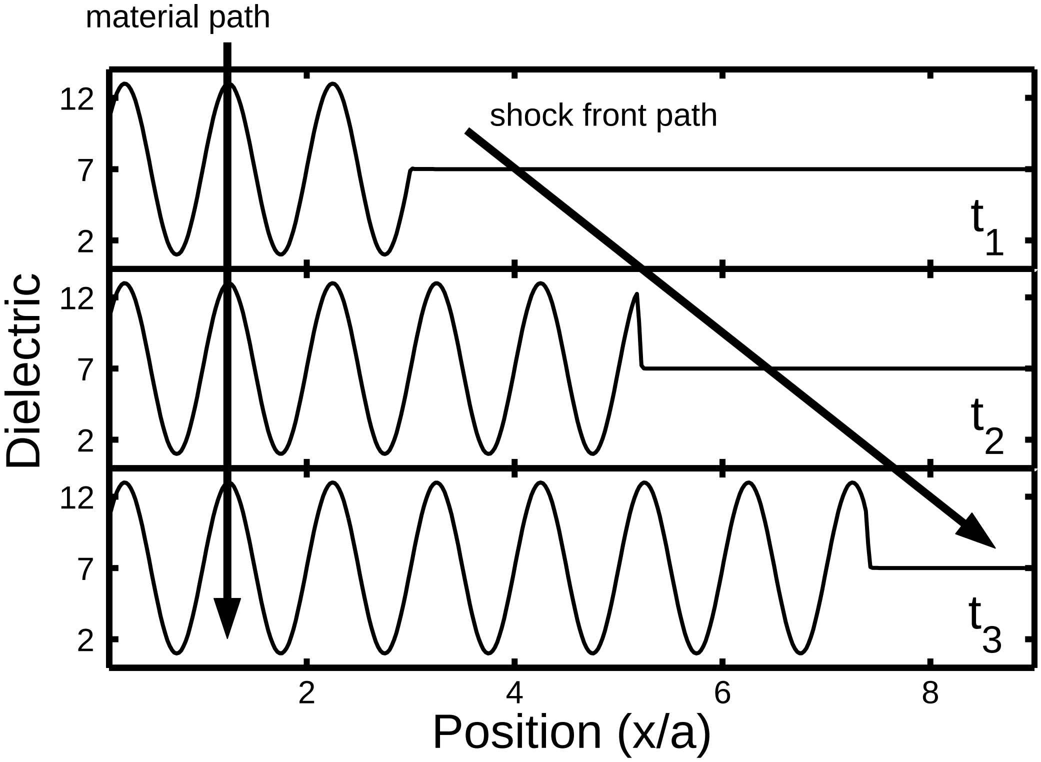

Figure 5-5: Dielectric as a function of position for three equally-spaced instants in time, $t_1 < t_2 < t_3$. Arrows follow the shock front and material paths which move at different speeds. As the interfaces moves, it causes an expansion or “growth” of the crystal region.

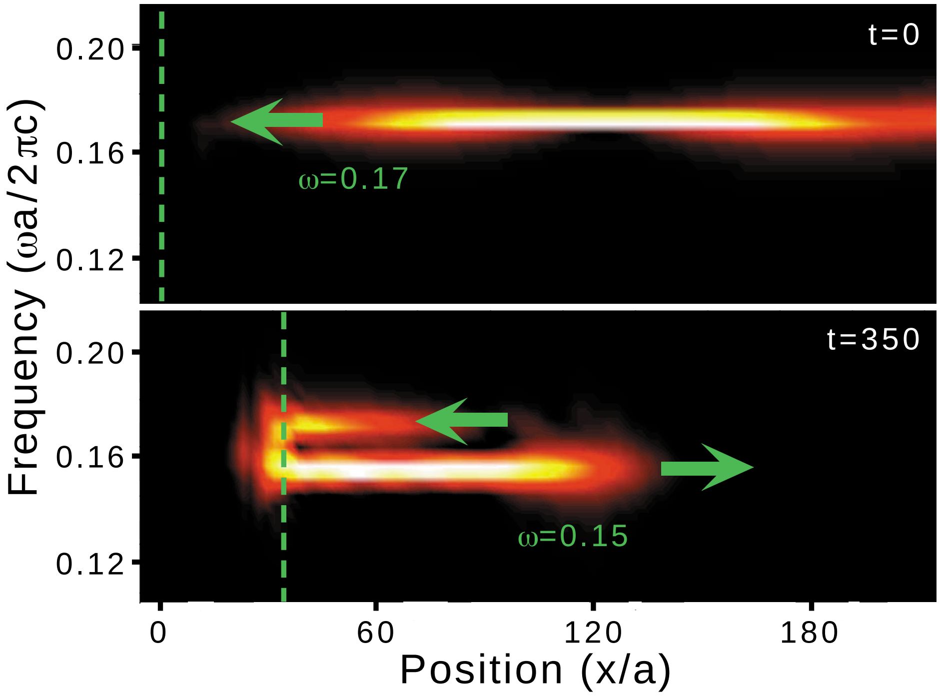

Figure 5-6: Depicted are two moments in time during a computer simulation of a pulse of light reflecting from the moving crystal of Figure 5-5. Time is given in units of a/c. The shock front is moving to the right and its location is approximately indicated by the dotted green line. Light incident from the right receives a negative Doppler shift upon reflection from the shock wave.

frequency where it is completely reflected by the bandgap region of the crystal, and a negative Doppler shift is observed. Here, $\gamma^{-1} = 1.8$, and $v = 0.125c$. A similar simulation was performed for a Gaussian pulse around $\omega = 0.19$ in which a zero Doppler shift was observed. A positive Doppler shift was observed for incident frequencies between about 0.19 and the top of the reflecting bandgap.

It is also possible to make light of a single frequency split into multiple discrete frequencies. This is illustrated in Figure 5-7. This simulation is similar to that in Figure 5-6 except the dielectric in the crystal region has additional high spatial frequency components. The dielectric is,

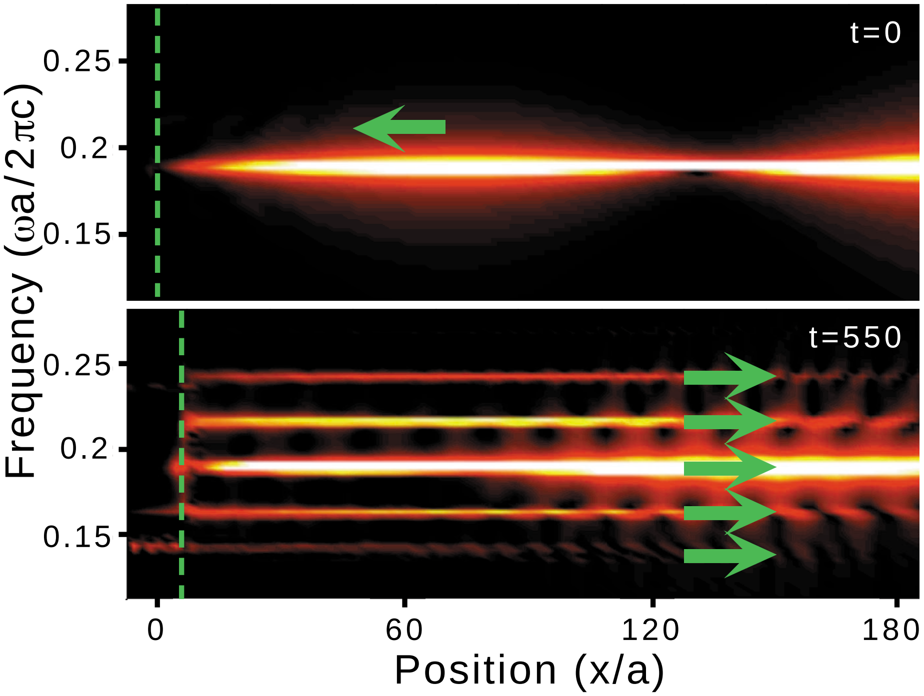

Figure 5-7: Depicted are two moments in time during a computer simulation of a pulse of light reflecting from the “growing” photonic crystal given by Equation 5.8. Time is given in units of a/c. The shock front location is approximately indicated by the dotted green line. Light incident from the right is split into multiple discrete frequencies upon reflection from the moving shock.

$$\epsilon\left(\hat{x}=\frac{x}{a},\hat{t}=\frac{ct}{a}\right)= \qquad (5.8)$$

$$7+3\left[1-\tanh\left(\gamma\left(\hat{x}-\frac{v}{c}\hat{t}\right)\right)\right]\left[\frac{4}{5}\sin(2\pi\hat{x})+\frac{1}{10}\sin(4\pi\hat{x})+\frac{1}{10}\sin(6\pi\hat{x})\right],$$

with shock front thickness parameter $\gamma^{-1}=0.013$ and $v=0.025c$.

The Gaussian pulse incident from the right in Figure 5-6 is split into evenly spaced frequencies upon reflection. Some of the light is reflected with no frequency shift. The intensity of each of the reflected frequency components can be controlled by adjusting the form of the dielectric in the crystal region. As in the cases of Figures 4-3 and 4-4, the interpretation of the reflected light as evenly-spaced discrete frequencies or as a periodic modulation of a single frequency is a matter of experimental timescale resolution.

The reverse Doppler shift scenario in Figure 5-6 corresponds to the case where the only dominant component of $R(x) = \sum_G \beta_G e^{-iGx}$ is the one corresponding to $G = -2\pi/a$. Equation 5.5 indicates that the reflected light should have a single frequency with a negative shift if $v < 0$, $k_0 < 0$, and $|2k_0| < 2\pi/a$, which is the case in Figure 5-6.

The multiple reflected frequencies of Figure 5-7 are also represented by Equation 5.5. In this case $R(x)$ has several spatial frequency components, which result from the high spatial frequency components in $\epsilon(x)$ for the crystal given by Equation 5.8. Furthermore, the incident light in the simulation in Figure 5-7 has wavevector $2k_0 = -2\pi/a$ which is coincident with a value of G for the crystal. Therefore, some of the reflected light has the same frequency as the incident light. Figure 6 was produced with a relatively broad shock front width greater than a, which has the effect of suppressing multiple reflected frequencies.

Finally, this chapter presents a new and general physical mechanism to manipulate and modulate the carrier frequency of light while performing the difficult task of preserving optical coherence. Potential applications for this technology include quantum information processing, all-optical signal processing, and new diagnostic tools for shock wave experiments.

Bibliography

[1] M. P. Allen and D. J. Tildesley. *Computer simulation of liquids.* Oxford University Press, New York, 1989.

[2] Y. Baryam and J. D. Joannopoulos. *Phys. Rev. Lett.*, 52:1129, 1984.

[3] A. M. Belyantsev and A. B. Kozyrev. *Tech. Phys.*, 47:1477, 2002.

[4] P. M. Celliers, G. W. Collins, L. B. Da Silva, D. M. Gold, R. Cauble, R. J. Wallace, M. E. Foord, and B. A. Hammel. *Phys. Rev. Lett.*, 84:5564, 2000.

[5] H. Chacham, X. Zhu, and S. G. Louie. *Phys. Rev. B*, 46:6688, 1992.

[6] C. S. Coffee. *Phys. Rev. B*, 24:6984, 1981.

[7] S. Courtecuisse, F. Cansell, D. Fabre, and J. P. Petitet. *J. Chem. Phys.*, 102:968, 1995.

[8] S. Courtecuisse, F. Cansell, D. Fabre, and J. P. Petitet. *J. Chem. Phys.*, 108:7350, 1998.

[9] D. T. Cromer, R. R. Ryan, and D. Schiferl. *J. Phys. Chem.*, 89:2315, 1985.

[10] J. J. Dick. *J. Phys. Chem.*, 97:6193, 1993.

[11] J. J. Dick, R. N. Mulford, W. J. Spencer, D. R. Pettit, E. Garcia, and D. C. Shaw. *J. Appl. Phys.*, 70:3572, 1991.

[12] J. J. Dick, R. N. Mulford, W. J. Spencer, D. R. Pettit, E. Garcia, and D. C. Shaw. *J. Appl. Phys.*, 70:3572, 1991.

[13] R. W. Dixon. *J. Appl. Phys.*, 38:5149, 1968.

[14] A. N. Dremin, V. Y. Klimenko, O. N. Davidove, and T. A. Zoludeva. In *The Ninth Symposium (International) on Detonation*, Portland, 1989.

[15] G. E. Duvall. In *Proceedings of the International School of Physics, Physics of High Energy Density*, page 7, New York, 1971. Academic Press.

[16] W. M. Ficker, O. A. Mosher, and A. Kuppermann. *Chem. Rev. Lett.*, 60:518, 1979.

[17] W. Fickett and W. Davis. *Detonation.* University of Califronia Press, Berkeley, CA, 1979.

[18] P. S. Fiske, W. J. Nellis, M. Lipp, H. Lorenzana, M. Kikuchi, and Y. Syono. *Science*, 270:281, 1995.

[19] L. E. Fried and A. J. Ruggiero. *J. Phys. Chem.*, 98:9786, 1994.

[20] T. C. Germann, B. L. Holian, P. S. Lomdahl, and R. Ravelo. *Phys. Rev. Lett.*, 84:5351, 2000.

[21] J. J. Gilman. *Philos. Mag. B*, 71:1957, 1995.

[22] R. A. Graham. *J. Phys. Chem.*, 83:3048, 1979.

[23] W. H. Gust and E. B. Royce. *J. Appl. Phys.*, 42:1897, 1971.

[24] R. Gustavsen and Y. M. Gupta. *J. Appl. Phys.*, 69:918, 1991.

[25] P. Hohenberg and W. Kohn. *Phys. Rev.*, 136:864B, 1964.

[26] B. L. Holian and P. S. Lohmdahl. *Science*, 280:2085, 1998.

[27] N. C. Holmes. *Rev. Sci. Instrum.*, 64:357, 1993.

[28] M. S. Hybertsen and S. G. Louie. *Phys. Rev. B*, 34:5390, 1986.

[29] V. K. Jindal and D. D. Dlott. *J. Appl. Phys.*, 83:3572, 1998.

[30] J. D. Joannopoulos, R. D. Meade, and J. N. Winn. *Photonic Crystals.* Princeton University Press, Princeton, NJ, 1995.

[31] S. John. *Phys. Rev. Lett.*, 58:2486, 1987.

[32] E. Jouget. *Mecanique des explosifs.* Octave Doin et Fils, Paris, 1917.

[33] K. Kadau, T. C. Germann, P. S. Lomdahl, and B. L. Holian. *Science*, 296:1681, 2002.

[34] M. D. Knudson and Y. M. Gupta. *Phys. Rev. Lett.*, 81:2938, 1998.

[35] J. D. Kress, S. R. Bickham, L. A. Collins, B. L. Holian, and S. Goedecker. *Phys. Rev. Lett.*, 83:3896, 1999.

[36] M. M. Kuklja and A. B. Kunz. *J. Appl. Phys.*, 86:4428, 1999.

[37] M. M. Kuklja, E. V. Stefanovich, and A. B. Kunz. *J. Chem. Phys.*, 112:3417, 2000.

[38] C. Liu, Z. Dutton, C.H. Behroozi, and L. V. Hau. *Nature*, 409:490, 2001.

[39] C. Livermore. *The Industrial Physicist*, 7:20, 2001.

[40] A. Loveridge-Smith, A. Allen, J. Belak, T. Boehly, A. Hauer, B. Holian, D. Kalantar, G. Kyrala, R. W. Lee, P. Lohmdahl, M. A. Meyers, D. Paisley, S. Pollaine, B. Remington, D. C. Swift, S. Weber, , and J. S. Wark. *Phys. Rev. Lett.*, 86:2349, 2001.

[41] J. B. Maillet, M. Mareschal, L. Soulard, R. Ravelo, P. S. Lomdahl, T. C. Germann, and B. L. Holian. *Phys. Rev. E*, 63:016121, 2001.

[42] M. R. Manaa and L. E. Fried. *J. Phys. Chem. A*, 103:9349, 1999.

[43] M. R. Manaa and L. E. Fried. *J. Phys. Chem. A*, 103:9349, 1999.

[44] Riad Manaa. Lawrence Livermore National Laboratory, private communication.

[45] Dionisios Margetis. Harvard University, private communication.

[46] M. I. McMahon and R. J. Nelmes. *Phys. Rev. B*, 47:8337, 1993.

[47] K. L. McNesby and C. S. Coffey. *J. Phys. Chem. B*, 101:3097, 1997.

[48] W. J. Nellis, S. T. Weir, and A. C. Mitchell. *Science*, 273:936, 1996.

[49] O. H. Nielsen and R. M. Martin. *Phys. Rev. B*, 32:3792, 1985.

[50] M. C. Payne, M. P. Teter, D. C. Allan, T. A. Arias, and J. D. Joannopoulos. *Rev. Mod. Phys.*, 64:1045, 1992.

[51] J. P. Perdew. In *Electronic Structure of Solids '91*, Berlin, 1991. Akademie-Verlag.

[52] J. P. Perdew, K. Burke, and M. Ernzerhof. *Phys. Rev. Lett.*, 77:3865, 1996.

[53] D. F. Phillips, A. Fleishhauer, A. Mair, R. L. Walsh, R. L. Walsworth, and M. D. Lukin. *Phys. Rev. Lett.*, 86:783, 2001.

[54] E. J. Reed, J. D. Joannopoulos, and L. E. Fried. *Phys. Rev. B*, 62:16500, 2000.

[55] I. N. Remediakis and E. Kaxiras. *Phys. Rev. B*, 59:5536, 1999.

[56] David Roundy. Massachusetts Institute of Technology, private communication.

[57] S. Sawada. *Vacuum*, 41:612, 1990.

[58] J. Sharma, B. C. Beard, and M. Chaykovsky. *J. Phys. Chem.*, 95:1209, 1991.

[59] F. Siringo, R. Pucci, and N. H. March. *High Press. Res.*, 2:109, 1989.

[60] Maksim Skorobogatiy and J. D. Joannopoulos. *Phys. Rev. B*, 61:5293, 2000.

[61] Maksim Skorobogatiy and J. D. Joannopoulos. *Phys. Rev. B*, 61:15554, 2000.

[62] F. H. Stillinger and T. A. Weber. *Phys. Rev. B*, page 5262, 1985.

[63] A. Taflove and S. C. Hagness. *Computational Electrodynamics: The finite-difference time-domain method.* Artech House, Norwood, MA, 2000.

[64] C. M. Tarver. *J. Phys. Chem.*, 101:4845, 1997.

[65] A. Tokmakoff, M. D. Fayer, and D. D. Dlott. *J. Phys. Chem.*, 97:1901, 1993.

[66] S. F. Trevino, E. Prince, and C. R. Hubbard. *J. Chem. Phys.*, 73:2996, 1980.

[67] S. F. Trevino and W. H. Rymes. *J. Chem. Phys.*, 73:3001, 1980.

[68] N. Troullier and J. L. Martins. *Phys. Rev. B*, 43:1993, 1991.

[69] D. Vanderbilt. *Phys. Rev. B*, 41:7892, 1990.

[70] V. G. Veselago. *Sov. Phys. USPEKHI*, 10:509, 1968.

[71] S. T. Weir, A. C. Mitchell, and W. J. Nellis. *Phys. Rev. Lett*, 76:1860, 1996.

[72] F. Williams. *Adv. Chem. Phys.*, 21:289, 1971.

[73] E. Yablonovich. *Phys. Rev. Lett.*, 58:1059, 1987.

[74] C. S. Yoo, W. J. Nellis, M. L. Sattler, and R. G. Musket. *Appl. Phys. Lett.*, 61:273, 1992.

[75] E. H. Younk and A. B. Kunz. *Int. J. Quantum Chem.*, 63:615, 1997.

[76] Ya. B. Zel'dovich and Yu. P. Raizer. *Physics of shock waves and high-temperature hydrodynamic phenomena.* Academic Press, New York, NY, 1967.

[77] V. V. Zhakhovskiǐ, S. V. Zybin, K. Nishihara, and S. I. Anisimov. *Phys. Rev. Lett.*, 83:1175, 1999.